ABSTRACT

MANESS, SHELIA JANE. Characterization of the Dynamics of β-Sheet Formation by Time-Resolved Infrared Spectroscopy and Computational Modeling. (Under the direction of Stefan Franzen.)

The mechanism of β-sheet formation is poorly understood due to difficulty in obtaining soluble β-hairpin samples. The recent design of β-sheet peptides with improved solubility provides an opportunity for spectroscopic study as models for β-hairpins in larger proteins. Dynamics were characterized for cyclic analogs of gramicidin S and two unconstrained β-sheet peptides referred to as H1a and H3. Thermodynamic parameters for peptide folding are determined by data collected using static, temperature-dependent Fourier transform infrared (FTIR) spectrometry. A nanosecond laser-induced temperature increase (T-jump) provides kinetic information about the unfolding or folding peptide. A correlation between computational methods and spectroscopic data was established using quench dynamics and density functional theory for two of the cyclic peptide structures.

Spectroscopic characterization of a series of three cyclic β-sheet peptides provide insight into the timescale for hydrogen bond propagation. Thermodynamic data for the 6-, 10-, and 14-mer peptides indicate that cooperativity increases with peptide length. Single exponential relaxation kinetics were observed and fit with a two-state model. The folding rates of cyclic peptides are accelerated by at least an order of magnitude over the rates of the linear β-hairpin peptides suggesting that nucleation processes are the rate-limiting step in the linear system.

The non-pre-nucleated β-hairpin peptides, H1a and H3, require both β-turn formation and hydrophobic collapse to establish a folded structure. H1a is a 16 residue peptide that cold-denatures in 5% hexafluoroisopropanol (HFIP). H3 has 12 amino acids and does not cold-denature but requires > 20% HFIP for increased structural features in aqueous solution. Kinetic analyses for these two peptides were made at different temperatures and varied frequencies in the amide I′ region. Bi-exponential fits of the relaxation lifetimes indicate the presence of a fast (ns) and slow (μs) phase in both systems. The faster time constant was assigned to β-turn formation while the slower phase corresponds to previous measurements of hydrophobic collapse on the microsecond timescale by Muñoz *et al*. (*Nature* **1997**, *390*, 196-199). Variation between fitted values of individual kinetic traces necessitated a global fitting procedure. Singular value decomposition (SVD) was used for feature reduction of the frequency dependent data. SVD analysis concludes that the H1a peptide conforms to a three-state model with observed time constants of 420 ± 7 ns and 5.8 ± 0.1 μs. H3 peptide fits a two-state model with an observed relaxation time of 1.2 ± 0.0 μs. The position of the hydrophobic core in the H3 peptide is one tetrad closer to the β-turn region than H1a. The slightly faster observed relaxation lifetime of H3 is most likely attributable to this physical difference.

Spectroscopic experimental evidence requires a structural correlation in order to interpret the results of folding and unfolding events. Quench dynamics and density function theory (DFT) calculations were used to complement experimental work and to aid in the analysis of two of the cyclic peptides. Calculated infrared spectra for the 6-mer peptide demonstrates agreement within 12 cm^{-1} between solution phase experimental results and gas phase predictions. The side-chains of the 6-mer were replaced by

primarily glycine or alanine with the exception of two proline residues. Additionally, the calculated infrared spectra of the decamer peptide with its original bulky side-chains showed reasonable agreement with a 10-mer structure having primarily glycine side-chains. Computational times can be greatly reduced if side-chain interactions are negligible to the overall outcome of the simulation which appears to be the case for these test models. The calculations presented in this study for the cyclic hexamer and decamer peptides corroborate the relationship between frequency and the folding state of a peptide established by experimental work.

CHARACTERIZATION OF THE DYNAMICS OF β-SHEET FORMATION BY TIME-RESOLVED INFRARED SPECTROSCOPY AND COMPUTATIONAL MODELING

by
SHELIA JANE MANESS

A dissertation submitted to the Graduate Faculty of
North Carolina State University
in partial fulfillment of the
requirements for the Degree of
Doctor of Philosophy

CHEMISTRY

Raleigh

2003

APPROVED BY:

_____ _____

_____ _____
Chair of Advisory Committee

Dedicated to My Parents, Jack and Minnie Maness

BIOGRAPHY

My educational background is deeply rooted in the Great State of North Carolina. The chronology of my educational history goes back to Farmer Elementary and Middle School in Farmer, NC followed by graduation from Southwestern Randolph High School in Asheboro, NC. I obtained a Bachelor of Science degree in chemistry with associate honors at Western Carolina University in Cullowhee, NC followed by a Master of Science degree in analytical chemistry at the University of North Carolina at Greensboro in Greensboro, NC. Upon submission of this dissertation, I hereby complete the requirements for the Doctor of Philosophy degree from the Department of Chemistry at North Carolina State University in Raleigh, NC.

ACKNOWLEDGMENTS

"Wherefore seeing we also are compassed about with so great a cloud of witnesses, let us lay aside every weight, and the sin which doth so easily beset us, and let us run with patience the race that is set before us, Looking unto Jesus the author and finisher of our faith; who for the joy that was set before him endured the cross, despising the shame, and is set down at the right hand of the throne of God. For consider him that endured such contradiction of sinners against himself, lest ye be wearied and faint in your minds."
Hebrews 12:1-3

I express my sincere gratitude to Professor Stefan Franzen at North Carolina State University and Dr. R. Brian Dyer at Los Alamos National Laboratory for investing so much of their time and energy helping me to attain my educational goals. Much appreciation is felt for their encouragement and support during my doctoral research. The high standards that they uphold in their roles as both a scientist and a mentor are the guideposts which I will use in my own life and professional career.

Much appreciation is also expressed to my family and friends for the lifetime of encouragement they have given to me. I especially thank my parents, Jack and Minnie Maness, for their love and support that made my college ambition possible. I also gratefully acknowledge my aunts, Dr. Catherine de Nerville and Mrs. Peggy Wood, who inspired me at an early age to always set high goals.

Finally, I gratefully acknowledge the financial support provided to me during my doctoral research in the form of a research assistantship under Prof. Stefan Franzen and a graduate research assistantship at Los Alamos National Laboratory sponsored by Dr. R. Brian Dyer. Additionally, I thank North Carolina State University for providing the initial funding for my graduate studies as a teaching assistant.

TABLE OF CONTENTS

Page

Page

LIST OF TABLES

Page

Page

Chapter 4

Chapter 5

LIST OF FIGURES

Page

Chapter 2

Chapter 3

Page

Chapter 4

Page

Chapter 5

Chapter 1

Introduction to the Protein Folding Problem

INTRODUCTION

The Protein Folding Problem

Protein folding has gained increasing attention in recent years as the Human Genome Project is completed and extensive protein sequence information is now available as a result of this work. Advances in science and technology have led to the sequencing of the human genome which also codes for the proteome, or the protein sequences. The task of interpreting the massive amounts of information contained not only in genes, but also in proteins, now confronts the scientific community. The challenge of finding the relationship between protein sequence, structure, and function has been named the Protein Folding Problem. The Protein Folding Problem has been elegantly described by the following schematic:[1]

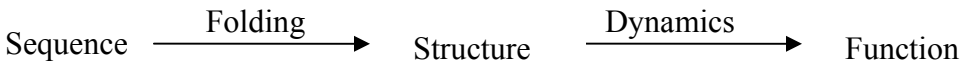

The primary sequence encodes the information required for the structure,[2-4] while the structure of the protein determines the function. The link between sequence and structure lies in understanding folding mechanisms, while dynamics provide the key to determining the influence of structure on function.

The 1973 Nobel Prize in chemistry was awarded to Christian B. Anfinsen for his work in the field of protein folding. Anfinsen discovered that ribonuclease protein could be induced to unfold using a denaturant and subsequently refold into a biologically active structure with the addition of appropriate reducing material.[2] This research proposed the 'thermodynamic hypothesis' which asserts that proteins acquire the structure of lowest Gibbs free energy for the conditions under which they exist.[2] In the decades following

Anfinsen's discovery, investigations related to the Protein Folding Problem have played a major role in the fields of biochemistry and biophysics.

In addition to the intellectual challenge posed by the Protein Folding Problem, there are also pragmatic concerns related to structure / function predictions. Three challenges to be addressed by protein folding studies are the post genomic era, misfolding disease states, and the biotechnology industry. Each of these areas requires a detailed understanding of the dynamic processes underlying the activities of proteins. These three topics will be addressed due to their relevance in enhancing the quality and longevity of life.

The intrinsic blueprint that determines life is found inside the cells of every living organism. A brief synopsis of the processes of life will help to establish the context of proteins in the big picture. A healthy human has 23 pairs of chromosomes which are comprised of the DNA that encodes for the genome of an individual.[5] Although genome sizes vary by species, the human and mouse genome both contain an estimated 3 billion base pairs of DNA, and the amount of DNA per chromosome can vary between 50-250 million base pairs.[5] Genes are sections of DNA found on the chromosomes which control factors of heredity by coding for specific proteins.[5] On average, genes are typically about 3000 base pairs in size, and there are approximately 30,000 to 35,000 genes in the human genome. Interestingly, this number only accounts for ~2% of the DNA with over half of the genes discovered having unknown functions.[5] The remaining sections of DNA are referred to as non-coding regions and are thought to be involved in the structural integrity of the chromosome and in protein regulatory functions.[5] Although proteins represent only about 2% of the human genome, they comprise and perform the

majority of cellular functions using a repertoire of only 20 amino acids.[5] It is important to note that proteins exist in a constant state of flux in response to signals from the cellular environment while the genome of a cell remains relatively constant.[5] Because proteins are the primary sites of activity within a cell, proteomics, the study of protein structure and function, will be the main focus for understanding the biological mysteries of both animals and plants in the post genomic era.[5]

The insights gained from proteomics will aid in understanding the protein misfolding problem. When protein folding goes awry, the consequences range from imperceptible to fatal.[6] Ideally, a misfolded protein is escorted from the ribosome by a molecular chaperone to a multi-component system called the ubiquitin-proteasome system (UPS) which identifies and destroys the protein[6]. However, problems arise when a cell's natural defenses are either defeated or overwhelmed by deleterious proteins. Some examples of neurodegenerative protein folding diseases include Alzheimer's disease, Parkinson's disease, and prion diseases such as Mad Cow disease in animals and Creutzfeldt-Jacob disease in humans.[6,7] Although the toxicity mechanisms of these neurodegenerative diseases are still under investigation, the overall similarities resulting from misfolding proteins suggest a common approach for treatment.[6] In the case of Alzheimer's disease, amyloid fibrils, or plaques of ordered aggregates of mostly β-amyloid peptide, accumulate in extracellular brain tissue, while tangles of the cytoskeletal protein tau form intracellular lesions.[6] The amyloid cascade hypothesis suggests that plaque formation is the precursor to all subsequent maladies such as synapse loss.[6,8] Plaque accumulation occurs as a result of the exposure of hydrophobic surfaces of β-amyloid peptide, and evidence tends to favor a nucleation-growth model for

the polymerization process that ensues.[7] Aggregation of an intermediate state is hypothesized to be more plausible than that of an unfolded state since the hydrophobic portions of an intermediate are more ordered than the random distribution of those in an unfolded state.[7] In addition to the hydrophobic propensity of peptide or protein residues, other factors such as temperature, pH, concentration, ionic strength, and co-solutes also influence aggregation susceptibility.[7] Alzheimer's disease afflicts nearly 2 million Americans [6](~10% of people over age 65 and ~50% of people over age 85), costs around $83 billion to care for patients, and kills 100,000 Americans annually.[9] While these figures only reflect statistics for Alzheimer's patients, the combined effects of all diseases induced by protein misfolding, or the lack of properly folded protein such as the case for cystic fibrosis, hereditary emphysema, and cancer, should not be under-estimated, and the structure / function relationship of proteins must continue to be aggressively pursued.

Understanding the protein folding problem is also a challenge in the biotechnology industry where the motivation is economic rather than altruistic. Production processes that generate protein products are sometimes known to result in insoluble precipitates of disordered aggregates called inclusion bodies.[7] Bacteria are used to express proteins for drugs, and scientists have observed that unexpected problems sometimes arise in the production process.[9] Two particular problems have been noted in the process of overexpressing proteins.[9] First of all, the protein can form inclusion bodies within the bacteria thereby necessitating a renaturation step to the process.[7,9] Secondly, proteins are sometimes unable to be excreted through the membrane wall into the medium outside of the bacteria.[9] Other difficulties have also been noted in the storage and delivery of protein drugs,[7] and as a result, the biotechnology industry began to

investigate the causes of these problems which led to a better understanding of protein misfolding. In an effort to overcome some of the issues of working with proteins in the biotechnology industry, Waldo *et al.* report a technique whereby green fluorescent protein (GFP) is fused to a target protein during the production process and the absence of a fluorescent signature is an indication of the presence of inclusion bodies.[10] The technique is general in nature and has been demonstrated to be effective using 20 test proteins.[10] The use of GFP is an example of the advances that will undoubtedly arise from the necessity of monitoring protein folding in the biotechnology industry.

Fast Events in Protein Folding

Although the protein folding problem is vast in scope, a more manageable approach is to focus on the early, submillisecond events of folding. This method offers several advantages since most of the fundamental processes of folding are fast and fortuitously provide overlap of experimental results with computer simulations. Additionally, there may be biological significance for the fast folding of proteins. These topics will be addressed in this section.

Fast dynamics (submillisecond) are of particular interest because of the fundamental processes which occur on these timescales.[11-18] Secondary structure formation, chain collapse, and diffusion processes are some examples of these early events. For example, an α-helix secondary structure is known to fold on a timescale of ~200 ns,[19,20] while small β-hairpins have been shown to fold with a lifetime of 6 μs.[21] The coiled-coil peptide GCN4-p1 folds on the order of 20 μs as measured by temperature jump techniques.[1] Temperature jump fluorescence studies have been used to study the collapse of cytochrome c protein into a compact denatured state from an expanded

denatured structure via a two-state process.[12,22] Biexponential kinetics are observed for the overall unfolding processes of cytochrome c with τ_1 ~100 μs and τ_2 ~1-10 ms.[22] These lifetimes represent re-equilibration between expanded and compact denatured states for τ_1 and the re-equilibration of denatured states and native structures for τ_2.[22] End-to-end chain diffusion for cytochrome c is estimated to be ~100 μs.[22] These examples are representative but not exhaustive of folding events which occur on the submillisecond timescale.

Early events in protein folding can be modeled by computer simulation. Simulation folding events are generally limited to short timescales (< 10 ns) due to computational expense. There are some clear advantages to simulation techniques. First of all, with the vast amount of data generated from the human genome project, computer simulations are more practical in terms of required materials and available methods of analysis. Secondly, experimental parameters and conditions can be adjusted to imitate the physiological milieu of a cellular environment. Lastly, computational methods are able to test the current level of theory for structure / function predictions. On the other hand, due to varying force fields, differences in potential energy surfaces, etc., the results from computer simulations are sometimes difficult to interpret relative to each other and also relative to experiment. Solvent effects may also play a significant part in the overall folding calculation and should be taken into consideration when interpreting results. Explicit solvent models are computationally expensive. An alternative is the use of implicit solvent added to the potential energy function. Implicit salvation is much less costly, however, the accuracy of such models is difficult to assess. Consequently, fast experimental techniques are necessary to check the accuracy of simulations which have

inundated the literature in recent years. Some of the most popular methods of simulating protein folding are using both lattice and off-lattice bead models of residues, as well as all-atom Monte Carlo and molecular dynamics studies.[12,23] Fluorescence temperature jump measurements of the 16-residue β-hairpin peptide from the B1 domain of protein G have set an experimental benchmark for ensuing computational models of β-sheet peptides.[21] A folding lifetime of 6 μs was observed for GB1, and the data was interpreted using a statistical mechanical model that suggested that the β-turn region forms first, followed by a zipping up of the hydrogen bond registry.[21,24] Subsequent course-grained, off-lattice Langevin simulations qualitatively produced the results observed by the statistical mechanical model and concluded that the stiffness of the β-turn region as determined by the position of the hydrophobic core would dictate the folding mechanism and kinetics.[25] Another simulation of the same 16-residue sequence of GB1 using Monte Carlo dynamics (MCD) and Entropy Sampling Monte Carlo (ESMC) returned a mixed result indicating that formation of the turn region followed by hydrogen bond zipping tends to occur most frequently, however, there were also indications that hydrophobic collapse followed by hydrogen bond propagation does occur occasionally.[26] MCD was tested at several temperatures while the ESMC studies provided a complete thermodynamic profile.[26] Molecular dynamics studies on GB1 indicate that hydrophobic collapse is the primary event initiating folding,[27] and multicanonical Monte Carlo simulations concur with this assessment.[28] As a result of the conflicting mechanisms determined by various simulation techniques, more experimental analyses of submillisecond kinetics on other model systems is needed to establish the mechanism of β-hairpin formation.

While the study of early events in protein folding is needed to elucidate mechanistic questions, there may or may not be a direct biological significance for fast folding. One idea is that folding times should not be a concern as long as folding occurs on the same order of time as protein synthesis.[12] *Escherichia coli* bacteria is known to synthesize 10-15 amino acids per second,[12] which means that a protein consisting of 350 amino acids could be produced in ~30 seconds.[29] If rapid folding is necessary, proteins that fold faster than ~1/minute should not be prone to aggregation.[12] Most two-state proteins are known to fold with a time constant of 20 ms or less in the absence of denaturant.[14] Based on evidence from studies of protein misfolding, the presence of long-lived intermediates is an indication of possible adverse effects due to aggregation.[7,30] The kinetics of aggregation for disease state folding intermediates of β-amyloid peptides varies depending on sample preparation and experimental conditions.[7] Since there is no direct evidence for the biological significance of fast folding, an answer to this question must await further discoveries in early folding events.

Peptide Model Studies

Protein folding studies have greatly benefited from work with peptide model systems. Gaining an understanding of the constituent pieces will aid in the overall interpretation of the protein folding problem. The simplest pieces of a protein are its secondary structure components, α-helices, β-sheets, and turn regions which are all connected by loops.[31]

More work has been done to study α-helices since approximately one third of the amino acid residues in proteins are part of an α-helix conformation.[32] Some of the early thermodynamic models proposed for α-helices come from the works of Schellman,

Zimm and Bragg, Lifson and Roig, and Poland and Scheraga.[33] Recently, a helix-coil model that combines both thermodynamic and kinetic properties has been designed which predicts a biphasic folding reaction for α-helices.[34] A fast phase describes the unzipping and zipping of the terminal residues (~20 ns) while a slow phase is indicative of the flux of interactions that must occur before the nucleation free energy barrier is finally crossed (~200 ns).[34,35] These studies of α-helix formation have proven to be successful in demonstrating that folding mechanisms of secondary structure can be predicted with increasing accuracy.

Inherent problems with β-sheets have impeded their characterization in comparison to more abundant α-helix peptide models. Solubility and aggregation are the most pervasive issues encountered in the study of β-sheet peptides.[36,37] Low structural content in water is also a factor that must be considered.[38,39] Model β-sheet peptides are often designed with enhanced stability in order to overcome the problem of low structural content in aqueous solution, however, a balance must exist to guard against excessive stability which can lead to aggregation.[40] Another obstacle in the design of β-sheet peptide models arises from the influence of context effects. The tertiary location of β-strands has been shown to influence the β-sheet formation propensity of amino acids based on the position of the β-strand at an edge or in a central region of the protein.[41,42] As a result of these influences, the study of secondary structure using simple β-sheet peptide models has not been easy.[38]

In an effort to acquire suitable model systems which could be studied in a context-free environment, efforts have been made to adapt naturally-occurring β-hairpin sequences from proteins,[21,39,43] as well as to design *de novo* peptides which are soluble

and monomeric.[36-38,43-49] Experimental characterization efforts have mostly involved NMR,[39,48,50,51] IR,[52,53] and CD studies,[39,46,51,54,55] although CD is not especially sensitive to changes in β-hairpin structure.[40,49] Highlights from these studies indicate the importance of turn region sequence,[38-40,48,51,56] side chain – side chain interactions,[38,40,50] and intra- and inter-strand hydrogen bonding.[46,53] Understanding these properties has led to the recent successes in designing soluble β-hairpin peptides.

Infrared Spectroscopic Methods of Analysis

Infrared spectroscopy is a powerful tool for elucidating the structural characteristics of proteins and peptides. The amide I region (1610-1680 cm^{-1}) is particularly rich with vibrational information which has been catalogued over many years to provide well-established libraries of spectral signatures.[57-60] Fourier transform infrared spectroscopy (FTIR) was used in the research presented in this dissertation to measure static, temperature-dependent absorbance traces. Difference spectra of these absorbance data were used to identify regions of maximum β-structure intensity. Melt curve plots of these maximum intensity regions, as well as singular value decomposition (SVD) methods (discussed in Chapter 4), helped to identify the appropriate fitting model for the processes observed (i.e. two-state or non-two-state). The combined information of spectral feature positions in the amide I region and corresponding intensities obtained from FTIR studies was used in infrared probe temperature jump kinetic experiments. Kinetics were probed in regions of maximum intensity to generate signals which could then be fitted to determine the observed relaxation time. The use of an infrared probe in conjunction with temperature jump (T-jump) spectroscopy is a powerful means of measuring vibrational frequencies of fast events in peptide folding. The results of the

temperature jump experiments, in conjunction with the thermodynamic data obtained from equilibrium FTIR studies, is used to help identify possible folding mechanisms for β-sheet peptides.

Computational Methods of Analysis

Computer simulations can be used to model the partially folded and unfolded states of peptides. The simulations in this dissertation are based on gas phase quench dynamics studies for two of the cyclic peptides discussed in Chapter 3. The goal of quench dynamics simulations was to provide approximate models of different hydrogen bonding states of the peptide molecule. As part of the quench dynamics process, molecular dynamics were performed on peptide structures at elevated temperatures. The cyclic β-sheet peptide structures sample a variety of conformations while propagating at high temperatures. Structures were quenched (annealed and energy minimized) at defined points in the simulation process to collect a number of structures. The structures were classified into families based on conformational similarities. Representative members of each of the families were used as models for calculating infrared spectra using density functional theory (DFT) methods. The goal of the computational modeling work is to provide a link between possible structures and the spectra observed experimentally as a function of temperature or time.

Simple general features are observed from the structure-spectroscopy correlation. Folded structures tend to have lower frequencies than unfolded structures due to the formation of C=O…N-H hydrogen bonds in the β-sheet conformation. Intermediate forms that have less than the maximum number of hydrogen bonds of the folded structure tend to have frequencies intermediate to that of the folded and unfolded structures. These

general relationships provide a useful means for comparing computational calculations of structures with spectroscopic experimental results for the β-sheet peptides.

Hypothesis

Do β-sheets fold with a characteristic lifetime? If so, is the folding lifetime dependent on the sequence of amino acids? The following chapters seek to address these two questions. The initial hypothesis is that β-hairpins form with a characteristic lifetime which is defined by an underlying molecular mechanism. Studies of fast events are needed to elucidate the molecular mechanism, and this is accomplished using infrared probe time-resolved spectroscopy.

REFERENCES

(1) Dyer, R. B.; Gai, F.; Woodruff, W. H.; Gilmanshin, R.; Callender, R. H. *Acc. Chem. Res.* **1998**, *31*, 709-716.

(2) Anfinsen, C. B. *Science* **1973**, *181*, 223-230.

(3) Kim, P. S.; Baldwin, R. L. *Annu. Rev. Biochem.* **1982**, *51*, 459-489.

(4) Dill, K. A. *Biochemistry* **1990**, *29*, 7133-7155.

(5) http://www.ornl.gov/hgmis/project/info.html; U. S. DOE Office of Science Office of Biological and Environmental Research, Human Genome Project, 2002.

(6) Taylor, J. P.; Hardy, J.; Fischbeck, K. H. *Science* **2002**, *296*, 1991-1995.

(7) Fink, A. L. *Folding Des.* **1998**, *3*, R9-R23.

(8) Selkoe, D. J. *Annual Review of Cell Biology* **1994**, *10*, 373-403.

(9) http://www.faseb.org/opar/protfold/protein.html; Thomasson, W. A., 2001.

(10) Waldo, G. S.; Standish, B. M.; Berendzen, J.; Terwilliger, T. C. *Nature Biotechnology* **1999**, *17*, 691-695.

(11) Myers, J. K.; Oas, T. G. *Annu. Rev. Biochem.* **2002**, *71*, 783-815.

(12) Eaton, W. A.; Munoz, V.; Hagan, S. J.; Jas, G. S.; Lapidus, L. J.; Henry, E. R.; Hofrichter, J. *Annu. Rev. Biophys. Biomol. Struct.* **2000**, *29*, 327-359.

(13) Callender, R. H.; Dyer, R. B.; Gilmanshin, R.; Woodruff, W. H. *Annu. Rev. Phys. Chem.* **1998**, *49*, 173-202.

(14) Eaton, W. A.; Munoz, V.; Thompson, P. A.; Chan, C. K.; Hofrichter, J. *Curr. Opin. Struct. Biol.* **1997**, *7*, 10-14.

(15) Miranker, A. D.; Dobson, C. M. *Curr. Opin. Struct. Biol.* **1996**, *6*, 31-42.

(16) Roder, H.; Colon, W. *Curr. Opin. Struct. Biol.* **1997**, *7*, 15-28.

(17) Fersht, A. R. *Curr. Opin. Struct. Biol.* **1997**, *7*, 3-9.

(18) McCammon, J. A. *Proc. Natl. Acad. Sci. USA* **1996**, *93*, 11426-11427.

(19) Williams, S.; Causgrove, T. P.; Gilmanshin, R.; Fang, K. S.; Callender, R. H.; Woodruff, W. H.; Dyer, R. B. *Biochemistry* **1996**, *35*, 691-697.

(20) Werner, J. H.; Dyer, R. B.; Fesinmeyer, R. M.; Andersen, N. H. *J. Phys. Chem. B* **2002**, *106*, 487-494.

(21) Munoz, V.; Thompson, P.; Hofrichter, J.; Eaton, W. A. *Nature* **1997**, *390*, 196-199.

(22) Hagen, S. J.; Eaton, W. A. *J. Mol. Biol.* **2000**, *301*, 1019-1027.

(23) Mirny, L.; Shakhnovich, E. *Annu. Rev. Biophys. Biomol. Struct.* **2001**, *30*, 361-396.

(24) Munoz, V.; Henry, E.; Hofrichter, J.; Eaton, W. *Proc. Natl. Acad. Sci. USA* **1998**, *95*, 5872-5879.

(25) Klimov, D. K.; Thirumalai, D. *Proc. Natl. Acad. Sci. USA* **2000**, *97*, 2544-2549.

(26) Kolinski, A.; Ilkowski, B.; Skolnick, J. *Biophys. J.* **1999**, *77*, 2942-2952.

(27) Pande, V. S.; Rokhsar, D. S. *Proc. Natl. Acad. Sci. USA* **1999**, *96*, 9062-9067.

(28) Dinner, A.; Lazaridis, T.; Karplus, M. *Proc. Natl. Acad. Sci. USA* **1999**, *96*, 9068-9073.

(29) Lorimer, G. H. *FASEB Journal* **1996**, *10*, 5-9.

(30) Kelly, J. W. *Structure* **1997**, *5*, 595-600.

(31) Nolting, B. *Protein Folding Kinetics*; Springer: Berlin, 1999.

(32) Fersht, A. R. *Structure and Mechanism in Protein Science: A Guide to Enzyme Catalysis and Protein Folding*; W. H. Freeman and Company: New York, 1999.

(33) Huang, C. Y.; Getahun, Z.; Wang, T.; DeGrado, W. F.; Gai, F. *J. Am. Chem. Soc.* **2001**, *123*, 12111-12112.

(34) Thompson, P. A.; Eaton, W. A.; Hofrichter, J. *Biochemistry* **1997**, *36*, 9200-9210.

(35) Thompson, P.; Munoz, V.; Jas, G.; Henry, E.; Eaton, W.; Hofrichter, J. *J. Phys. Chem. B* **2000**, *104*, 378-389.

(36) Kortemme, T.; Ramírez-Alvarado, M.; Serrano, L. *Science* **1998**, *281*, 253-256.

(37) Schenck, H. L.; Gellman, S. H. *J. Am. Chem. Soc.* **1998**, *120*, 4869-4870.

(38) Ramirez-Alvarado, M.; Kortemme, T.; Blanco, F. J.; Serrano, L. *Bioorg. Med. Chem.* **1999**, *7*, 93-103.

(39) Maynard, A. J.; Sharman, G. J.; Searle, M. S. *J. Am. Chem. Soc.* **1998**, *120*, 1996-2007.

(40) Blanco, F.; Ramirez-Alvarado, M.; Serrano, L. *Curr. Opin. Struct. Biol.* **1998**, *8*, 107-111.

(41) Minor Jr., D. L.; Kim, P. S. *Nature* **1994**, *371*, 264-267.

(42) Minor Jr., D. L.; Kim, P. S. *Nature* **1994**, *367*, 660-663.

(43) Espinosa, J. F.; Gellman, S. H. *Angew. Chem. Int. Ed.* **2000**, *39*, 2330-2333.

(44) Fisk, J.; Gellman, S. *J. Am. Chem. Soc.* **2001**, *123*, 343-344.

(45) Neidigh, J. W.; Fesinmeyer, R. M.; Andersen, N. H. *Nat. Struct. Biol.* **2002**, *9*, 425-430.

(46) Erdelyi, M.; Langer, V.; Karlen, A.; Gogoll, A. *New Journal of Chemistry* **2002**, *26*, 834-843.

(47) Smith, C. K.; Regan, L. *Acc. Chem. Res.* **1997**, *30*, 153-161.

(48) de Alba, E.; Jimenez, M. A.; Rico, M. *J. Am. Chem. Soc.* **1997**, *119*, 175-183.

(49) Ramirez-Alvarado, M.; Blanco, F. J.; Serrano, L. *Nat. Struct. Biol.* **1996**, *3*, 604-612.

(50) Syud, F. A.; Stanger, H. E.; Gellman, S. H. *The Journal of the American Chemical Society* **2001**, *123*, 8667-8677.

(51) Griffiths-Jones, S. R.; Maynard, A. J.; Searle, M. S. *J. Mol. Biol.* **1999**, *292*, 1051-1069.

(52) Arrondo, J. L. R.; Blanco, F. J.; Serrano, L.; Goni, F. M. *FEBS Lett.* **1996**, *384*, 35-37.

(53) Colley, C. S.; Griffiths-Jones, S. R.; George, M. W.; Searle, M. S. *Chem. Comm.* **2000**, 593-594.

(54) Gibbs, A. C.; Kondejewski, L. H.; Gronwald, W.; Nip, A. M.; Hodges, R. S.; Sykes, B. D.; Wishart, D. S. *Nat. Struct. Biol.* **1998**, *5*, 284-288.

(55) Jelokhani-Niaraki, M.; Prenner, E. J.; Kondejewski, L. H.; Kay, C. M.; McElhaney, R. N.; Hodges, R. S. *J. Peptide Res.* **2001**, *58*, 293-306.

(56) Stanger, H. E.; Gellman, S. H. *J. Am. Chem. Soc.* **1998**, *120*, 4236-4237.

(57) Krimm, S.; Bandekar, J. *Adv. Protein Chem.* **1986**, *38*, 181-364.

(58) Susi, H.; Byler, D. M. *Methods Enzymol.* **1986**, *130*, 290-311.

(59) Surewicz, W. K.; Mantsch, H. H. *Biochim. Biophys. Acta* **1988**, *952*, 115-130.

(60) Rahmelow, K.; Hubner, W.; Ackermann, T. *Analytical Biochemistry* **1998**, *257*, 1-11.

Chapter 2

Materials and Methods

MATERIALS AND METHODS

An overview of the materials and methods discussed in subsequent chapters is described here. Details omitted from this chapter are presented in the relevant locations elsewhere in the dissertation.

Peptide Samples

Cyclic Peptides. The cyclic peptides studied in this research were synthesized by Alan Gibbs in the laboratory of Prof. David Wishart at the University of Alberta, Canada. Gibbs *et al.* performed nuclear magnetic resonance (NMR) and circular dichroism (CD) studies on cyclic peptides with varying ring size and found that peptides with a periodicity of 4n+2 exhibit β-sheet structure.[1] Based on this evidence, cyclic peptides having 6, 10, and 14 amino acid residues were selected for study in this research. Peptides were received in crystalline form and dissolved in D_2O for lyophilization. Lyophilized peptide samples were re-dissolved into D_2O solvent before injecting them into a sample cell using a syringe (discussed later). The reference solution for the cyclic peptides consisted of deuterated solvent with trifluoroacetic acid (TFA) in amounts qualitatively comparable to that of the sample.

Linear Peptides. Linear peptides H1, H1a, and H3 were synthesized in the laboratory of Prof. Niels H. Andersen by R. Matthew Fesinmeyer at the University of Washington, Seattle. As is commonly found in β-sheet peptides, H1 has very limited solubility. When the terminal isoleucine residue of H1 is substituted with alanine, H1a is formed. This substitution of only one amino acid dramatically improved the solubility of H1a as compared to H1. H3 peptide consists of 12 amino acids with the hydrophobic core moved closer to the β-turn region than in H1a. The linear peptides used in this research

were each lyophilized in D_2O to exchange amide protons. The solvent for these peptides consisted of D_2O and hexafluoroisopropanol (HFIP). The addition of HFIP is necessary to obtain cold-denaturation for the H1 and H1a peptides, while H3 requires an alcohol co-solvent to induce structure at low temperatures. Reference solutions for the linear peptides contained hexafluoroisopropanol (HFIP) in D_2O in the same amounts as the sample solvent. TFA was also present in the sample as a result of the HPLC purification method. However, TFA was not added to the reference solution to match the sample TFA content of the linear peptides as was previously done for the cyclic peptides.

Trifluoroacetic Acid Impurity. One of the problems encountered in studying both the cyclic and non-cyclic peptides described above is the large amount of trifluoroacetic acid (TFA) impurity that is present in the sample. TFA is present as a result of the HPLC purification methods used to elute the peptide from the chromatography column. Although a spectroscopically silent molecule would be a more favorable counter-ion, TFA has been found to be the most effective for eluting maximum amounts of peptide. Attempts to negate or reduce the appearance of TFA in the amide I′ region include centrifugation and addition of TFA to the reference solution in amounts comparable to the sample. In the case of centrifugation, the supernatant contains the same amount of TFA as the sample. However, other impurities, presumably acetate from the filter material, created an unequal TFA match between the sample and reference solutions. The addition of TFA to the reference solution is a feasible means of eliminating the appearance of most of the TFA when the sample and reference traces are ratioed. The benefit of adding TFA to the reference solution was demonstrated for the cyclic peptides when the instrument response and the reference solution were deconvolved from the

sample trace. The relaxation kinetics observed for H1a and H3 were not close enough to the instrument response to warrant deconvolution. The prominent amide I′ signature of TFA may be due to dimerization of the molecules which enhances the carbonyl stretching mode. TFA appears in the amide I` region (1675 – 1680 cm^{-1}) in an area that does not obscure the low-frequency β-sheet (1620 – 1635 cm^{-1}) or the bulk of the random coil region (1655 cm^{-1}), and therefore, no attempts were made to remove this impurity from the linear peptide samples of H1a and H3. However, it is noteworthy that early time-scale kinetics for the linear peptides seem to indicate that TFA may have a fast kinetic component. Any kinetics related to TFA in the linear peptide data were omitted from the fitting procedure by normalizing the difference spectra to either 110 ns or 300 ns.

Lyophilization. Peptide samples dissolved in D_2O underwent a process of freeze / pump / thaw in order to exchange amide protons for deuterated hydrogen. An incomplete exchange of amide protons in the sample causes H-O-D artifacts to appear in the absorbance spectra. These artifacts result in baseline problems due to drifting in the absorbance spectra of the amide I′ region.

Sample Cells

Successful sample cell construction is an art that results from the numerous steps and components required for cleaning and assembling the pieces. While there are likely several regimes which can be followed with favorable outcomes, the following description of sample cell cleaning and assembly was found to be effective in this research.

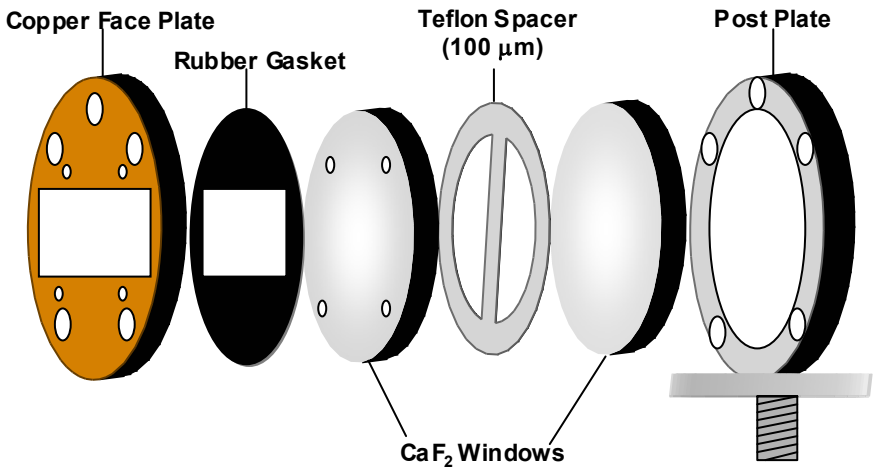

Figure 1 Sample cell components. Peptide samples were injected into a fully assembled sample cell.

Cleaning Windows. Calcium fluoride (CaF_2) windows were used for all infrared measurements because they provide a spectral window in the range of 0.13 – 7.0 μm.[2] CaF_2 windows can be cleaned in a number of ways using various solutions. The method of cleaning used in this research was based primarily on hot, soapy water followed by rinsing with 18 MΩ water, and finally, a thorough cleaning with methanol.

Sample Cell Assembly. The sample cell is comprised of several pieces which are shown in Figure 1. The heart of the sample cell is the calcium fluoride (CaF_2) windows which are sandwiched together using heat resistant vacuum grease that is lightly coated onto the Teflon spacer to prevent smearing. All of the samples described in this dissertation used a 100 μm spacer. A rubber gasket is placed between the copper face plate and the CaF_2 windows which are then positioned on the back post plate and held together by four screws. The back post plate has a ring of indium wire around the opening rim to promote even heating of the windows as well as to prevent chipping of the windows against the surface. An important detail in the assembly process is the fact that the four screws holding the sample cell together should be tightened in an alternating fashion to create even pressure on the windows in order to prevent breakage.

Spacer Measurements. The quality of a sample cell assembly was quantitatively assessed by measuring etalon spacing in relation to the centerburst of an interferogram. Spacer measurements of both the sample and reference sides of an empty cell were typically done using a Biorad FTS-40 spectrometer. Occasionally the Biorad FTS-60 was used for spacer measurements, and it was interesting to note that this instrument tended to produce larger spacer distances but similar relative differences between the sample and reference sides of the cell as compared to the FTS-40 instrument. Differences between the spacer

distances on the sample and reference sides of a cell differed by less than 1 μm in well-built cells.

Loading the Cell. Fully assembled cells with known pathlengths were loaded with sample and reference solutions using a syringe. Pressure relief needles were placed in the CaF_2 window hole opposite of where the syringe injection occurred. Problems in loading the sample and / or reference solutions can occur if there are bubbles in the syringe or if the windows are not entirely clean.

Concentration Determination. Sample concentrations were measured directly inside the cell. The cell was mounted onto a small pedestal and placed inside a UV-Vis spectrometer where the absorbance of tryrosine in the peptide was measured. The concentration of tyrosine was calculated using an extinction coefficient of $\varepsilon = 1405$ L/(mol*cm).[3]

Infrared Studies

Fourier Transform Infrared Studies. Equilibrium infrared spectroscopy was used to obtain absorbance spectra for peptide samples over a range of temperatures from ~1 – 80 °C. A cell containing both the sample and reference solutions was equilibrated at a given temperature prior to measuring the single beam transmission spectra of each solution. Following the data collection at a given temperature, the temperature was increased, and the cell equilibrated at a new temperature before the next measurement was acquired. The end result was a single beam transmission spectrum for both the sample and the reference solutions at each temperature. The single beam transmission spectra were converted to absorbance spectra by taking the –log (sample spectrum / reference spectrum).

Baseline corrections were applied to absorbance spectra to account for distortions that occur due to differences in the H-O-D content of sample and reference solutions. This problem of baseline drifting is due to incomplete exchange of amide protons in the sample during lyophilization. Baseline corrections were made by choosing a point on the baseline on each side of the absorbance peaks and normalizing these points to a line passing through both points. The corrected absorbance spectra were used to generate difference spectra, second derivative spectra, melt curves, and van't Hoff plots.

Difference spectra were obtained by subtracting the highest baseline-corrected, temperature-dependent absorbance spectrum from each spectra of lower absorbance. The result of these subtractions was enhanced resolution of the features of interest, namely, the β-structure region and the disordered polypeptide component. Information from the difference spectra were used for two primary purposes. First, information from the difference spectra was used to determine the appropriate wavenumber to probe for maximum structural changes for kinetic experiments. Also, the β-structure melt maximum found by difference spectra identified the frequency for a melt curve plot from the absorbance spectra. Secondly, the change in absorbance between temperatures was used to calibrate the magnitude of the temperature jumps anticipated from kinetics experiments.

Temperature Jump Studies. The kinetics of small, β-sheet peptides were measured using infrared temperature jump (T-jump) spectroscopy. T-jump measurements detect physical changes that occur due to a sudden increase in temperature. A schematic of the T-jump setup is shown in Figure 2. The T-jump setup consisted of two lasers, a pulsed Nd:YAG and a continuous wave (CW) lead salt diode laser, which were used for pump and probe

measurements, respectively. The pump laser had a fundamental frequency of 1064 nm which was passed into a Raman shifter filled with hydrogen gas. The first Stokes shift of the 1064 nm fundamental (2 μm) beam was separated from the other frequencies using a Pellin Broca prism. The 2 μm light was used to pump a weak D_2O vibrational overtone at ~6 cm^{-1}.[4] The pump beam created an instantaneous energy transfer from the solvent to the peptide to incite unfolding or folding, depending on the sample. The diode laser was tuned to probe the frequency of interest which was detected by a mercury – cadmium – tellurium (MCT) detector.

Temperature Jump Calibration

The magnitude of temperature jumps was determined based on calibration curves of the calculated change in absorbance for the reference side of the sample cell. Calibration curves were obtained either from temperature-dependent FTIR or T-jump measurements.

Cyclic Peptide Calibration Curve. Temperature jumps for the three cyclic peptides were determined based on a D_2O calibration curve which was acquired from the T-jump setup (Figure 3). The relative absorbance of D_2O at 1623.40 cm^{-1} was calculated (Table 1) and fit to a single exponential.

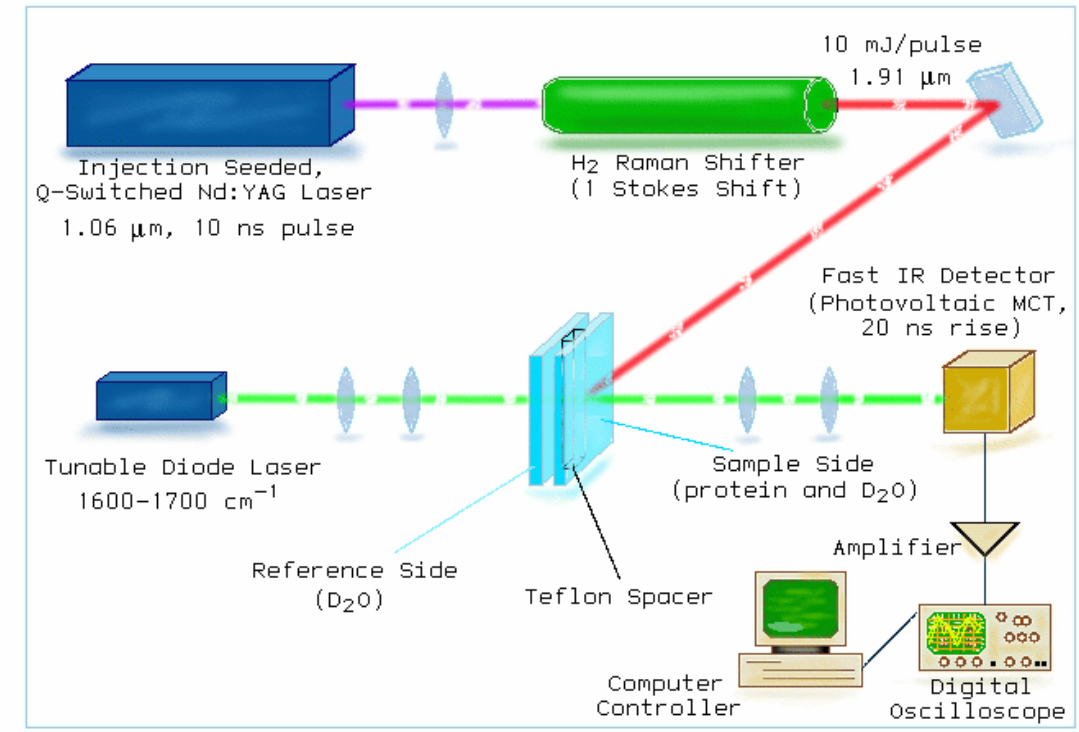

Figure 2 Temperature jump apparatus schematic.

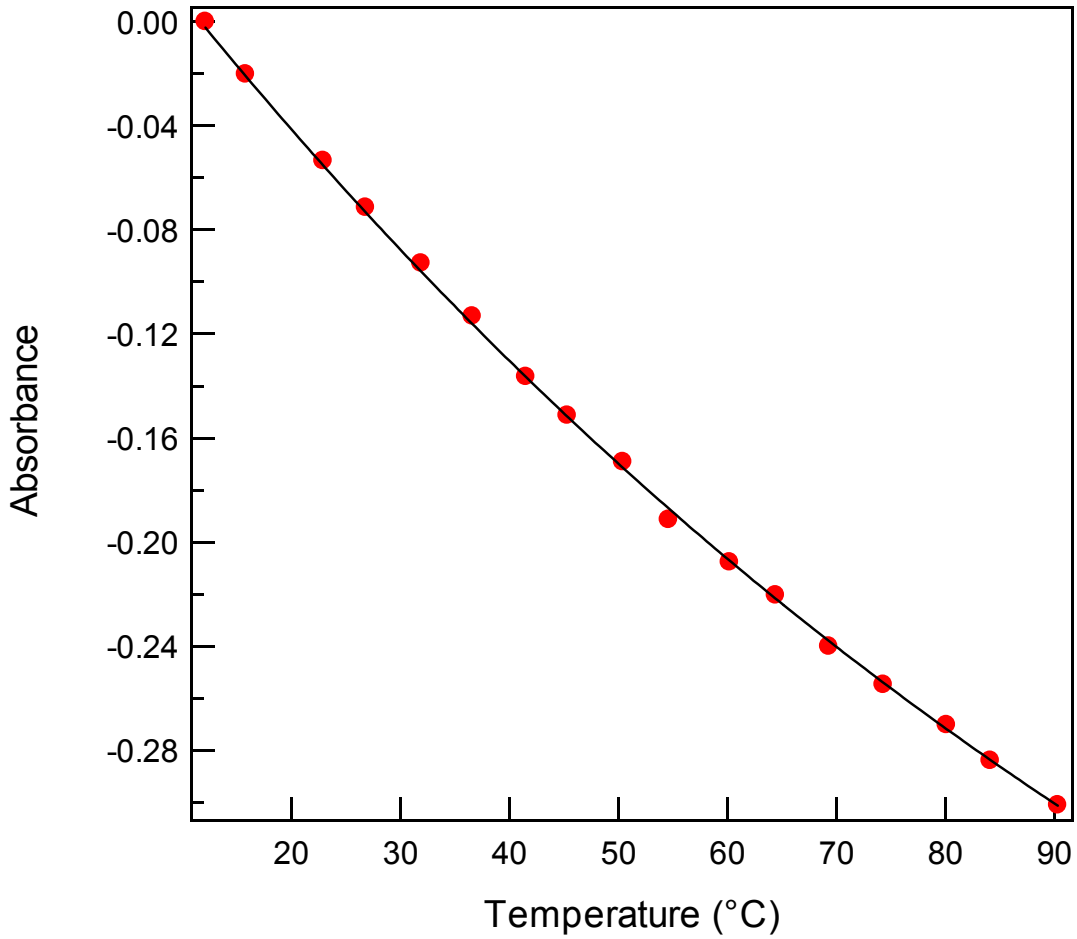

Figure 3 D_2O calibration curve for cyclic peptides. These data were obtained from a temperature jump calibration at 1623.40 cm^{-1}. Red dots represent calculated absorbance values which were fit to a single exponential (black trace).

Table 1 Relative absorbance values of D_2O. These data were used to plot the calibration curve for cyclic peptides shown in Figure 3.

Temperature (◦C)	Transmission	Calculated Absorbance
12.1	168.0	0
15.8	176.0	-0.02020
22.9	190.0	-0.05344
26.8	198.0	-0.07136
31.9	208.0	-0.09275
36.6	218.0	-0.11315
41.5	230.0	-0.13642
45.3	238.0	-0.15127
50.4	248.0	-0.16914
54.6	261.0	-0.19133
60.2	271.0	-0.20766
64.4	279.0	-0.22029
69.3	292.0	-0.24007
74.3	302.0	-0.25470
80.1	313.0	-0.27024
84.1	323.0	-0.28389
90.3	336.0	-0.30103

The following equations are used to find the change in temperature using the calibration curve:

$$Abs_{Tinitial} = a + be^{-(c * Tinitial)} \quad \text{(Equation 1)}$$

$$Abs_{(Tinitial + \Delta T)} = a + be^{-[c * (Tinitial + \Delta T)]} \quad \text{(Equation 2)}$$

$$Abs_{Tinitial} - Abs_{(Tinitial + \Delta T)} = be^{-(c * Tinitial)} - be^{-[c * (Tinitial + \Delta T)]} \quad \text{(Equation 3)}$$

In these equations, a, b, and c represent the coefficients found from the exponential fit of the calibration curve, while the change in absorbance between $T_{initial}$ and ΔT was measured from the calibration graph.

H1a Peptide. Absorbance values for a calibration curve can be calculated from either FTIR or T-jump data measured at several temperatures. For H1a peptide, a comparison of the relative absorbance values from FTIR versus temperature jump measurements was found to have relatively good agreement when fit to a linear equation (Figure 4). Although the FTIR data are not as well-suited to a linear fit as the calculated absorbance values from the temperature jump studies, they provide a useful approximation for comparison purposes. A slope of -0.0047982 ± 0.000166 was measured for the FTIR values, and a slope of -0.0050399 ± 0.00017 was determined for the temperature jump trace. The slope of the temperature jump trace was used to calculate the changes in temperature measured during a T-jump experiment. For example, the absorbance of a reference trace at 1.96×10^{-6} s divided by the slope of the temperature jump calibration line equals the change in temperature observed at that time (ΔT).

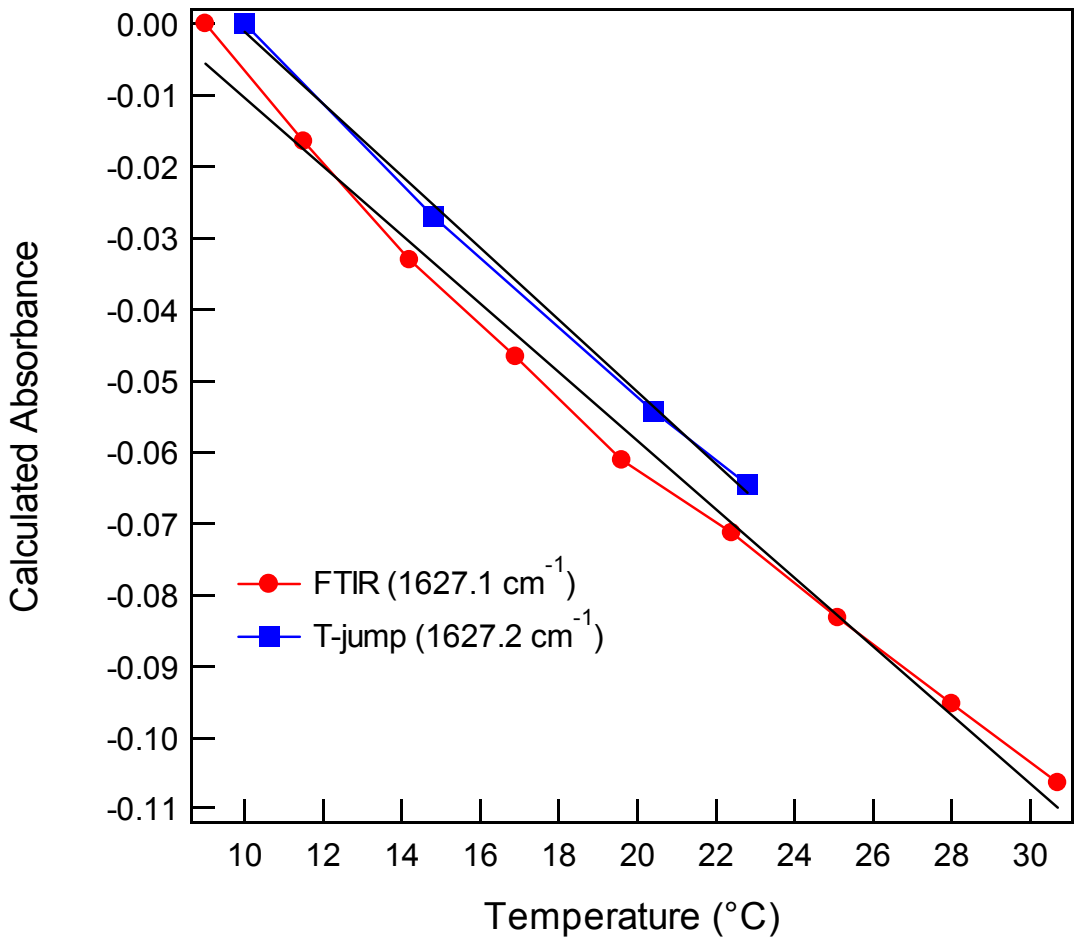

Figure 4 Comparison of absorbance values from FTIR versus T-jump experiments. Linear fits measured slopes of m = -0.0047982 ± 0.000166 for FTIR data and m = -0.0050399 ± 0.00017 for T-jump data.

Table 2 Data used for FTIR trace in Figure 4. The relative absorbance was calculated using the formula $A = (I + I_o)/I_o$. Thermocouple measurements are accurate to ± 0.1 °C.

Temperature (◦C)	Transmission	Calculated Absorbance
9.0	7.3112	0
11.5	7.5938	-0.0165
14.2	7.8895	-0.0331
16.9	8.1390	-0.0466
19.6	8.4150	-0.0611
22.4	8.6145	-0.0712
25.1	8.8536	-0.0831
28.0	9.1028	-0.0952
30.7	9.3374	-0.1062

Table 3 Data used for T-jump trace in Figure 4. Data for the average values of relative absorbance used to create the temperature jump calibration curve in Figure 4. The standard deviation of the pooled variance is also reported.

	Average Temperature (◦C)	Average Voltage (mV)	Average Calculated Absorbance
	10.0	407	0
	14.8	436	-0.02939
	20.4	460	-0.05316
	22.8	471	-0.06343
s.d.pooled	± 0.0	± 2	± 0.00156

An FTIR calibration curve can also be used to determine the amount of the temperature jump assuming that the FTIR data tracks the kinetic measurements reasonably well. The advantage of using an FTIR calibration curve is that more data points are available to produce a more accurate fit using an exponential function rather than a linear fit. Figure 5 illustrates the FTIR calibration curve at 1627.1 cm^{-1} for 5% (vol) HFIP from 4 – 77 °C. The calculated relative absorbance trace was fit in the region from 4 – 40 °C with a single exponential for the H1a peptide studies. Equation 3 was solved using MatLab software to find the change in temperature (ΔT) using the FTIR calibration curve.

A comparison of the results of T_{final} between FTIR and temperature jump calibration curves show insignificant differences when the standard deviation is calculated using pooling of variance. The standard deviation is determined in this way by averaging the values for temperatures at each point $(\overline{x_n} = (x_1 + ...x_n)/n)$, calculating the squared value of the data point minus the mean at that temperature $((x_n - \overline{x_n})^2)$, and adding the sum of the squares $(ss = \sum (x_n - \overline{x_n})^2)$. The degrees of freedom were found by subtracting the number of means from the number of total data points $(df = n - n_{\bar{x}})$. Finally, the pooled standard deviation is determined by taking the square root of the sum of squares divided by the degrees of freedom $(s.d._{pooled} = \sqrt{ss/df})$.

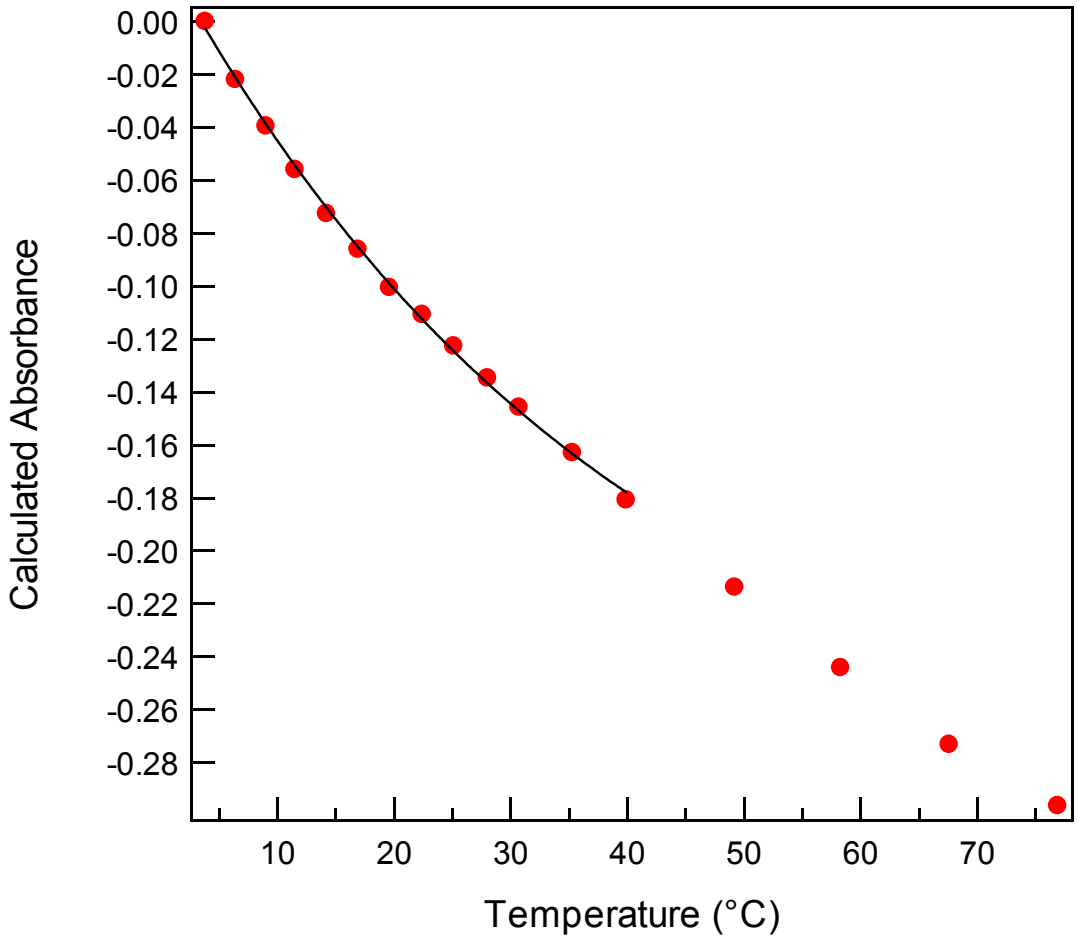

Figure 5 FTIR calibration curve for H1a peptide. The calculated relative absorbance of 5% (vol) HFIP was fit to a single exponential function from 4 – 40 °C.

Table 4 Data for FTIR and T-jump calibration curves with varied temperatures for H1a peptide. Comparisons of calculated T-jumps for varied $T_{initial}$ using the FTIR calibration curve fit with an exponential function and the T-jump calibration curve fit with a linear function. Negative values for ΔT using the FTIR curve result from a decrease in the measured absorbance and must be subtracted from $T_{initial}$. Values for T-jump ΔT values are positive because a negative absorbance is divided by a negative slope to produce a positive result and are therefore added to $T_{initial}$. A pooled standard deviation is calculated for these measurements. All units in this table are °C.

	FTIR Calibration Curve		
	Tinitial	ΔT	Tfinal
	10.0	-6.1	16.1
	14.8	-5.9	20.7
	20.4	-5.5	25.9
	22.8	-5.8	28.6
s.d. pooled	0.0	0.6	0.6
	T-jump Calibration Curve		
	Tinitial	ΔT	Tfinal
	10.0	8.5	18.5
	14.8	7.4	22.2
	20.4	5.9	26.3
	22.8	5.8	28.6
s.d. pooled	0.0	0.8	0.8

Table 5 Data for FTIR and T-jump calibration curves with varied wavenumbers for H1a peptide. These data are the comparisons between average temperatures obtained from FTIR and T-jump calibration curves. Standard deviations are also listed.

FTIR Calibration Curve		
Average Tinitial	Average ΔT	Average Tfinal
12.4 $\pm$ 0.1	-7.8 $\pm$ 0.7	20.3 $\pm$ 0.8
T-jump Calibration Curve		
Average Tinitial	Average ΔT	Average Tfinal
12.4 $\pm$ 0.1	10.2 $\pm$ 1.0	22.7 $\pm$ 1.1

H3 Peptide. Calibration curves for H3 peptide were obtained from both FTIR and T-jump measurements for 21% (vol) HFIP in D_2O. A linear fit to the FTIR trace had a slope of -0.0043163 ± 0.000118 while the T-jump fit had a slope of -0.016505 ± 0.000457. Figure 6 shows the discrepancy between the calculated absorbance values for the reference solution using these two experimental methods. These differences indicate a mis-alignment of one or both of the setups. The data used to generate Figure 6 are presented in Tables 6 and 7 for FTIR and T-jump traces, respectively. An exponential fit of the FTIR data (Figure 7) shows improvement over the linear fit illustrated in Figure 6. Calculations of the change in temperature were done using the exponential FTIR fit (Figure 7) and the linear T-jump fit (Figure 6). The results of these fits are compared in Table 8 for temperature-dependent kinetic measurements and in Table 9 for wavenumber-dependent measurements. Although values for both FTIR and T-jump calibration curves were obtained for H3 peptide, the change in temperature measured by T-jump experiments is believed to be the most accurate reflection of the actual change in temperature since temperature changes were being produced by T-jump measurements.

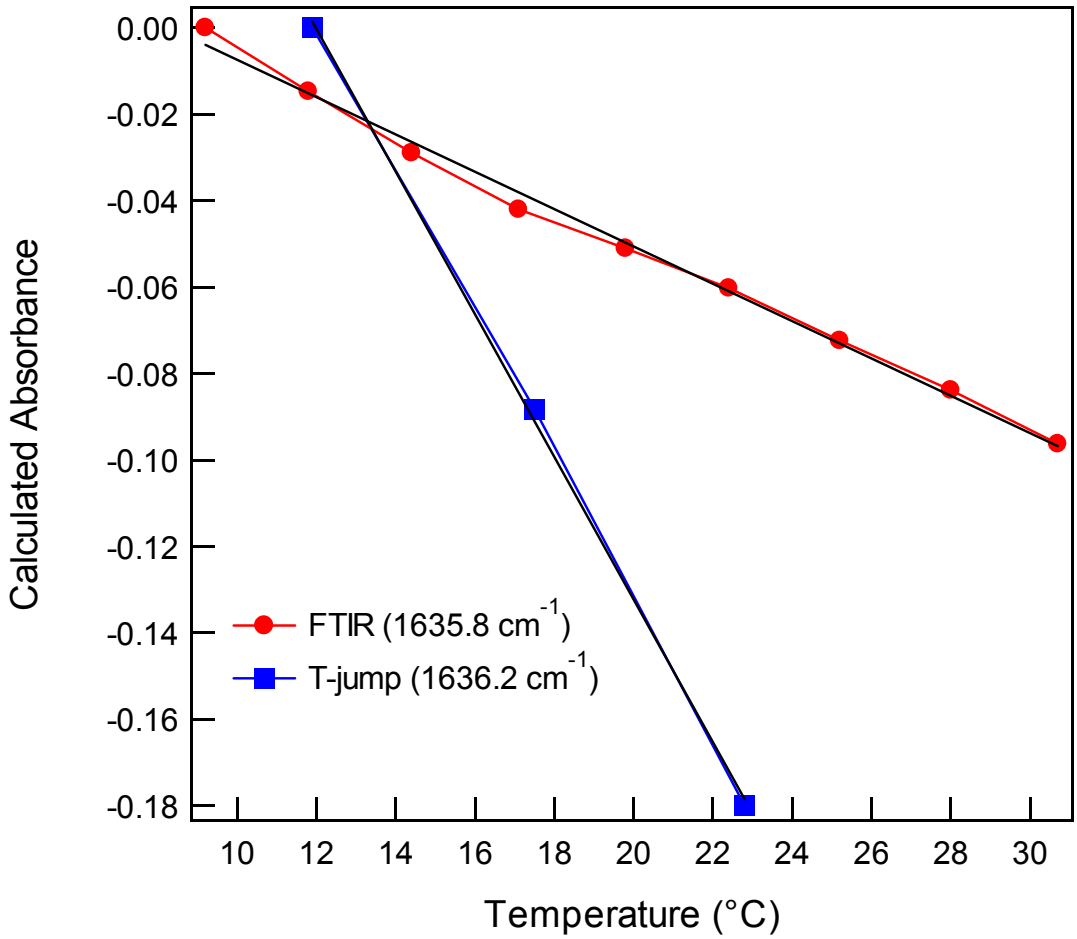

Figure 6 FTIR and T-jump calibration curves for H3 peptide. Linear fits were applied to this data; the slope of the FTIR fit was -0.0043163 ± 0.000118 and the T-jump slope fit had a value of -0.016505 ± 0.000457.

Table 6 FTIR calibration curve for H3 peptide at 1635.8 cm^{-1}.

Temperature (◦C)	Transmission	Calculated Absorbance
9.2	9.3833	0
11.8	9.7074	-0.0147
14.4	10.0300	-0.0289
17.1	10.3360	-0.0420
19.8	10.5530	-0.0510
22.4	10.7790	-0.0602
25.2	11.0850	-0.0724
28.0	11.3810	-0.0838
30.7	11.7120	-0.0963

Table 7 T-jump calibration curve for H3 peptide at 1636.2 cm^{-1}.

	Average Temperature (◦C)	Average Voltage (mV)	Average Calculated Absorbance
	11.9	204	0
	17.5	250	-0.08815
	22.8	308	-0.17998
s.d.pooled	± 0.0	± 9	± 0.00890

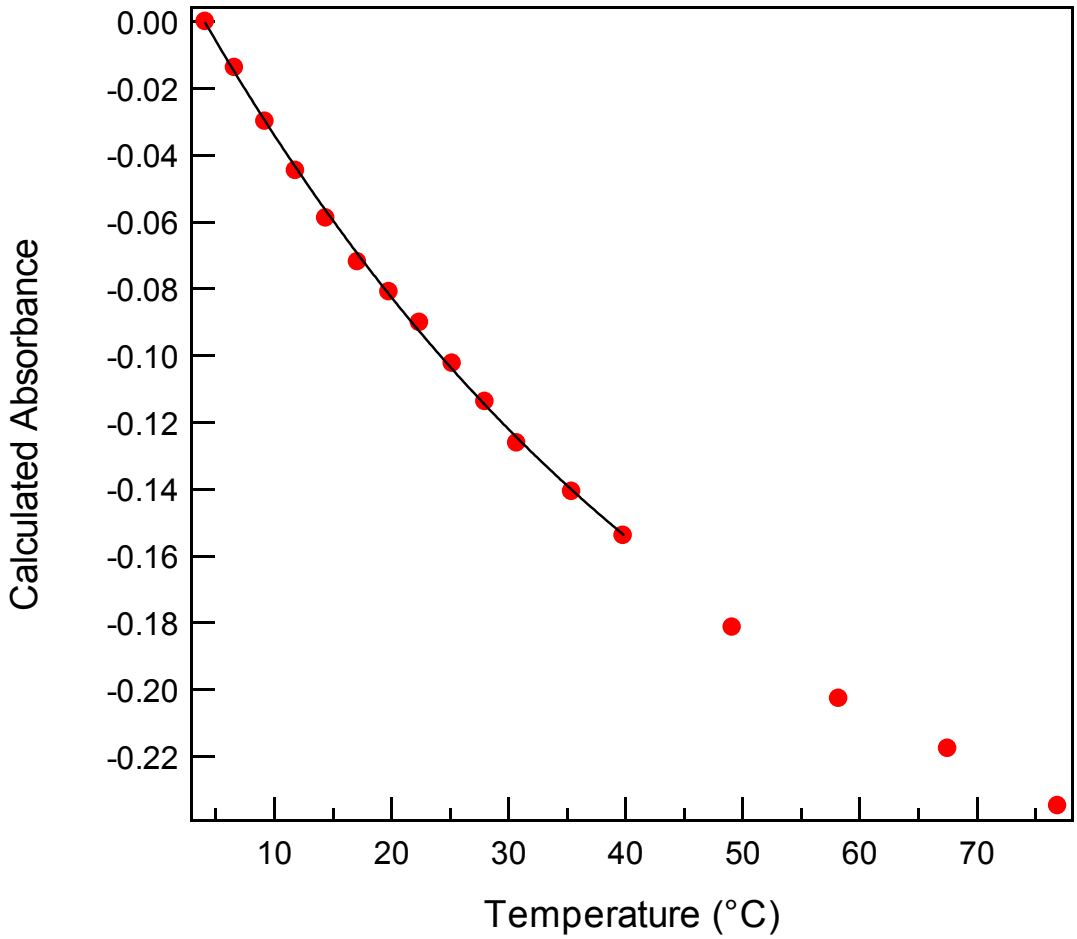

Figure 7 FTIR calibration curve for H3 peptide. The calculated relative absorbance of 21% (vol) HFIP was fit to a single exponential function from 4 – 40 °C.

Table 8 T-jump measurements for temperature-dependent data of H3 peptide using FTIR and T-jump methods.

	FTIR Calibration Curve		
	Tinitial	ΔT	Tfinal
	11.9	-7.9	19.8
	17.5	-7.9	25.4
	22.8	-8.7	31.5
s.d. pooled	0.0	1.2	1.3
	T-jump Calibration Curve		
	Tinitial	ΔT	Tfinal
	11.9	3.4	15.2
	17.5	3.0	20.5
	22.8	3.0	25.8
s.d. pooled	0.0	0.5	0.6

Table 9 T-jump measurements for wavenumber-dependent data of H3 peptide using FTIR and T-jump methods.

FTIR Calibration Curve		
Average Tinitial	Average ΔT	Average Tfinal
12.0 $\pm$ 0.1	-8.8 $\pm$ 1.0	20.9 $\pm$ 1.0
T-jump Calibration Curve		
Average Tinitial	Average ΔT	Average Tfinal
12.0 $\pm$ 0.1	3.8 $\pm$ 0.5	15.8 $\pm$ 0.5

REFERENCES

(1) Gibbs, A. C.; Kondejewski, L. H.; Gronwald, W.; Nip, A. M.; Hodges, R. S.; Sykes, B. D.; Wishart, D. S. *Nat. Struct. Biol.* **1998**, *5*, 284-288.

(2) http://www.janostech.com/techinfo/caf2.html.

(3) http://omlc.ogi.edu/spectra/PhotochemCAD/html/tyrosine.html.

(4) Werner, J. H.; Dyer, R. B.; Fesinmeyer, R. M.; Andersen, N. H. *J. Phys. Chem. B* **2002**, *106*, 487-494.

Chapter 3

Cyclic β-Sheet Peptides

ABSTRACT

The thermal unfolding of a series of 6-, 10-, and 14-mer cyclic β-hairpin peptides was studied to gain insight into the mechanism of formation of this important secondary structure. The thermodynamics of the transition were characterized using temperature dependent FTIR spectroscopy. Thermodynamic data were analyzed using a two-state model which indicates increasing cooperativity along the series. The relaxation kinetics of the peptides in response to a laser induced temperature jump (T-jump) were probed using time-resolved infrared spectroscopy. Single exponential relaxation kinetics were observed and fit with a two-state model. The folding rate determined for these cyclic peptides is accelerated by some two orders of magnitude over the rate of a linear peptide that forms a β-hairpin. This observation supports the argument that the rate limiting step in the linear system is either stabilization of compact collapsed structures or rearrangement of collapsed structures over a barrier to achieve the native interstrand registry. Small activation energies for folding of these peptides obtained from an Arrhenius analysis of the rates imply a primarily entropic barrier, hence an organized transition state having specific stabilizing interactions.

INTRODUCTION

Small peptide models have proven to be invaluable experimental systems for studying the fundamental processes of protein folding (reviewed in [1], [2]). Many of the essential elements of protein folding, including hydrophobic collapse, hydrogen bond formation, and side-chain packing have been observed in the folding of peptide models. [3-6] Studies of helical peptides have been particularly successful in elucidating the dynamics of helix nucleation and propagation, and helix-helix interactions.[7,8] The study of β-structures has been more difficult due to the scarcity of suitable model systems. Some of the problems associated with β-sheet peptide models include their tendency to be large, prone to aggregate, not very stable, and low in secondary structure content.

Significant breakthroughs have been made recently in the design of stable and soluble peptides with β-turn and β-sheet structures.[9-13] The dynamics of folding of one such system, the 16 residue C-terminal β-hairpin fragment of protein G, have been studied by Muñoz *et al*.[14,15] They observed apparent two-state relaxation kinetics of the β-hairpin structure using laser induced temperature jump (T-jump) and time-resolved fluorescence measurements of the native Trp in this fragment. The relaxation kinetics were analyzed using a statistical mechanical kinetic zipper model. Using this model, they calculate a folding lifetime of 6 μs for the hairpin. This is substantially slower than the folding lifetimes of about 200 ns reported for similarly sized helical peptides under similar conditions.[7,8] The slower rate is rationalized within the kinetic zipper model by assuming that the hydrogen bond propagation rate is the same in both instances which implies that the nucleation of a stable turn is much slower than helix nucleation. Muñoz

et al. postulate that hairpin nucleation is slow because it requires a cooperative stabilization by hydrophobic side chain interactions.

The folding of the β-hairpin fragment of protein G has also been studied using Langevin simulations of minimal off-lattice models [16] and all atom molecular dynamics [17] and multicanonical Monte Carlo simulations.[18] These studies find that the hairpin folds via discrete intermediates, or through a hierarchy of structural changes involving hydrophobic collapse, hydrogen bond formation, and side chain ordering. The model of Muñoz *et al.* suggests that folding nucleates at the turn, followed by a zipping of the structure. The hydrophobic core is formed subsequent to the turn, and stabilizes the structure. In contrast, the simulations of Dinner *et al.* predict that hydrophobic collapse and rearrangement to produce a native-like topology is the key initial step, followed by hydrogen bond formation. Thus, formation of a collapsed, native-like topology serves as a nucleating event, with hydrogen bonds propagating outward from the hydrophobic core. These models predict fundamentally different roles for the formation of the turn versus the hydrophobic core in the folding mechanism of this β-hairpin structure. In either case, hydrogen bond formation is seen as a fast propagation step that follows the nucleating event. The relative importance of hydrophobic interactions versus turn formation in facilitating chain collapse and formation of the native topology remains unresolved. The rate of hydrogen bond propagation and how it compares to that in helical systems is also not known.

We have explored the dynamics of β-turn formation and hydrogen bond propagation within a series of 6-, 10-, and 14-mer cyclic β-hairpin analogs of Gramicidin S (GS) using equilibrium FTIR spectroscopy and T-jump relaxation probed by time-

resolved IR spectroscopy. Cyclic peptides have gained increasing attention in recent years as a result of their antimicrobial properties and membrane permeation capabilities.[19] GS is one such cyclic peptide [cyclo(-Val-Orn-Leu-$_D$-Phe-Pro-)$_2$] having antibiotic properties and an amphipathic nature. Studies of the sequence-dependent biophysical properties of GS analogues have been used to examine the effects of hydrophobicity, amphipathicity, and β-hairpin turn propensity.[20-24] These studies provide useful insight into the antimicrobial and hemolytic activities of GS. What is lacking, however, is an understanding of the structural dynamics that are critical to the biological activity of GS.

The cyclic 6-, 10-, and 14-mer β-hairpin peptides are excellent model systems because a study of length dependence of the dynamics is possible, with the number of hydrogen bonds increasing from two to four to six along the series. Additionally, these peptides are sterically constrained in their search of conformational space, and consequently, turn formation and hydrogen bond propagation can be measured separately from chain diffusion (collapse) processes. The solution structures of the 6-, 10-, and 14-mer peptides have been solved by NMR.[25] They form stable antiparallel β-hairpin structures, bordered by two type II′ β-turns. We have modeled the relaxation behavior of these peptides using a two-state model, from which we extract folding rates and activation parameters.

MATERIALS AND METHODS

Peptides. Synthesis of the cyclic β-hairpin peptides was performed by Gibbs *et al.* [25] with the first and last residues in the sequence linked in the cyclization. The sequences of the peptides used in these studies are as follows, where Tyr residues are of D stereochemistry:

6-mer: K<u>Y</u>PK<u>Y</u>P
|_____|

10-mer: VKL<u>Y</u>PVKL<u>Y</u>P
|_____|

14-mer: VKLKV<u>Y</u>PLKVKL<u>Y</u>P
|_____|

The samples were purified by reverse phase HPLC and deuterium exchanged by repeated lyophilization from D_2O. Trifluoroacetic acid (TFA), which was used in the HPLC purification, was present as an impurity in all samples. Samples were dissolved in D_2O (99.9%, Sigma), and final concentrations were found to be in the range of 1 - 4 mM as determined by the UV absorption of Tyr at 274 nm.

Infrared Spectroscopy. The equilibrium melting behavior of the cyclic peptides was studied using Fourier Transform Infrared (FTIR) spectroscopy. FTIR spectra were collected on a Biorad FTS-40 interferometer using a temperature controlled IR cell. The IR cell contained both the sample and a D_2O reference solution with TFA between CaF_2 windows with a 100 μm spacer. The cell is translated laterally under computer control, to acquire matching sample and reference single beam spectra, and the protein absorption spectrum is computed as $-\log(I_{samp}/I_{ref})$. It is critical to match the sample and reference solutions as closely as possible, particularly with regard to H_2O content, because of the overlap of the temperature dependent spectrum of HOD with the protein spectrum in the region of interest. Temperature-dependent spectra in the amide I′ (the prime indicates the deuterated amide group) region from ~1600-1700 cm^{-1} were baseline corrected using a linear baseline to account for the small differences in the broad HOD absorption. The

baseline corrections required were typically smaller than 1 mOD, or less than 1% of the observed protein signal.

T-jump Relaxation Measurements. The T-jump relaxation apparatus has been described previously.[7] Briefly, a laser induced T-jump is used to rapidly shift the folding/unfolding equilibrium, and the relaxation kinetics are measured using time-resolved infrared spectroscopy. The T-jump perturbation generated by a laser heating pulse is faster than the molecular dynamics of interest. The T-jump pulse is generated by Raman shifting a Q-switched Nd:YAG (Spectra Physics DCR-4) fundamental at 1064 nm in H_2 gas (1-Stokes shift), producing a 10 ns pulse at 1.91 μm. The near infrared wavelength is partially absorbed by the D_2O ($\varepsilon \sim 6$ cm^{-1}, or 87% transmittance in a 100 μm path length cell), and the absorbed energy is rapidly thermalized within the irradiated volume. The magnitude of the T-jump produced depends on the per pulse energy and the focus of the laser, typically 40 mJ and 1mm spot diameter respectively, which yields an 11°C T-jump. The mid-IR probe beam is a continuous wave lead-salt diode laser (Laser Photonics) with a tunable output range of 1600-1700 cm^{-1}. The probe beam is focused to a 50 μm ($1/e^2$ diameter) spot at the center of the heated volume. Probing only the center of the heated volume ensures a uniform temperature distribution in the probe volume by avoiding the temperature gradient produced on the wings of the Gaussian pump beam.[26] The transient transmission of the probe beam through the sample is measured using a fast (100 MHz) photovoltaic MCT IR detector/preamplifier (Kolmar Technologies). Transient signals are digitized and signal averaged using a Tektronics digitizer (7612D). Instrument control and data collection are accomplished using a LabVIEW computer program.

Very high dynamic range is achieved in these transient IR measurements using a simple procedure to measure the total transmitted intensity of the probe beam independently from the transient change in the transmission due to the T-jump. The detector and amplifier are DC coupled to maximize the bandwidth of the measurement (to cover the range from 100 MHz – 1 Hz). The amplitude of the transmitted probe beam (I_0) is measured using an optical chopper, and the DC offset of the detector preamplifier is adjusted to null the DC signal. The transient signal (ΔI) is then measured in the presence of the pump beam, and the transient absorbance is computed as:

$$\Delta A = -\log [(I_o + \Delta I) / I_o] \qquad \text{(Eqn. 1)}$$

In this way, the full dynamic range of the detector, amplifier, and digitizer is exploited to measure the transient signal. Measurements of the transient absorbance for both the sample and the reference were collected from 10^{-9} to 10^{-1} s, and relaxation times were obtained using a deconvolution process described below.

Analysis of Kinetics Data. Accurate determination of the peptide relaxation kinetics requires deconvolution of the instrument response function from the observed kinetics. Very accurate deconvolution of the instrument response is possible because it is determined concurrently with each sample measurement under the exact same conditions. Using a macro created using IGOR (WaveMetrics, Inc.), the observed sample relaxation kinetics are fit as a function of the instrument response convolved with an exponential decay. The instrument response function for the system is taken to be the derivative of the reference trace, normalized to have an integral of 1 at the maximum of the reference trace. Normalizing the instrument response is necessary so that amplitudes represent changes in absorbance. The decay function used is an exponential decay with the

formula ($A*exp^{(-kT)}$), where A and k are the change in absorbance and the rate, respectively. The reported relaxation rates represent an average of at least 7 separate trials, and the reported uncertainties represent the standard deviation of the average values.

RESULTS

Equilibrium FTIR Studies. All three cyclic peptides adopt β-hairpin (folded) structures in solution at room temperature.[25] We have studied the temperature induced unfolding in the range from 1 – 85°C using FTIR spectroscopy. We focus on the amide I′ spectral region because this vibrational mode is an established indicator of secondary structure.[27,28] This broad, multicomponent band contains contributions from the entire polypeptide backbone, which in this case adopts either a β-sheet, β-turn, or disordered conformation. The absorption spectra as a function of temperature for the 6-, 10-, and 14-mer are shown in Figs. 1a, 2a, and 3a, respectively. The amide I′ maximum at room temperature is similar to that previously reported for GS in D_2O,[29] with a peak maximum at 1632 cm^{-1}. The changes with temperature are highlighted in the difference spectra for each peptide, in Figs. 1b, 2b, and 3b, respectively. These difference spectra are generated by subtraction of the lowest temperature spectrum from each of the absorbance spectra at higher temperatures. The amide I′ envelopes of all three peptides were simultaneously deconvolved using a multi-Gaussian global fitting routine in Igor (Wavemetrics). The number of subcomponents and their frequencies was determined from the second derivative of the absorbance spectra. The frequencies and peak areas from the global fit are reported in Table 1.

The deconvolution analysis reveals three components of the amide I′ band at 10 °C, centered near 1625, 1636, and 1658 cm^{-1} (Table 1, Figure 4). All three of these spectral components decrease in intensity with increasing temperature. These components of amide I′ arise from the folded structure, which is highly populated at low temperature, and are therefore due to the β-turn and antiparallel β-sheet backbone conformations present in the folded state. We assign the peak at ~1625 cm^{-1} to the β-turns on the basis of its low frequency (characteristic of β-turns) and constant intensity across the series (all three peptides contain two type II′ β-turns). Two peaks are observed for the β-sheet, consistent with the structure which contains inward and outward directed C=O groups, i.e., intra- and intermolecular (to water) hydrogen bonding, respectively. We assign the peak at ~1636 cm^{-1} to the inward directed C=O groups (intramolecular H-bonding) and the peak at ~1658 cm^{-1} to the outward directed C=O groups (intermolecular H-bonding to water). There are several lines of evidence that support these assignments. First, the peak at 1658 cm^{-1} is similar in frequency to that observed for disordered polypeptide and therefore, is most likely indicative of the C=O groups which are intermolecularly H-bonded to water. Second, the peak at 1658 cm^{-1} is always smaller than the 1636 cm^{-1} peak and altogether absent in the 6-mer. This absence of a peak for intermolecularly H-bonded carbonyl groups in the 6-mer is reasonable since both of the sheet residues in this peptide exhibit intramolecular H-bonding. In contrast, the 10-mer will have 4 intra- and 2 intermolecular-H-bonds, and the 14-mer will have 6 intra- and 4 intermolecular-H-bonds. Consequently, the intermolecular H-bonding band is expected to be weaker than the intramolecular H-bonding band, and both bands should increase in intensity along the series, which is what is observed. Finally, these assignments are

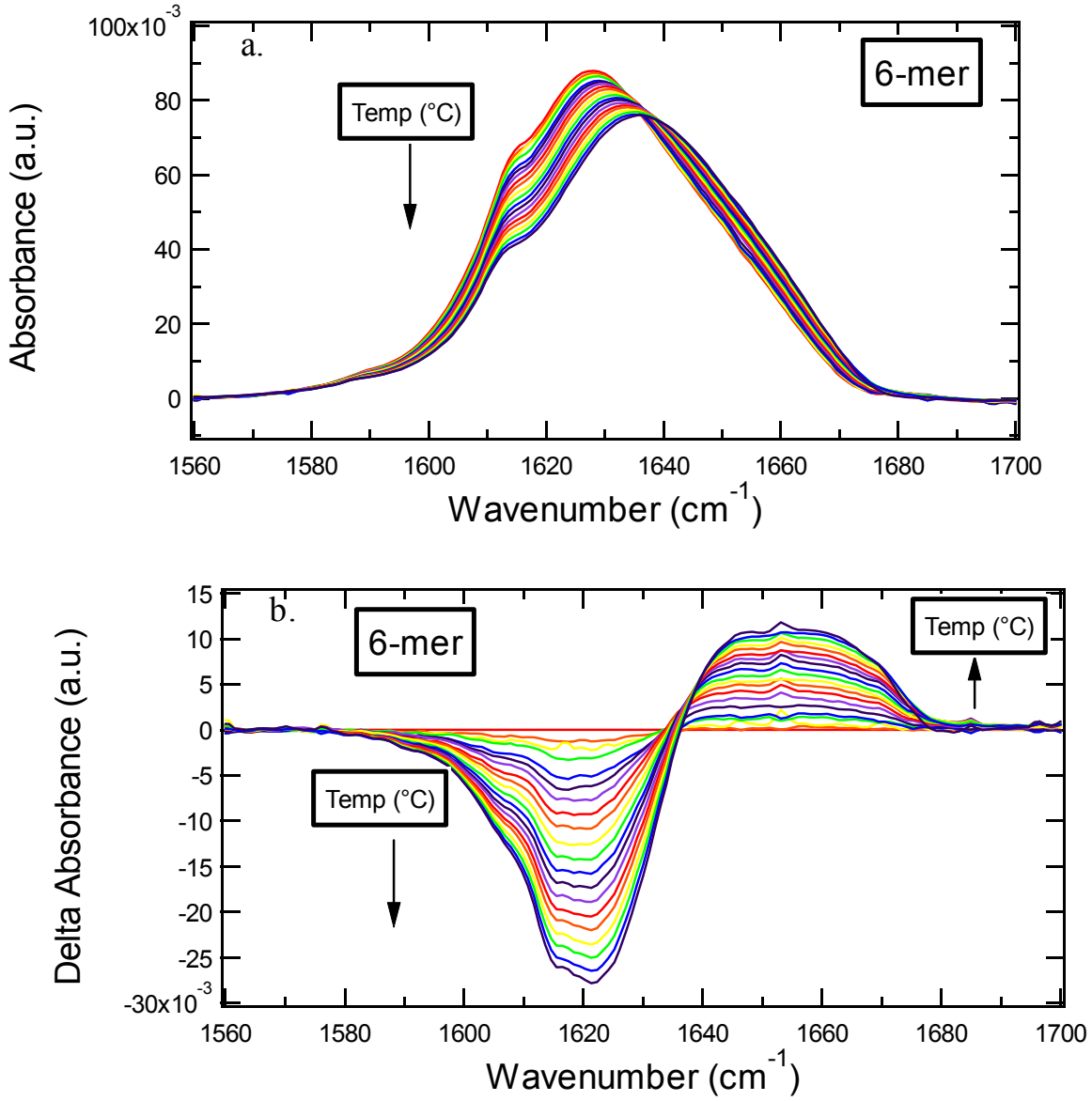

Figure 1 Temperature-dependent FTIR spectra for the 6-mer cyclic peptide, 3.4 mM in D_2O, minimal salt. (A) Absorbance spectra in the amide I′ region; the temperatures of the individual traces range from 2 °C to 85 °C from top to bottom with approximately 10 °C intervals. (B) Difference spectra obtained by subtracting the spectrum at 2 °C from the spectra at higher temperatures.

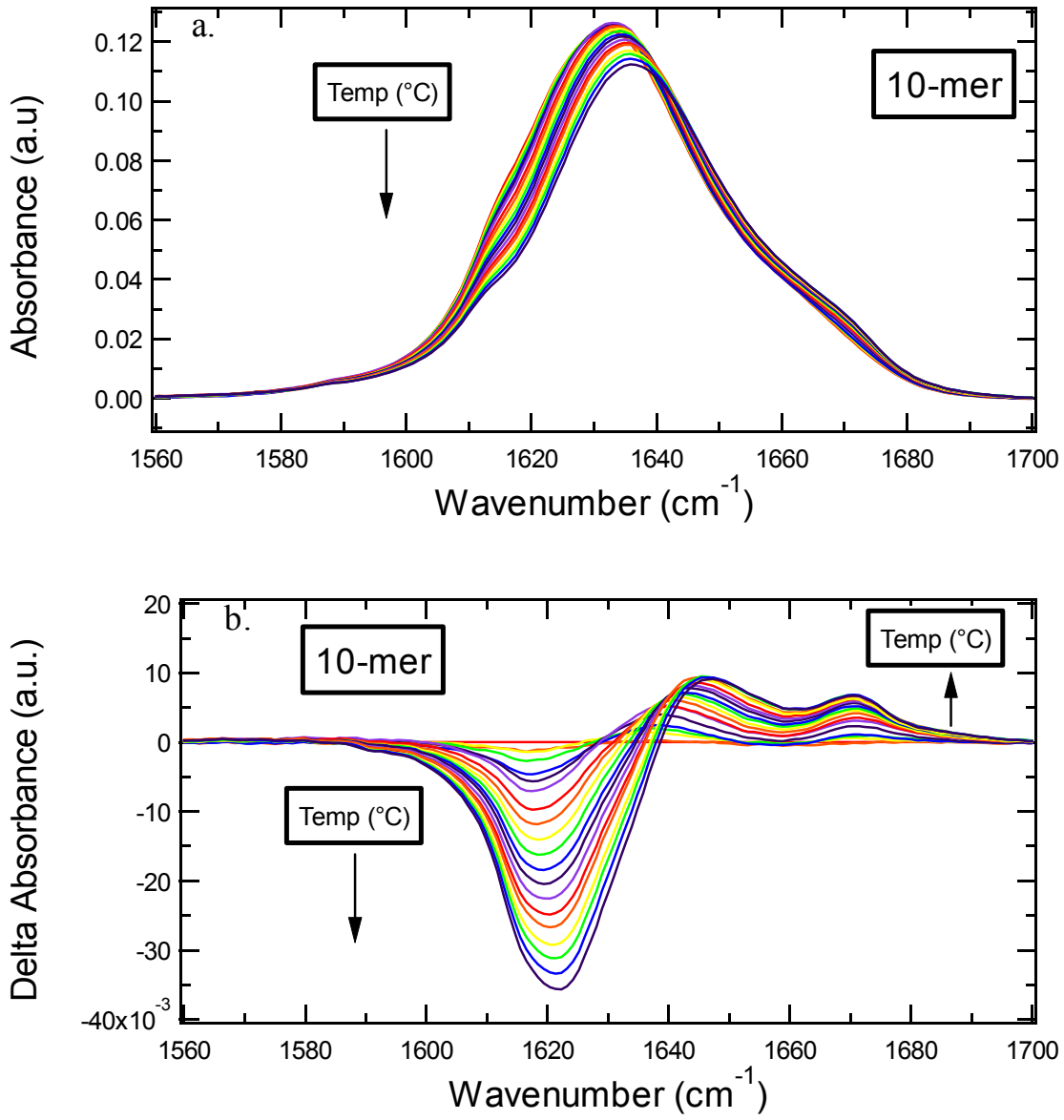

Figure 2 Temperature-dependent FTIR spectra for the 10-mer cyclic peptide, 2.9 mM in D_2O, minimal salt. (A) Absorbance spectra in the amide I′ region; the temperatures of the individual traces range from 1 °C to 85 °C from top to bottom with approximately 10 °C intervals. (B) Difference spectra obtained by subtracting the spectrum at 1°C from the spectra at higher temperatures.

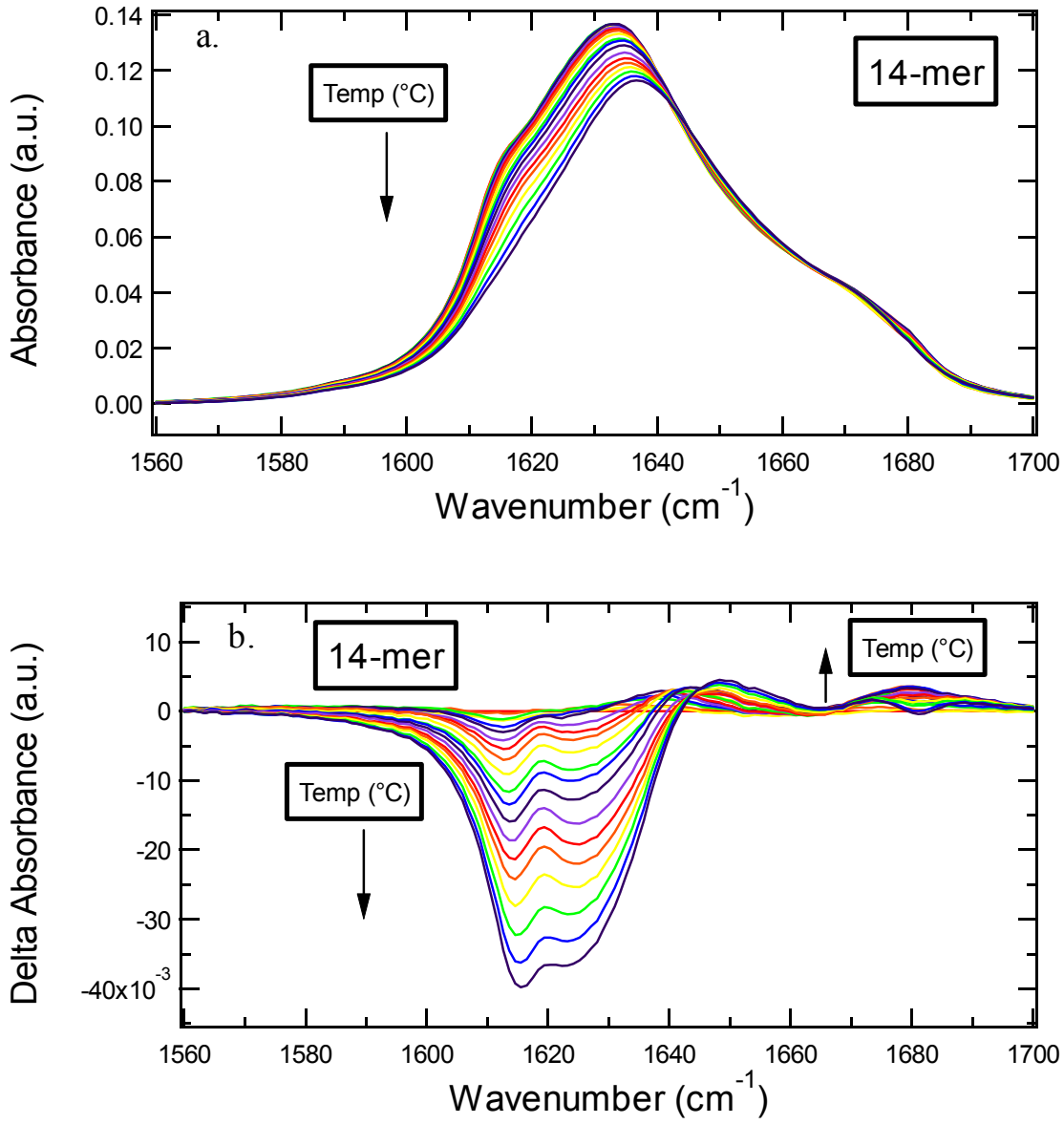

Figure 3 Temperature-dependent FTIR spectra for the 14-mer cyclic peptide, 2.4 mM in D_2O, minimal salt. (A) Absorbance spectra in the amide I′ region; the temperatures of the individual traces range from 2 °C to 83 °C from top to bottom with approximately 10 °C intervals. (B) Difference spectra obtained by subtracting the spectrum at 2 °C from the spectra at higher temperatures.

Table 1 Cyclic peptide amide I′ frequencies,* band areas* and assignments.

	Assignment		
	β-turn	β-sheet(in)	β-sheet(out)
6-mer			
Frequency (cm^{-1})	1623	1637	1657
Area	1.87	1.11	0.11
10-mer			
Frequency (cm^{-1})	1625	1636	1658
Area	1.81	2.47	0.44
14-mer			
Frequency (cm^{-1})	1624	1635	1655
Area	1.90	3.53	1.32

*Derived from deconvolution analysis of FTIR spectrum at 10°C.

supported by the observed ratio of β-sheet/β-turn, which is 0.6, 1.6, and 2.6 for the 6-, 10-, and 14-mer, respectively, compared to the expected values of 0.5, 1.5, and 2.5.

A single broad component centered at 1660 cm^{-1} grows in with increasing temperature. The difference spectra for the 10- and 14-mer show the growth of this broad positive absorbance overlapped with the loss of the narrower high frequency β-sheet band near 1658 cm^{-1} (of negligible intensity in the 6-mer). The frequency and breadth of the 1660 cm^{-1} peak are characteristic of disordered polypeptide structure.[7,8,30] The FTIR spectra therefore provide clear evidence for the loss of folded conformation with increasing temperature.

The FTIR spectra of the 6-mer and 10-mer are concentration independent, and lack the amide I′ signature of aggregation (sharp peaks at 1615 and 1681 cm^{-1} [31,32]), evidence that these peptides are monomers in the concentration range of our experiments (1-4 mM). In contrast, the FTIR spectra of the 14-mer contain an aggregation signature (sharp peaks at 1615 and 1681 cm^{-1} seen in Fig. 3b). The amplitudes of these features are concentration dependent and increase with time, especially at elevated temperatures. In addition, aggregation of the 14-mer peptide at concentrations above 70 μM was reported in a previous study.[20] Despite the presence of aggregated peptide, it is possible to monitor the monomer independently, via its distinct amide I′ bands. Thus it is possible to follow the unfolding of the monomer with increasing temperature, without interference from the aggregated peptide. The very weak temperature dependence of the aggregation peaks suggests that the aggregated form of the peptide is very stable over this temperature range, and does not contribute substantially to the monomer folding/unfolding equilibrium. Finally, the data for the 14-mer reported here were obtained under

conditions where the maximum concentration of aggregated peptide was 11% of the total, estimated from the intensity of the aggregation peaks relative to the monomer peaks.

Melting curves derived from the temperature dependent IR absorbance for the three cyclic peptides are shown in Fig. 4. The solid lines represent fits to a two-state equilibrium model:

$$A = \frac{A_i + A_f * 10^{2(T - Tm) / \Delta T}}{1 + 10^{2(T - Tm) / \Delta T}} \qquad \text{(Eqn. 2)}$$

where A_i and A_f are the extrapolated absorbance values at the two endpoints of the transition, T_m is the transition midpoint, and ΔT represents the overall temperature range of the transition. The T_m and ΔT values from the two-state model fits are listed in Table 2. The melting transition for the 6-mer is so broad that it cannot be uniquely fit using the two-state model over the range of experimentally accessible temperatures. Consequently, the thermodynamic parameters derived for the 6-mer melting transition are not very reliable.

They do reflect the general trend along the series, however, and hence are included for comparative purposes. The transition becomes increasingly sharper (smaller ΔT) as the peptide length increases. This trend reveals the increasing cooperativity along the series. Thermodynamic parameters derived from a van't Hoff analysis are also summarized in Table 2. The free energy of unfolding of these peptides is linear with temperature over an 80 °C temperature range (Figure 5). The thermodynamic parameters reveal that the stability of the peptides increases with increasing peptide length. The substantial enthalpy gain is nearly counterbalanced by the unfavorable entropic cost of folding for both the 10-mer and 14-mer.

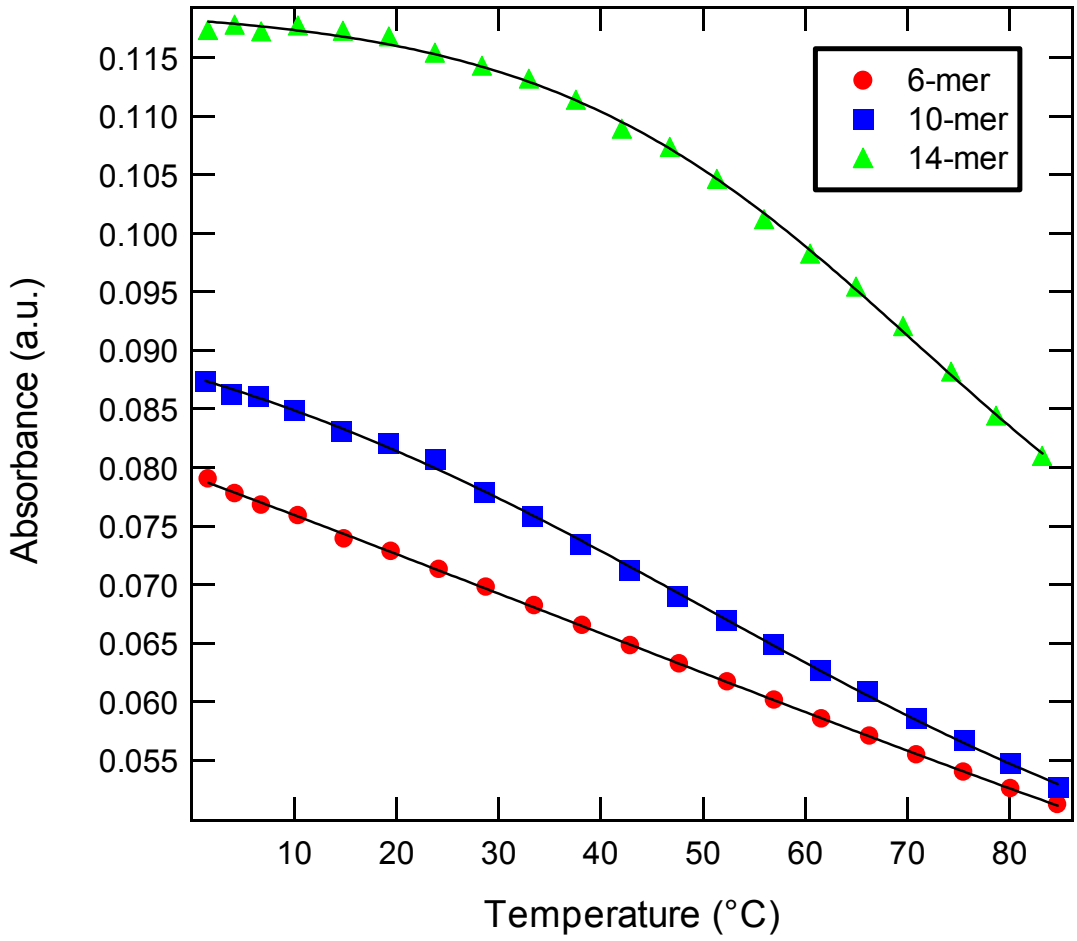

Figure 4 Cyclic Peptide melt curve analyses. FTIR melt curves for the 6-mer (●), 10-mer (■), and 14-mer (▲) cyclic peptides obtained by plotting the change in IR intensity at the peak maximum of the β-turn band at 1621 cm^{-1}, 1619 cm^{-1}, and 1624 cm^{-1}, respectively, versus temperature. The solid lines are fits to a two-state model (Eqn. 2).

Table 2 Cyclic peptide thermodynamic parameters of folding.

	T_m (°C)	ΔT(°C)	ΔH_f (kJ/mol)	ΔS_f (J/mol*K)
6-mer[a]	37	387	-10	-31
10-mer	50.5 ± 0.3[b]	139.4 ± 12.4	-29.1 ± 0.4	-89.8 ± 1.4
14-mer	71.0 ± 2.3	84.1 ± 5.0	-48.3 ± 0.5	-140.4 ± 1.8

[a] The breadth of the transition in this case precludes a unique fit; included for comparative purposes only.

[b] Standard deviations are reported. Thermodynamic parameters are derived from a two-state model and a van't Hoff analysis.

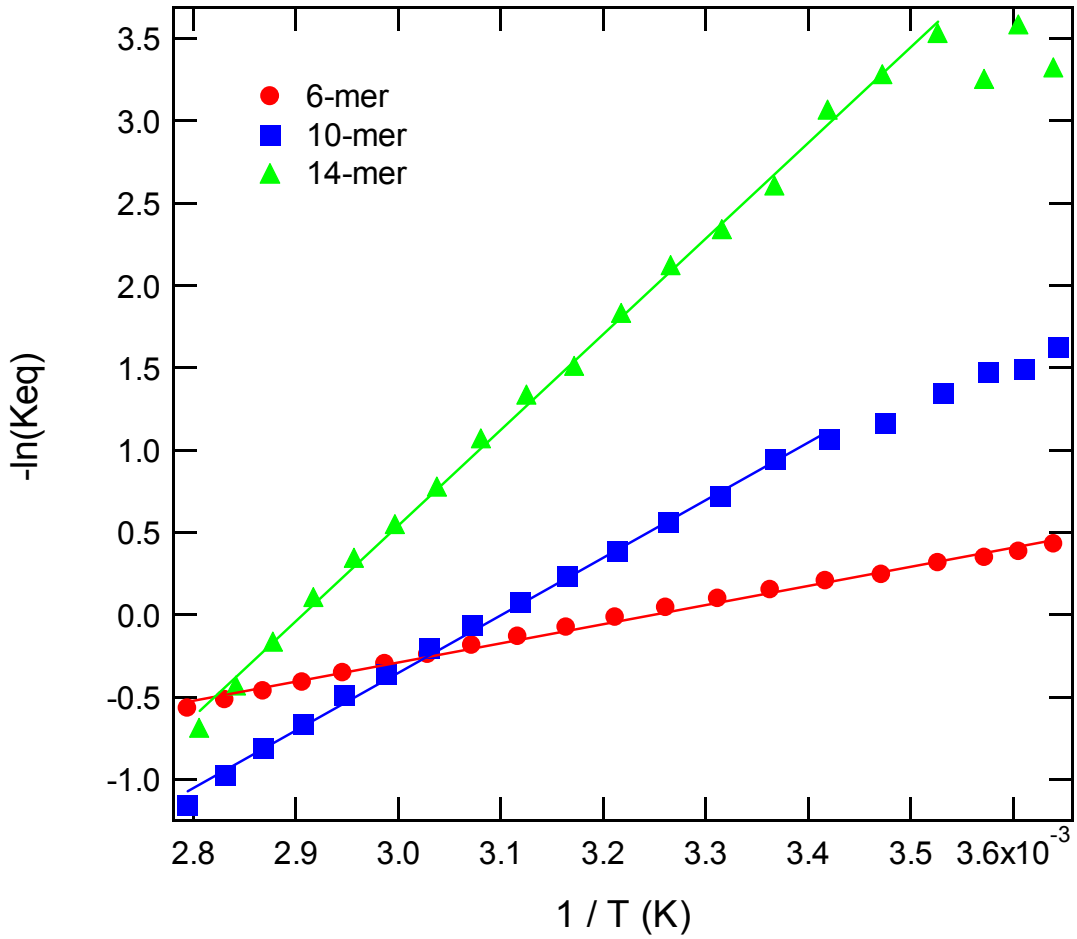

Figure 5 van't Hoff Plots of the 6-, 10-, and 14-mer peptides.

Temperature Jump Relaxation Kinetics. The relaxation kinetics of the F→U transition following a laser induced T-jump were probed using time-resolved infrared spectroscopy in the amide I′ band. Figure 6 displays the relaxation kinetics for the three peptides following a T-jump from 40°C to 51°C. A progressively slower relaxation time is clearly observed along the series for T-jumps to the same final temperature. The data are well fit by a single exponential decay in each case. All of the relaxation kinetics observed for these cyclic peptides are single exponentials, regardless of concentration, starting temperature or magnitude of the T-jump. Furthermore, the equilibrium changes in the FTIR spectra as a function of temperature are best modeled in terms of two states (folded and unfolded structures) as discussed above. We have therefore analyzed the relaxation kinetics using a two-state model, for which the observed relaxation rate is the sum of the folding and unfolding rates, and the equilibrium constant is the ratio of these rates. The relaxation rates for all three peptides (Table 3) are close to the instrument response (response time = 28 ns, $k = 3.6 \times 10^7\ s^{-1}$). Nevertheless, deconvolution of the instrument response from the observed relaxation kinetics is possible because the instrument response is very accurately determined for every relaxation measurement by the reference response. The observed relaxation rates are reproducibly resolved from the measured instrument response using the deconvolution procedure described above. Folding and unfolding rates (Table 3) were extracted from the observed relaxation rates using the equilibrium constant determined from the static FTIR data.

A second set of kinetics experiments with the 10-mer and 14-mer peptides examined the dependence of the relaxation rates on the final temperature following a T-jump. The magnitude of the T-jump was kept constant while varying the initial

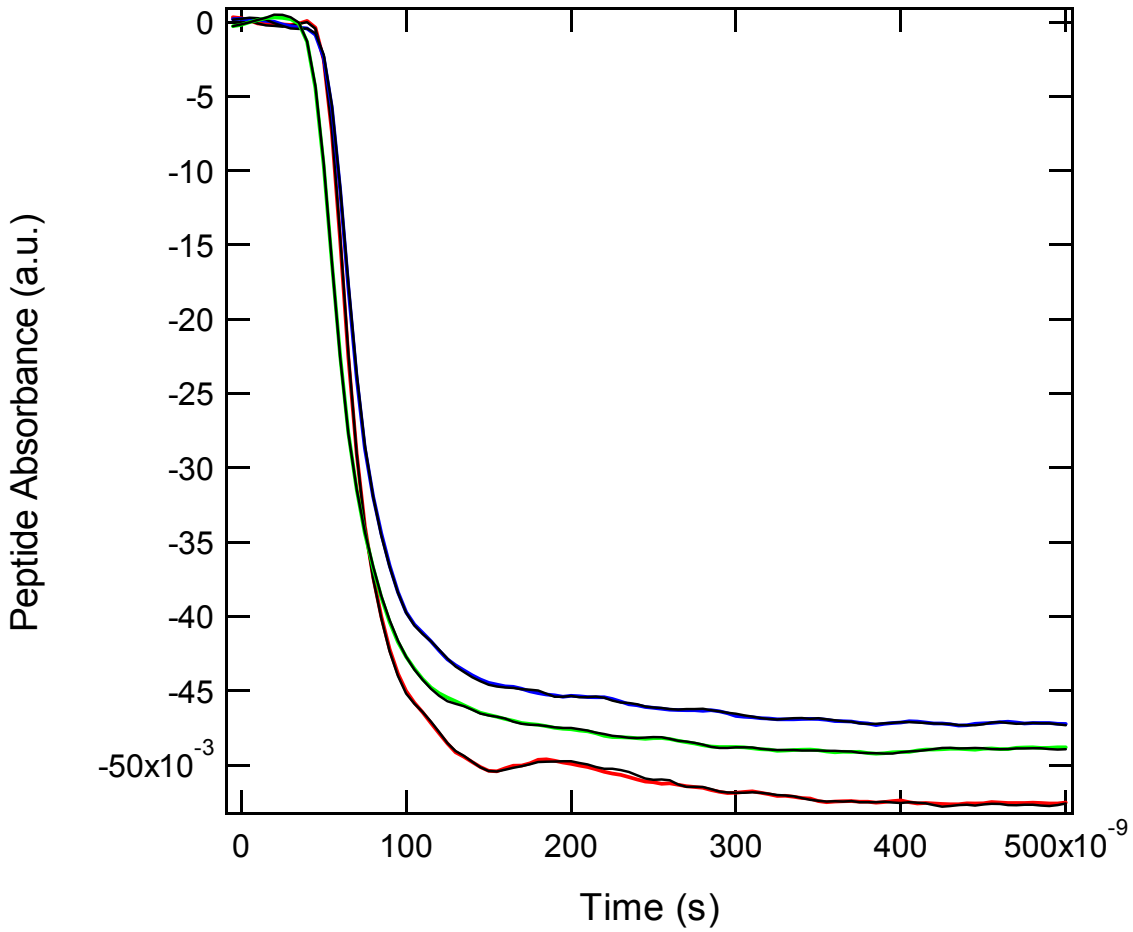

Figure 6 T-jump relaxation kinetics monitored in the amide I′ spectral region (1625 cm^{-1}) following a jump from 40 °C to 51 °C. A single exponential fit is overlaid on each kinetics trace. The amplitudes are normalized to 6-mer amplitude at long time (10 μs) to aid comparison of the relaxation times.

Table 3 Kinetic parameters from T-jump measurements of the cyclic peptides.

	k_{obs} x10^7 (s^{-1})[a,b]	k_f x10^7 (s^{-1})	k_u x10^7 (s^{-1})	$\Delta H_f^{\ddagger}$ (kJ/mol)[c]	$\Delta H_u^{\ddagger}$ (kJ/mol)[c]
6-mer	2.4 ± 0.4*	1.0 ± 0.2	1.4 ± 0.2	-	-
10-mer	1.5 ± 0.2	0.7 ± 0.1	0.7 ± 0.1	-17 ± 2	9 ± 1.0
14-mer	1.1 ± 0.1	0.8 ± 0.1	0.3 ± 0.03	-20 ± 6	23 ± 6

[a]Standard deviations are reported. [b]Relaxation rates measured at T_f = 51 °C. [c]Activation parameters are derived from Arrhenius plots.

temperature to produce a different final temperature within the range of the melting transition. Folding and unfolding rates were determined using the equilibrium constant at the final temperature. An Arrhenius plot (Figure 7) of the folding and unfolding rates versus temperature yielded the activation parameters summarized in Table 3. The limited temperature range of our measurements led to a level of uncertainty in the Arrhenius plots which precluded an accurate determination of $\Delta S^{\ddagger}$.

DISCUSSION

Simple peptide models provide a framework for exploring the fundamental processes of protein folding, including chain collapse and hydrogen bond formation. We have explored these processes in a unique series of cyclic peptides that form β-hairpin structures. Tying the ends of the peptide together dramatically influences the folding behavior compared to linear analogs that form a β-hairpin.

The equilibrium structures and melting behavior of these peptides have been studied using temperature dependent FTIR spectroscopy. At room temperature, all three peptides are strongly folded, having characteristic β-turn and β-sheet components of the amide I′ band (Table 1). These bands are reduced in intensity and a new band corresponding to disordered polypeptide grows in as the temperature is increased. The frequency and band width of the disordered polypeptide band is essentially identical to what we have observed for noncyclic peptides and for proteins.[7,33] The increase in frequency of the amide I′ mode upon unfolding is consistent with loss of strong intramolecular hydrogen bonding.

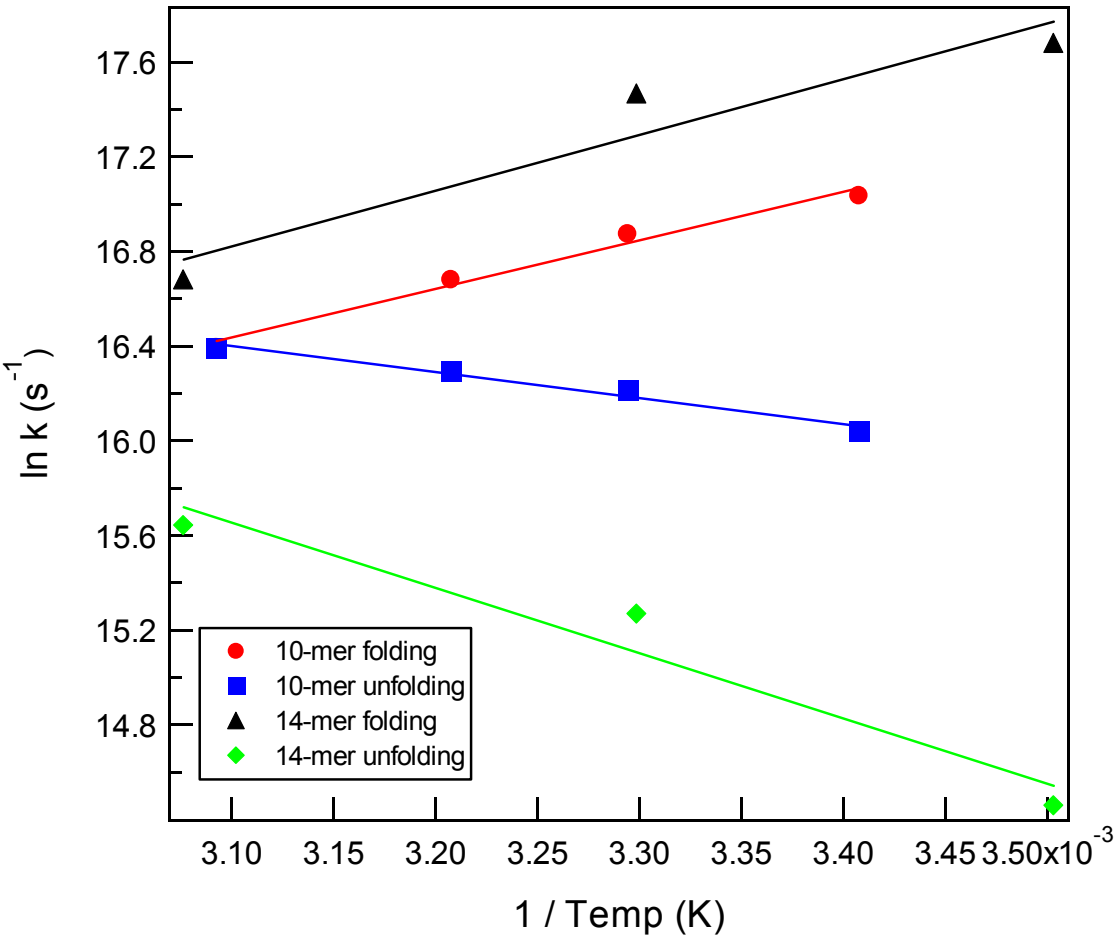

Figure 7 Arrhenius Plot for 10-mer and 14-mer.

A previous study reported minimal temperature-dependent changes for the 10-mer peptide in the far-UV-CD.[20] The interpretation of the 10-mer result was that no significant conformational changes occurred in the temperature range studied between 5 – 85 °C. The problem with this interpretation is that CD spectra of cyclic peptides are not well characterized in general. Furthermore, these cyclic β-hairpin structures have an unusual CD spectrum that more closely resembles that expected for an α-helix than for a β-sheet. Finally, the CD spectrum for unfolded cyclic peptides is not known. Large differences are observed between the CD spectra of β-hairpin forming (6-, 10-, and 14-mer) and non-β-hairpin forming peptides (8-, 12-, and 16-mer).[25] However, it is unlikely that the unfolded structures of the 6-, 10-, and 14-mer resemble the structures of the 8-, 12-, and 16-mer due to the periodicity dependence of accessible conformations. The cyclic systems obviously cannot access extended conformations that would give the characteristic CD spectrum of a disordered polypeptide. Therefore, it is possible that the CD spectrum of the unfolded 10-mer may closely resemble that of the folded state, accounting for the small changes observed in the temperature dependent CD data. In contrast, the IR data offer definitive proof that the intramolecular H-bonding of the β-hairpin structure is lost with increasing temperature. Furthermore, the amide I′ peak of the unfolded state is characteristic of a disordered polypeptide H-bonded to water. Clearly changes in the backbone conformation, in addition to loss of the β-hairpin H-bonding, are necessary to accommodate intermolecular interactions with water molecules.

Further insight into the nature of the thermally induced transition is provided by thermodynamic characterization. A van't Hoff analysis reveals a linear dependence of

the free energy of folding over a very wide temperature range (1–85°C). Both the stability of the folded structure and the cooperativity of the transition (measured by the transition width) increase along the series. The thermodynamic parameters for folding of the 14-mer (Table 2) are remarkably close to those found previously for the GB1 β-hairpin (ΔH = -48.5 kJ mol^{-1}, ΔS=-163 J mol^{-1} K^{-1}). The entropy loss of folding of the cyclic peptide is only slightly smaller than that of the noncyclic peptide. This is somewhat surprising given the restriction in conformational entropy imposed by the cyclization of the structure. This result suggests that the entropy change is dominated by side chain rather than the backbone motions.

The T-jump relaxation kinetics observed for the cyclic β-hairpin structures are remarkably fast. All three cyclic peptides exhibit relaxation rates about two orders of magnitude greater than that observed for the β-hairpin of protein G under similar conditions.[14] This rate acceleration occurs in both the folding and unfolding steps, and appears to be a consequence of cyclization. Obviously the cyclic peptides are constrained to adopt compact structures even in the unfolded state. An estimate of the rate at which a linear polypeptide samples such compact conformations can be obtained from measurements of the rate of contact of the ends of a polypeptide.[34] A flexible peptide of 16 residues is predicted to have an end-to-end contact rate of about 10^7 s^{-1}, which provides an upper limit for the rate at which GB1 samples compact conformations. The folding rate of GB1 is much slower (10^5 s^{-1}), indicating that either the residence times in such conformations are small until specific stabilizing interactions are made, or that collapsed structures are quickly stabilized but with the wrong registry and must rearrange over a barrier to reach the correct fold. In contrast, the structure of the cyclic peptides

precludes the collapse process as a rate-limiting step. In addition, the barrier to rearrangement of the compact, unfolded conformations must be small in this case.

An important feature of the folding rates of this series of cyclic peptides is that they are essentially constant with peptide length (Table 3). The unfolding rate, in contrast, shows a clear decrease along the series. These results suggest that the free energies of the unfolded state and the transition state do not change along the series, but rather the free energy of the folded state is decreased, to yield an increasingly stable folded structure, and a decreasing rate of unfolding. The estimated propagation time (i.e. the rate of making or breaking a single H-bond in a nucleated structure) in a β-hairpin is $1ns^{-1}$ [14]. In addition, the disruption of β-sheet H-bonds in response to a T-jump has been reported to occur on a 1 - 5 ns timescale in ribonuclease A.[35] If the macroscopic folding rate were sensitive to this propagation rate, we would expect it to scale with the number of H bonds in the structure, which it does not. On the other hand, if the rate were dominated by the folding of the turn structure, it should remain constant since all three peptides have the same type II′ β-turns. We conclude that the folding rate is dominated by turn formation.

The temperature dependence of the folding rates yields a negative enthalpy of activation of folding for both the 10-mer and 14-mer. Negative activation enthalpies are unusual in *chemical* reactions because energy is required to partially break covalent bonds in the transition state. Outer-sphere transition metal electron transfer reactions having large negative enthalpies of reaction have been shown to exhibit negative activation enthalpies.[36,37] This observation has been rationalized within Marcus electron transfer theory as due to more energetic states of the activated complex in this case

(highly negative enthalpy of reaction) being less reactive than the less energetic ones.[37] The molecular basis for the observation of negative activation enthalpies in protein folding reactions, however, is less clear. Negative activation enthalpies have been observed in the kinetics of the folding of many proteins, including RnaseA, lysozyme, CI2 and barnase.[38-40] This behavior has been attributed to the difference in heat capacity between the unfolded and transition states ($\Delta C_p^{\ddagger}$), due to the formation of native like hydrophobic interactions in the transition state.[39,40] The free energy of activation of the reaction is temperature dependent, because of the change in heat capacity between the ground (unfolded) state and the transition state. It has a minimum value as a function of temperature, at which the folding rate reaches its maximum, then begins to decrease again. Thus, the folding rate exhibits a parabolic dependence on temperature, yielding an apparent negative activation enthalpy at higher temperatures.

Negative activation energies have also been observed for the folding of small peptide models, although the reason for this is less clear than for the protein examples cited above.[8,14,41] The characteristic parabolic behavior of the Eyring plot produced by $\Delta C_p^{\ddagger}$ is not observed for any of these peptide models, including the cyclic β-hairpin structures in the present study. This is not surprising since the folding of these structures does not involve substantial burial of hydrophobic side chains (with the possible exception of the linear β-hairpin structure studied by Muñoz et al., which also exhibits some curvature in the Arrhenius plot). This implies that the transition state is stabilized by other interactions, such as the formation of intramolecular H-bonds. Our results also imply a substantial entropic barrier to folding, which leads to a positive free energy of activation. The cyclic nature of these peptides restricts the accessible conformations of

the polypeptide to relatively compact structures. Consequently, the entropic barrier must arise from limited peptide backbone degrees of freedom, loss of side chain mobility, and changes in solvation of the transition state.

In summary, the cyclic peptides studied in this work provide new insight into the mechanism of β-hairpin formation. The folding rate of these cyclic peptides is significantly accelerated over the rate of a linear peptide that forms a β-hairpin. The folding of the cyclic peptides involves both formation of the turn and the requisite cross-strand interactions. These events occur on the tens of ns time scale, two orders of magnitude faster than the linear GB1 system. This observation supports the argument that the rate-limiting step in the linear system is either stabilization of compact collapsed structures or rearrangement of collapsed structures over a barrier to achieve the native intrastrand registry. Lastly, a negative value for the activation energy for folding implies a transition state barrier that is primarily entropic in nature, and therefore, corroborates the idea of an organized transition state. While the specific structural origin of these effects is not revealed in these experiments, it is likely due to the presence of stabilizing native cross-strand interactions in the transition state, including hydrogen bonds and hydrophobic contacts.

ACKNOWLEDGMENTS

We thank J.H. Werner for helpful discussions, and C. L. Caramana, J.A. Bailey and C.T. Buscher for technical assistance. This work was supported by a grant from the National Institutes of Health (GM 53640 to RBD).

REFERENCES

(1) Callender, R. H.; Dyer, R. B.; Gilmanshin, R.; Woodruff, W. H. *Annu. Rev. Phys. Chem.* **1998**, *49*, 173-202.

(2) Eaton, W. A.; Munoz, V.; Thompson, P. A.; Henry, E. R.; Hofrichter, J. *Acc. Chem. Res.* **1998**, *31*, 745-753.

(3) Espinosa, J. F.; Gellman, S. H. *Angew. Chem. Int. Ed.* **2000**, *39*, 2330-2333.

(4) Krantz, B. A.; Moran, L. B.; Kentsis, A.; Sosnick, T. R. *Nat. Struct. Biol.* **2000**, *7*, 62-71.

(5) Syud, F. A.; Stanger, H. E.; Gellman, S. H. *The Journal of the American Chemical Society* **2001**, *123*, 8667-8677.

(6) Ramirez-Alvarado, M.; Kortemme, T.; Blanco, F. J.; Serrano, L. *Bioorg. Med. Chem.* **1999**, *7*, 93-103.

(7) Williams, S.; Causgrove, T. P.; Gilmanshin, R.; Fang, K. S.; Callender, R. H.; Woodruff, W. H.; Dyer, R. B. *Biochemistry* **1996**, *35*, 691-697.

(8) Werner, J. H.; Dyer, R. B.; Fesinmeyer, R. M.; Andersen, N. H. *J. Phys. Chem. B* **2002**, *106*, 487-494.

(9) Jäger, M.; Nguyen, H.; Crane, J. C.; Kelly, J. W.; Gruebele, M. *J. Mol. Biol.* **2001**, *311*, 373-393.

(10) Smith, C. K.; Regan, L. *Acc. Chem. Res.* **1997**, *30*, 153-161.

(11) Kortemme, T.; Ramírez-Alvarado, M.; Serrano, L. *Science* **1998**, *281*, 253-256.

(12) Schenck, H. L.; Gellman, S. H. *J. Am. Chem. Soc.* **1998**, *120*, 4869-4870.

(13) Griffiths-Jones, S. R.; Maynard, A. J.; Searle, M. S. *J. Mol. Biol.* **1999**, *292*, 1051-1069.

(14) Munoz, V.; Thompson, P.; Hofrichter, J.; Eaton, W. A. *Nature* **1997**, *390*, 196-199.

(15) Munoz, V.; Henry, E.; Hofrichter, J.; Eaton, W. *Proc. Natl. Acad. Sci. USA* **1998**, *95*, 5872-5879.

(16) Klimov, D. K.; Thirumalai, D. *Proc. Natl. Acad. Sci. USA* **2000**, *97*, 2544-2549.

(17) Pande, V. S.; Rokhsar, D. S. *Proc. Natl. Acad. Sci. USA* **1999**, *96*, 9062-9067.

(18) Dinner, A.; Lazaridis, T.; Karplus, M. *Proc. Natl. Acad. Sci. USA* **1999**, *96*, 9068-9073.

(19) Fernandez-Lopez, S.; Kim, H. S.; Choi, E. C.; Delgado, M.; Granja, J. R.; Khasanov, A.; Kraehenbuehl, K.; Long, G.; Weinberger, D. A.; Wilcoxen, K. M.; Ghadiri, M. R. *Nature* **2001**, *412*, 452-455.

(20) Jelokhani-Niaraki, M.; Prenner, E. J.; Kondejewski, L. H.; Kay, C. M.; McElhaney, R. N.; Hodges, R. S. *J. Peptide Res.* **2001**, *58*, 293-306.

(21) Kondejewski, L. H.; Lee, D. L.; Jelokhani-Niaraki, M.; Farmer, S. W.; Hancock, R. E. W.; Hodges, R. S. *The Journal of Biological Chemistry* **2002**, *277*, 67-74.

(22) McInnes, C.; Kondejewski, L. H.; Hodges, R. S.; Sykes, B. D. *The Journal of Biological Chemistry* **2000**, *275*, 14287-14294.

(23) Jelokhani-Niaraki, M.; Kondejewski, L. H.; Farmer, S. W.; Hancock, R. E. W.; Kay, C. M.; Hodges, R. S. *Biochemistry Journal* **2000**, *349*, 747-755.

(24) Gibbs, A. C.; Bjorndahl, T. C.; Hodges, R. S.; Wishart, D. S. *The Journal of the American Chemical Society* **2002**, *124*, 1203-1213.

(25) Gibbs, A. C.; Kondejewski, L. H.; Gronwald, W.; Nip, A. M.; Hodges, R. S.; Sykes, B. D.; Wishart, D. S. *Nat. Struct. Biol.* **1998**, *5*, 284-288.

(26) Wray, W. O.; Aida, T.; Dyer, R. B. *Appl. Phys. B* **2002**, *74*, 57-66.

(27) Arrondo, J. L. R.; Blanco, F. J.; Serrano, L.; Goni, F. M. *FEBS Lett.* **1996**, *384*, 35-37.

(28) Susi, H.; Byler, D. M. *Methods Enzymol.* **1986**, *130*, 290-311.

(29) Lewis, R. N. A. H.; Prenner, E. J.; Kondejewski, L. H.; Flach, C. R.; Mendelsohn, R.; Hodges, R. S.; McElhaney, R. N. *Biochemistry* **1999**, *38*, 15193-15203.

(30) Dyer, R. B.; Gai, F.; Woodruff, W. H.; Gilmanshin, R.; Callender, R. H. *Acc. Chem. Res.* **1998**, *31*, 709-716.

(31) Colley, C. S.; Griffiths-Jones, S. R.; George, M. W.; Searle, M. S. *Chem. Comm.* **2000**, 593-594.

(32) Zurdo, J.; Guijarro, J. I.; Jimenez, J. L.; Saibil, H. R.; Dobson, C. M. *J. Mol. Biol.* **2001**, *311*, 325-340.

(33) Gilmanshin, R.; Williams, S.; Callender, R. H.; Woodruff, W. H.; Dyer, R. B. *Proc. Natl. Acad. Sci. USA* **1997**, *94*, 3709-3713.

(34) Lapidus, L. J.; Eaton, W. A.; Hofrichter, J. *Proc. Natl. Acad. Sci. USA* **2000**, *97*, 7220-7225.

(35) Phillips, C. M.; Mizutani, Y.; Hochstrasser, R. M. *Proc. Natl. Acad. Sci. USA* **1995**, *92*, 7292-7296.

(36) Cramer, J. L.; Meyer, T. J. *Inorganic Chemistry* **1974**, *13*, 1250-1252.

(37) Marcus, R. A.; Sutin, N. *Inorganic Chemistry* **1975**, *14*, 213-216.

(38) Hagerman, P. J.; Baldwin, R. L. *Biochemistry* **1976**, *15*, 1462-1473.

(39) Chen, B. L.; Baase, W. A.; Schellman, J. A. *Biochemistry* **1989**, *28*, 691-699.

(40) Oliveberg, M.; Tan, Y. J.; Fersht, A. R. *Proc. Natl. Acad. Sci. USA* **1995**, *92*, 8926-8929.

(41) Lednev, I. K.; Karnoup, A. S.; Sparrow, M. C.; Asher, S. A. *J. Am. Chem. Soc.* **1999**, *121*, 8074-8086.

Chapter 4

Linear β-Sheet Peptides

ABSTRACT

Two small β-structure peptide models were studied to determine a characteristic rate of β-sheet formation. The peptides were chosen to test the importance of hydrophobic core formation along the β-sheet and β-turn formation for the folding pathway. H1a is a 16-mer peptide derived from the DNA binding motif of the met repressor dimer. H3 is a *de novo* peptide designed with the hydrophobic core nearer to the β-turn. Equilibrium FTIR measurements and infrared temperature jump spectroscopy were used for studies of folding dynamics. Singular value decomposition (SVD) was required to determine the number of states needed to fit the observed spectral data for peptide folding. H1a was found to follow a three-state model while H3 conforms to a two-state model according to SVD results.

INTRODUCTION

The mechanism of β-sheet formation can be understood by elucidating the nature of nucleation. In the previous chapter it was shown that propagation steps consist of rapid hydrogen bond formation. In the present chapter we investigate the nature of the nucleation event necessary to initiate folding in a β-hairpin. A folded β-sheet peptide consists of a β-hairpin turn and two β-strands that align in a registry that permits both intra- and intermolecular hydrogen bonding. The β-hairpin is the smallest component of an anti-parallel β-sheet.[1-3] Formation of the β-hairpin turn is a crucial step in the folding process of β-sheets and has been implicated as the nucleation event that initiates subsequent folding.[4] β-sheets typically contain a cluster of hydrophobic amino acid residues which associate to form a hydrophobic core. The hydrophobic core plays a significant role in β-sheet formation, and some suggest that it is a possible nucleation site from which hydrogen bonding propagates outward.[5] Thus, there are two possible explanations of the nucleation event: 1. β-turn formation and 2. formation of the hydrophobic core. Experimental evidence that distinguishes between turn formation and hydrophobic collapse is needed in order to resolve the folding mechanism of β-sheet peptides.

Time-resolved studies of peptide folding have been performed for both α-helices and β-sheets. Results from these studies indicate that α-helices have a time constant of 160 ns[6] while the GB1 β-sheet peptide was found to have a lifetime of 3.5 μs.[4] α-Helices fold faster than β-sheets due to the fact that they can form nucleation sites anywhere along the polypeptide backbone, whereas β-sheets are much more restricted in topology.

Nucleation is followed by propagation of hydrogen bonds which allows the peptide to 'zip' into a folded structure. α-Helices display hydrogen bonding between i and i+4 residues, while β-sheets have a larger conformational space to sample in order to obtain the proper hydrogen bond registry. Pre-nucleated cyclic β-sheet peptides were studied using infrared temperature jump spectroscopy and found to 'zip' at times on the order of tens of nanoseconds.[7] Rapid hydrogen bond formation, or zipping, is not a surprising result, however, it definitively precludes hydrogen bond formation as the rate-limiting step for folding. This leads logically to an investigation of nucleation as the rate limiting step in the folding process.

Soluble, monomeric β-hairpin peptide models are ideal test cases to provide insight into the folding mechanism of β-sheet structures within proteins. β-hairpin structures, such as GB1 discussed earlier,[4] have been shown to exist as stable entities when removed from their native protein context.[3] The 16-residue β-hairpin analog of the DNA binding motif of the met repressor dimer known as 'H1' is another example of a small peptide that displays autonomous folding properties in aqueous solution.[3] H1 and one of its analogs, H1a, were studied as part of this research.

Insolubility and aggregation are the primary obstacles that must be overcome in order to study β-structure peptides. Aggregation of peptide samples occurs as a result of the hydrophobic core of monomer peptides associating with hydrophobic regions of other monomers to create a mass of insoluble peptide.[8,9] Decreasing folding times could reduce the likelihood of aggregation since long-lived intermediate states are thought to be precursors of aggregation.[9] Moving the hydrophobic core closer to the β-hairpin turn has been hypothesized to reduce the amount of time required for a peptide to fold.[4] The

effect of placing the hydrophobic core immediately next to the β-hairpin turn was studied in this research using a 12-residue peptide called H3.

We have investigated the relaxation kinetics of two small β-sheet peptides, H1a and H3, in an effort to distinguish the possible nucleation events, β-turn formation and hydrophobic core collapse. Both folding and unfolding processes can be studied using peptides that cold-denature such as H1 and H1a. The condition of cold-denaturation exists when a peptide is unfolded at low temperatures and folds as the temperature is increased. Heat-denaturation is more commonly encountered in protein folding and occurs when a peptide is folded at low temperatures and unfolds upon heating. H1 and H1a both cold-denature when small amounts (< 10%) of hexafluoroisopropanol (HFIP) are added to the aqueous solvent. The addition of an alcohol co-solvent such as HFIP lowers the solvent entropy by ordering solution molecules to create a hydrophobic efffect.[10] H3 was designed such that the hydrophobic core is next to the β-turn region. To our knowledge, the kinetics of such a design which deliberately moves the hydrophobic core next to the β-turn has not been previously characterized. Figure 1 shows the amino acid sequences and hydrophobic core placement for H1a and H3 peptides. Fourier transform infrared (FTIR) and time-resolved infrared spectroscopies were used to obtain dynamical information. The kinetic results of studies of multiple wavenumbers in the amide I′ region were further analyzed using singular value decomposition (SVD) and exponential fitting. SVD was found to be a valuable method for feature reduction to obtain a clear picture of the kinetic processes involved with the folding of H1a and H3 peptides.

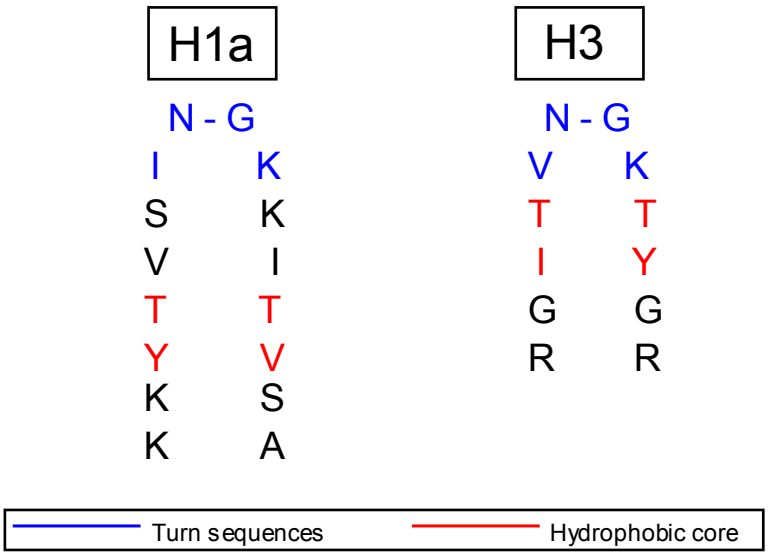

Figure 1 H1a and H3 peptide sequences denoting hydrophobic core position relative to the β-hairpin turn.

MATERIALS AND METHODS

Peptide Samples. All peptide samples used in these studies were synthesized in the laboratory of Prof. Niels H. Andersen at the University of Washington, Seattle. Credit for the original synthesis of H1 belongs to Prof. Mark S. Searle at the University of Nottingham, U.K..[3] H1, H1a, and H3 peptides were received in crystalline form and were lyophilized in D_2O. Samples were dissolved in hexafluoroisopropanol (HFIP) in amounts of 8%, 5% and 21% (volume) for H1, H1a, and H3, respectively. The sequences of the peptides are presented in Scheme 1.

H1: Ac- KKYTVSINGKKITVSI- CO_2

H1a: KKYTVSINGKKITVSA- CO_2

H3: RGITVNGKTYGR

Scheme 1 Peptides used for kinetic studies of β-hairpin formation. The peptides are presented using the single letter code for the amino acids. A representation of the approximate fold for H1a and H3 is shown in Figure 1.

Equilibrium FTIR. Temperature-dependent, static FTIR data were collected on a Bio-Rad FTS-40 instrument using a split sample cell containing both the sample and the reference. The sample cell was translated on a movable stage having a temperature-controlled copper cell mount attached. Single beam intensity was measured for seventeen temperatures in the range of 3.8 - 76.9 °C and computed as absorbance using the –log (sample trace / reference trace).

Kinetic Measurements. Kinetic measurements were made on a pump-probe temperature jump setup.[6] The 1064 nm fundamental of a Nd:YAG laser was passed through a Raman shifter filled with H_2 (g) to generate a 1.91 μm beam (1 Stokes shift) used to pump a weak D_2O overtone in the sample cell. A lead-salt diode probe laser with a range of ~1600-1700 cm^{-1} was tuned to the β-sheet melt region as determined by the FTIR spectra. Data were collected using a Tektronix 7612D programmable digitizer.

Data Analysis. Singular value decomposition (SVD) is a useful technique for visualizing distinctive trends among large volumes of data through the use of feature reduction methods.[11] SVD operates on the basis of the decomposition of a matrix after the following manner:

$$\mathbf{A = UxSxV^T} \qquad \text{(Equation 1)}$$

In this equation, A represents the data matrix, U is comprised of the basis spectra in time, S is the eigenvalue matrix, and V^T is comprised of the basis spectra in wavenumbers. In other words, the components of V^T have the appearance of an infrared absorption difference spectrum and the corresponding components of U are the time courses associated with those spectra. A MatLab program written by Dr. Brandye M. Smith was used to decompose the data matrix A.

The cut-off for determining the number of basis spectra to include in the SVD analysis was based on percent variance. Basis spectra with percent variance in the hundredths decimal place were retained. Three basis spectra were retained for H1a and two basis spectra were kept for the H3 peptide. The basis spectra for time (U) were fit to an exponential function using the principle of Ockam's razor. Ockam's razor reasons that the simplest model should be tested and rejected before using the next more

complicated model. In the case of H3, a single exponential fit was found to be sufficient while a double exponential was required to fit the time basis spectra of H1a. The general equation for an exponential is shown in Equation 2.

$$\mathbf{U}_i = \sum_j \mathbf{c}_{ij} \mathbf{e}^{-k_j t} \qquad \text{(Equation 2)}$$

The following general equation was used to create linear combinations from the coefficients (c) of the fits of the basis spectra for time, the square root of the eigenvalues (s), and V^T, the wavenumber basis spectra:

$$\mathbf{exp}_j = \sum_i \mathbf{c}_{ij} \mathbf{s}_{ii} \mathbf{V}_i^T \qquad \text{(Equation 3)}$$

The results from Equation 3 were plotted as a function of wavenumber to illustrate the reduction of features obtained from the SVD operation.

RESULTS

The time course for the temperature jump infrared probe measurements of the folding process for the H1 peptide is shown in Figure 2. A single exponential fit of the kinetic relaxation of H1 shown in Figure 2 indicates that the observed lifetime is 5.3 ± 0.2 μs. The relative error of one standard deviation is reported for the time constant. Despite signal oscillations at the early times in the trace shown in Figure 2 which may have obscured the visibility of other kinetic phases, a two-state model can be assigned to H1 based on the single-exponential observed kinetics. A two-state model was assigned to H1 earlier based on nuclear magnetic resonance (NMR) and circular dichroism (CD) studies.[3] A microsecond lifetime agrees favorably with the 3.5 μs time constant observed for the fluorescence temperature jump results reported by Muñoz *et al*. for the 16-residue GB1 peptide which also conformed to a two-state model.[4]

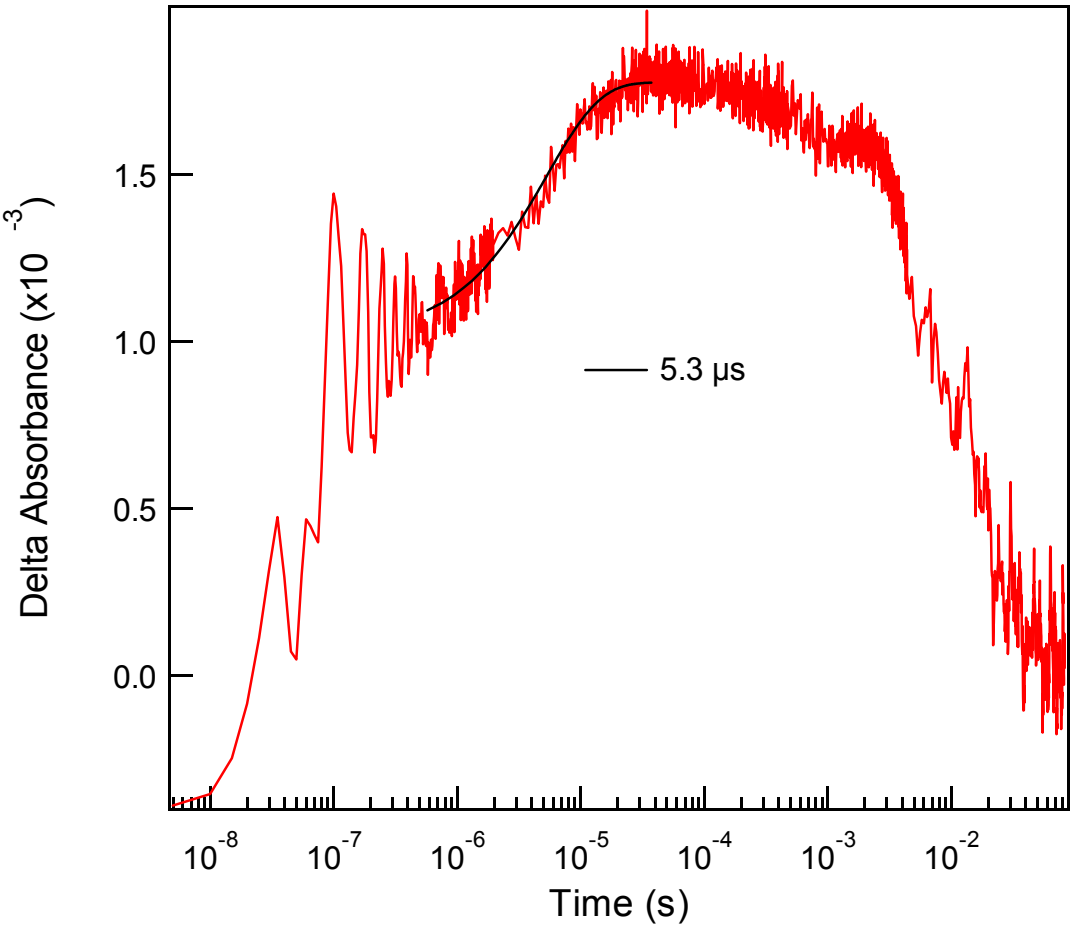

Figure 2 Temperature jump difference spectra of H1 peptide. An infrared temperature jump (T-jump) measurement of 3 mM H1 peptide in 8 % (vol) HFIP from $T_{initial}$ = 2.7 °C to T_{final} = 16.9 °C at 1622.5 cm^{-1}. The difference trace shown here illustrates cold-denaturation in which the peptide is becoming more folded as a result of the T-jump perturbation.

Solution concentrations of up to 3 mM were achieved for H1 in our studies. However, aggregation occurred within a day as temperature jump experiments were performed and became visibly apparent in the sample cell. A cold-denaturing analog of H1 β-hairpin, called H1a, was designed with improved solubility as shown in Scheme 1. H1 and H1a differ by the substitution of the terminal isoleucine residue of H1 for an alanine residue in H1a. H1a is not acetylated which creates a greater electrostatic attraction between the end groups of the peptide. The subtle design changes between H1 and H1a dramatically enhanced the solubility of H1a such that concentrations of 10 mM were achieved without signs of aggregation in the sample cell. The H3 peptide was studied using a sample concentration of 18 mM without evidence of aggregation.

H1a Peptide

Equilibrium FTIR Studies. Static, temperature-dependent spectral changes of folding and unfolding were studied using FTIR spectroscopy. Absorbance data for H1a were collected at temperatures in the range of 4 - 77 °C (Figure 3). The effect of changing temperature is best highlighted by using the 22 °C spectrum as the reference spectrum. The 22 °C spectrum has the highest absorbance of all the spectra obtained in the range from 4 to 77 °C. The data suggest that the highest absorbance in the amide I′ region (prime denotes a deuterated solvent) corresponds to the most folded structure which is found at 22 °C. The amide I′ region of the infrared spectrum has been assigned to a collective normal mode of the polyamide backbone that consists mainly of carbonyl stretching and to a minor extent of N-H in-plane bending.[12] Subtraction of the absorbance spectrum at 22 °C from absorbance spectra of lower temperatures show β-sheet structure increasing as temperatures approach 22 °C at 1626.1 cm^{-1} (Figure 4a).

Difference spectra for temperatures above 22 °C indicated β-sheet disappearance as the temperature increases (Figure 4b). These temperature-dependent changes in β-structure intensity are consistent with cold- and heat-denaturation. Cold denaturation occurs at temperatures below 22 °C, while heat-denaturation occurs as the peptide becomes more unfolded at temperatures above 22 °C. Disordered polypeptide structure is observed in the difference spectra around 1655 cm^{-1}. This feature is mutually exclusive with β-sheet structure and diminishes at temperatures around 22 °C and increases at temperatures both lower and higher than 22 °C. The changes that occur in disordered structure in the amide I′ region have been previously characterized[6,13,14] and further support the FTIR evidence for peptide conformational changes resulting from both cold- and heat-denaturation.

In addition to disordered structure, a temperature-dependent TFA impurity is observed in the 1670 – 1685 cm^{-1} range. TFA is present in the sample as a result of the HPLC purification method used. However, its presence is confined to the high frequency part of the amide I′ region away from the components of interest and does not affect the interpretation of the equilibrium FTIR data in terms of peptide folding.

The melt curve for H1a peptide clearly does not conform to a two-state model as a function of temperature. The effects of cold-denaturation are observed from a melt curve analysis of the β-sheet maximum at 1626.1 cm^{-1} (Figure 5). The addition of 5% volume hexafluoroisopropanol (HFIP) as a co-solvent with D_2O induced cold-denaturation in the H1a peptide. HFIP lowers the solvent entropy by ordering solution molecules based on polarity differences to create a hydrophobic efffect.[10] Cold-denaturation occurs when the unfolded state of a peptide in solution has a larger heat capacity (Cp) than the folded state.[10]

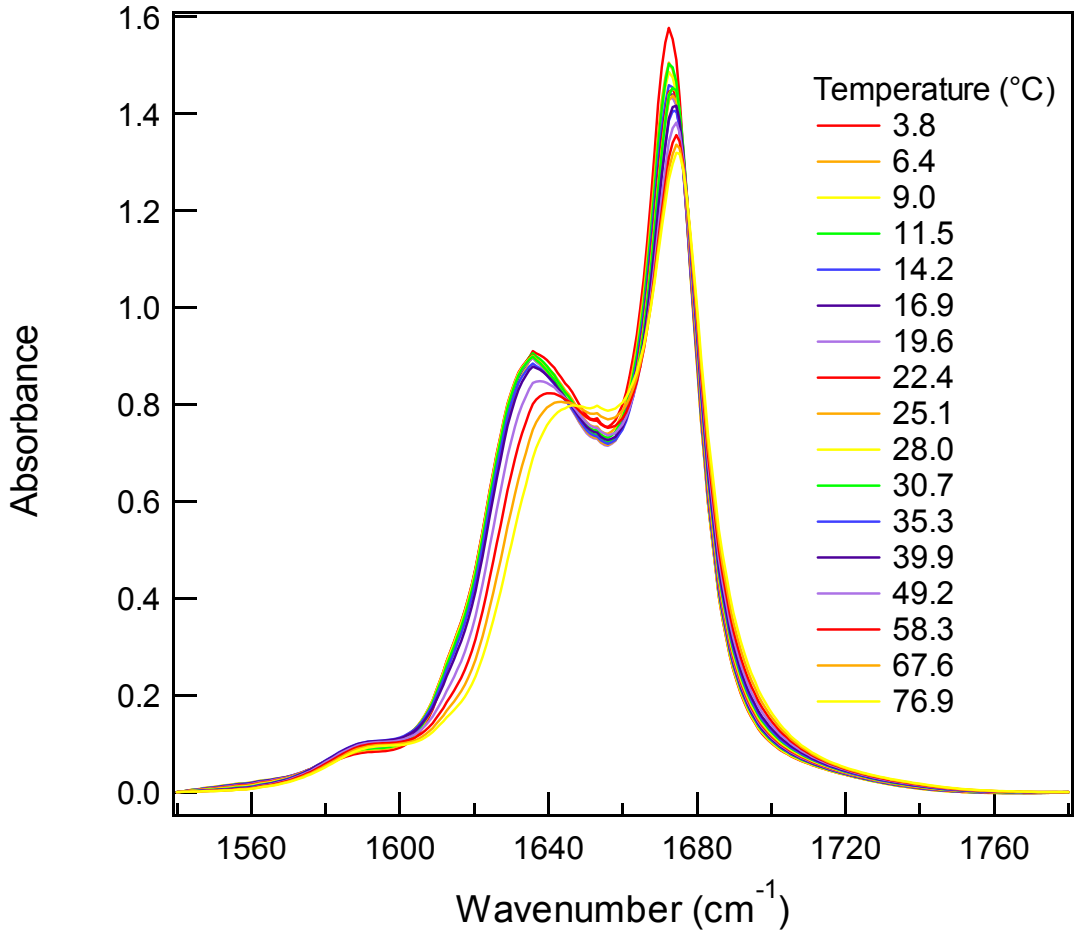

Figure 3 Temperature-dependent FTIR spectra for H1a peptide in 5% (vol) HFIP.

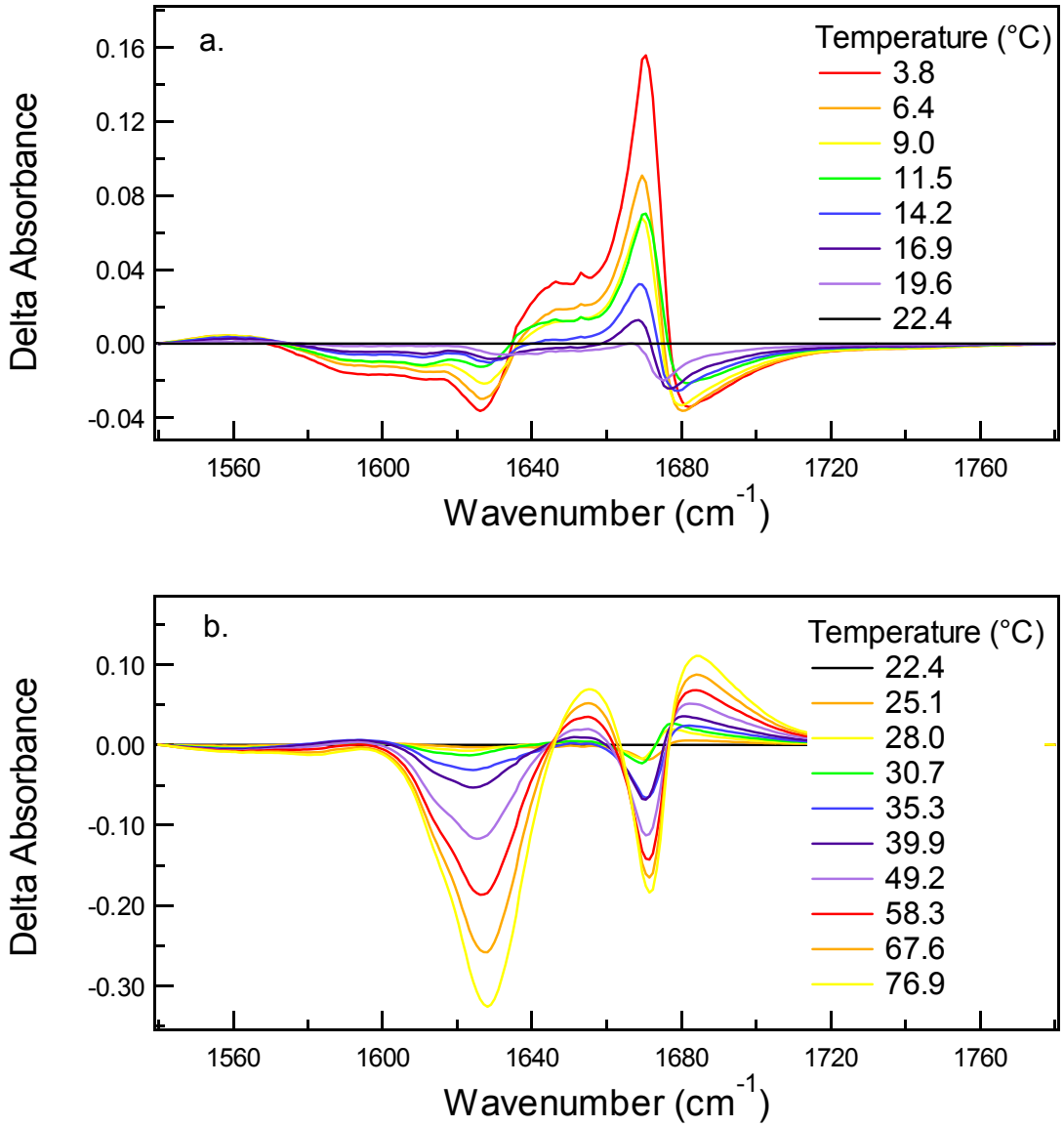

Figure 4 Difference spectra for H1a with 5% (vol) HFIP. β-structure content at 1626.1 cm^{-1} increases from 4 – 20 °C (a) and decreases at that wavenumber between 25 – 77 °C (b).

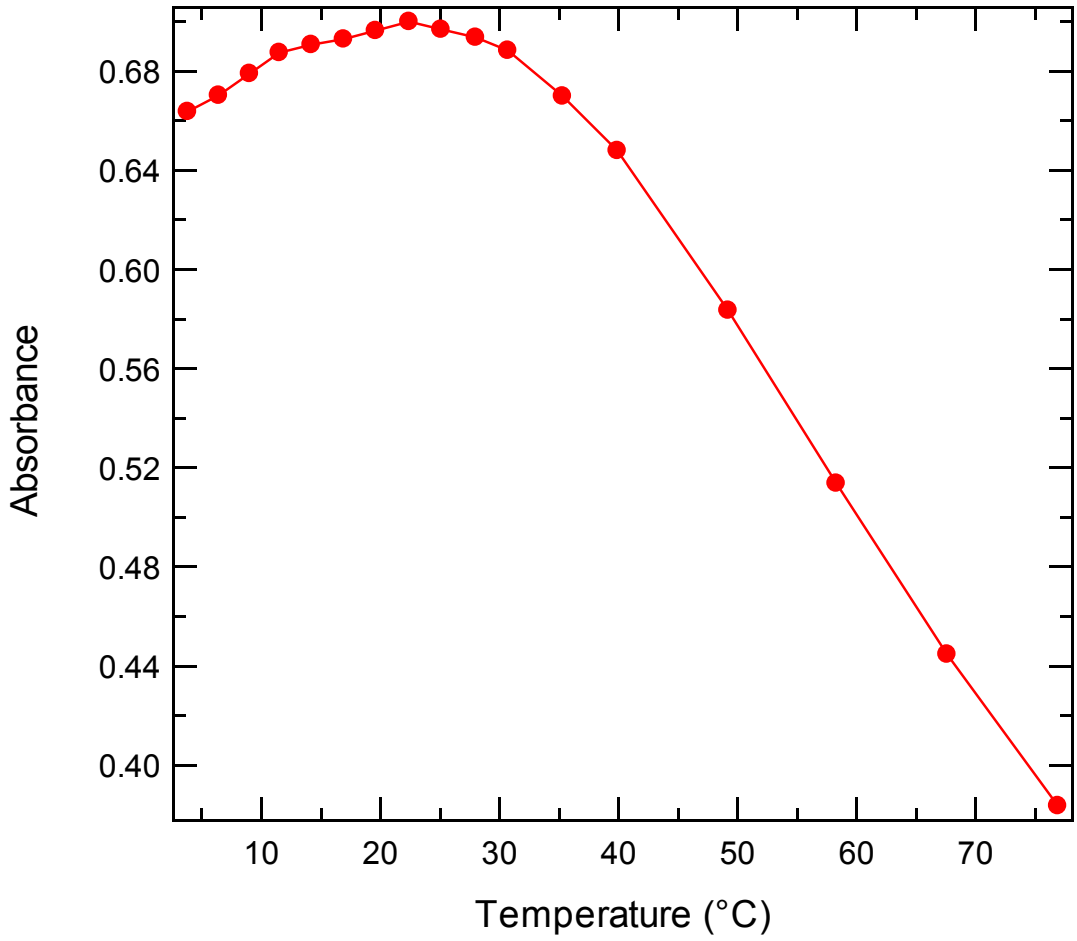

Figure 5 H1a Melt Curve. The absorbance melt curve of H1a peptide in 5% (vol) HFIP at 1626.1 cm^{-1}. Folded peptide is most abundant at 22 °C while unfolded states are found at both lower and higher temperatures.

Temperature Jump Relaxation Kinetics. The relaxation kinetics of transitions between the $U_{cold} \rightarrow F$ and $F \rightarrow U_{heat}$ states of H1a were probed using infrared temperature jump spectroscopy. U_{cold} and U_{heat} correspond to the unfolded peptide in cold- and heat-denatured states, respectively, while F represents the folded state. Observed lifetimes were measured as a function of both temperature (Figure 6) and wavenumber (Figure 7). The transient absorption spectra of the sample were normalized to the reference spectra in order to reduce the kinetics transients due to TFA which are observed at early times. TFA may mask any kinetic events in these spectra on a timescale shorter than 110 ns. A normalization was carried out using the data point at 110 ns for temperature-dependent data and at 300 ns for wavenumber-dependent data. The values for normalization were chosen based on features observed in the individual difference spectra at earlier times, which appeared to be artifacts. These artifacts are attributable to the TFA impurity in the samples.

A kinetic study of the temperature dependence of H1a was performed. Difference spectra consisting of peptide and TFA features were generated from the subtraction of reference spectra from sample spectra. The reference solution contained D_2O and 5% (vol) HFIP. Temperature jumps ranging from 4.3 – 8.2 °C were measured at the various temperatures probed. The difference spectra were fit to a bi-exponential equation. The observed relaxation rates correspond to a fast phase in the 100's of nanoseconds and a slower phase in the microsecond regime. A summary of the rates obtained, as well as the corresponding amplitudes of the phases are shown in Tables 1 and 2. The relative amplitude of the phases depends on temperature. For example, the amplitudes are nearly equal for the data obtained at 14.8 °C (row two in Tables 1 and 2).

Temperature jump studies at various wavenumbers across the amide I′ region were also performed to create a time-resolved infrared spectrum of the folding process of H1a. The T-jumps obtained for these spectra had an average $T_{initial}$ = 12 .4 ± 0.1 °C and T_{final} = 22.7 ± 1.1 °C. The data were fit to a bi-exponential function, and rates similar to those obtained from the temperature-dependent studies were observed. A fast phase of a few 100's of nanoseconds and a slower phase of ~10 μs were observed. However, the variation in results obtained from fitting the data at individual wavenumbers suggested that a global fitting procedure was needed. Singular value decomposition (SVD) is well-suited as a feature reduction method and was chosen to further analyze the wavenumber-dependent kinetic data.

SVD analysis of the kinetic data for the wavenumber dependence measurements indicated the presence of two kinetic phases for H1a peptide. Table 5 shows the eigenvalues associated with each of the eight principle components for the eight wavenumbers studied. SVD analysis for H1a was based upon the first three components since these eigenvalues contained information to the hundredths decimal place in the percent variance. Although the third eigenvalue for component three is shown as zero, this is simply the result of round-off effects. The basis spectra for time (U) and wavenumber (V^T) are shown in Figure 8. The time basis spectra were fit to a double exponential function plus a baseline which had rates of 420 ± 7 ns and 5.8 ± 0.1 μs (Figure 8 top). Errors are reported as the relative error of one standard deviation. Linear combinations of the coefficients (Equation 3) obtained from fits of the time course basis spectra, the singular value matrix, and the wavenumber basis spectra (V^T) were used to generate the component spectra for the individual processes shown in Figure 9. Figure 9

illustrates the fact that components 1 and 2 are slightly shifted relative to each other and appear to represent unique kinetic features of the H1a peptide. The third (green) component spectrum in Figure 9 represents a baseline offset. It is roughly equal to the sum of the components of the two exponential processes, but it has the opposite sign. Subtraction of the first two components in Figure 9 from the third component would generate a relatively flat line which indicates that two components are growing into the spectra over the course of time. A reconstructed data matrix of absorbance changes for H1a peptide as a function of wavenumber variation would conform to Equation 4. This equation illustrates the effect of the time-dependent changes on the two components.

$$\Delta A(1 - e^{-k_1 t} - e^{-k_2 t}) \qquad \text{(Equation 4)}$$

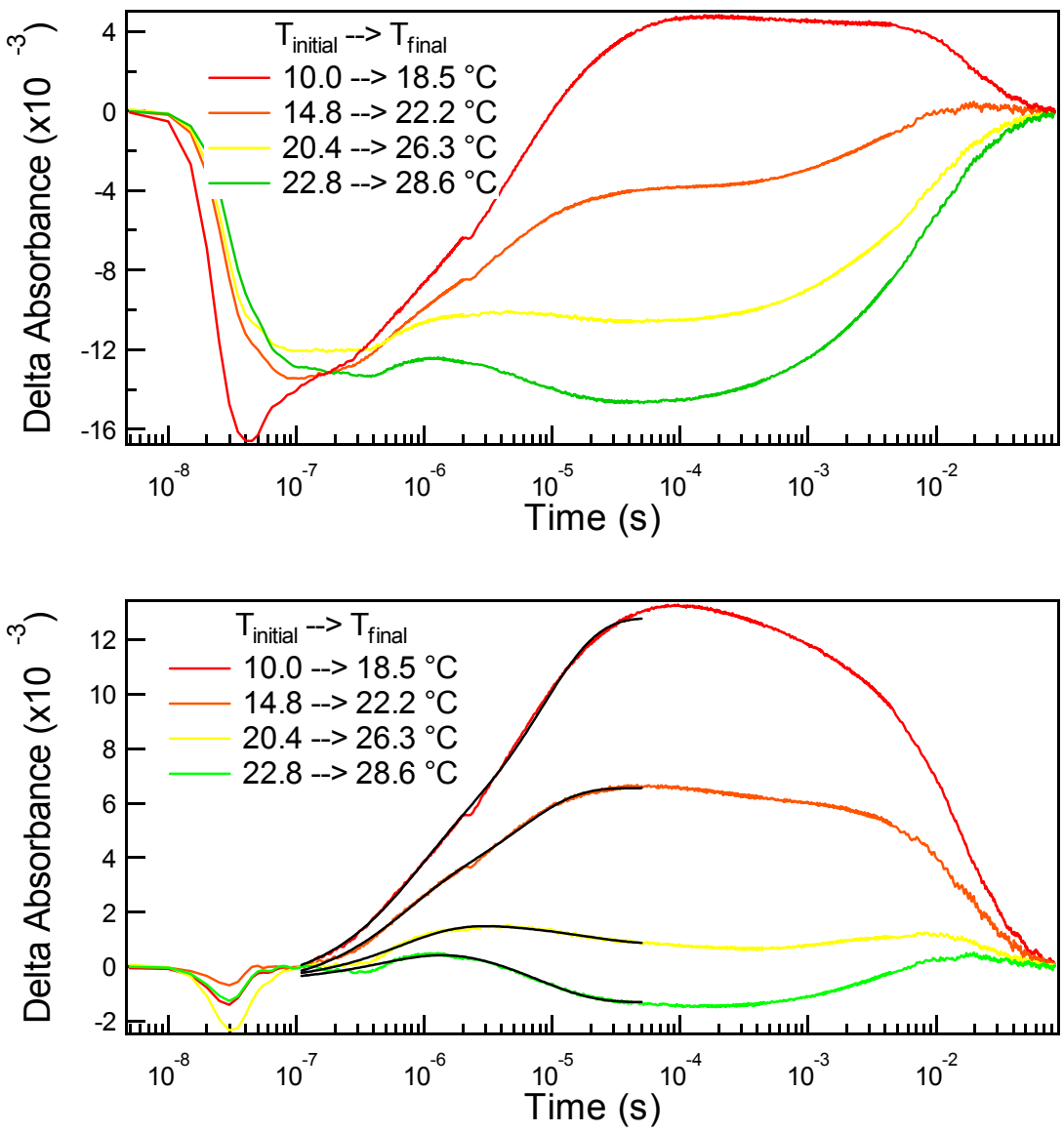

Figure 6 Kinetic relaxation difference spectra for H1a in 5% (vol) HFIP measured as a function of temperature. Laser spikes and the effects of TFA at early times are evident in the uncorrected spectra (top) while spectra normalized to a point at 110 ns better illustrate the effects of changing temperature at 1627.2 cm^{-1}. These traces were fit between the range of 110 ns and 50 μs. Each trace represents an average of two difference spectra.

Table 1 Observed relaxation rates for H1a temperature-dependent T-jumps. Rates and their standard deviations (s.d.) obtained from bi-exponential fits of temperature-dependent difference spectra normalized at 110 ns. Fits were measured between 110 ns and 50 μs.

Tinitial (°C)	Tfinal (°C)	Rate 1	s.d.Rate 1	Rate 2	s.d.Rate 2
10.0	18.5	1.1968E+05	673	1.4672E+06	2.12E+04
14.8	22.2	1.7492E+05	1.34E+03	1.6578E+06	2.14E+04
20.4	26.3	1.4656E+06	2.58E+04	5.6358E+04	3.19E+03
22.8	28.6	1.7251E+06	59500	1.2712E+05	2.04E+03

Table 2 Amplitudes from bi-exponential fits of H1a temperature-dependent T-jumps. Amplitudes of the rates in Table 1 found by using bi-exponential fits of temperature-dependent difference spectra normalized at 110 ns.

Tinitial (°C)	Tfinal (°C)	Amplitude 1	s.d. Amplitude 1	Amplitude 2	s.d. Amplitude 2
10.0	18.5	-0.0088725	2.66E-05	-0.0046724	2.66E-05
14.8	22.2	-0.0039567	1.94E-05	-0.0033855	1.81E-05
20.4	26.3	-0.0021888	1.54E-05	0.00081648	1.32E-05
22.8	28.6	-0.001474	2.03E-05	0.0022187	1.75E-05

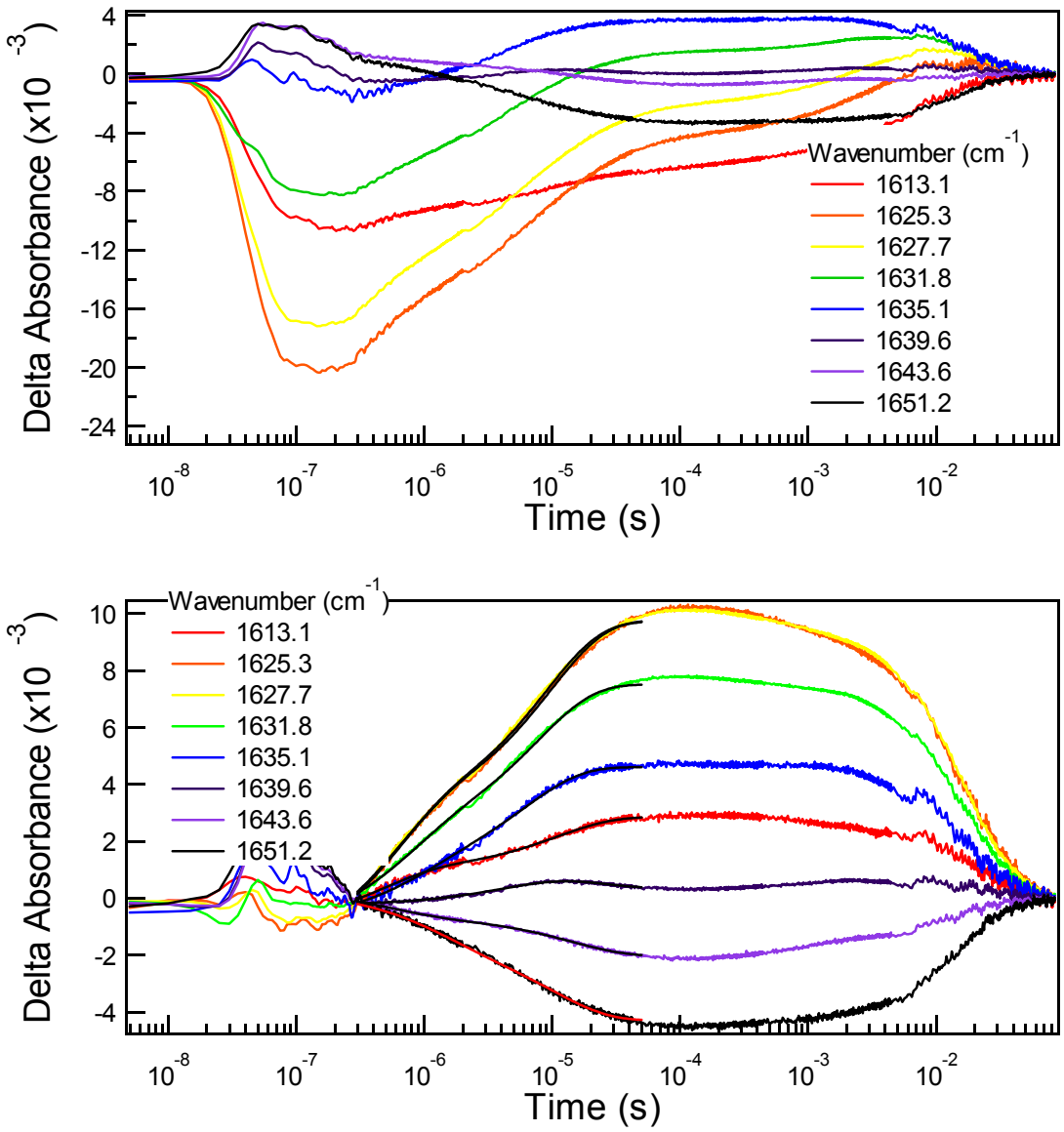

Figure 7 Kinetic relaxation difference spectra for H1a in 5% (vol) HFIP measured as a function of wavenumber. Traces on this graph represent individual spectra and not an average. Difference spectra without normalization (top), and the same spectra normalized to 300 ns (bottom). These traces were fit between the range of 300 ns and 50 μs. The average starting temperature of all traces is 12.4 ± 0.1 °C, while the average final temperature was 22.7 ± 1.1 °C.

Table 3 Observed relaxation rates for H1a wavenumber-dependent T-jumps. Rates and their standard deviations (s.d.) obtained from bi-exponential fits of wavenumber-dependent difference spectra normalized at 300 ns. Fits were measured between 300 ns and 50 μs.

Wavenumber (cm-1)	Rate 1	s.d.Rate 1	Rate 2	s.d.Rate 2
1613.1	9.2191E+04	1.56E+03	2.2457E+06	7.57E+04
1625.3	1.0320E+05	783	1.7776E+06	3.24E+04
1627.7	1.1248E+05	731	1.7847E+06	3.00E+04
1631.8	1.2905E+05	936	1.4855E+06	3.10E+04
1635.1	1.6081E+05	2.58E+03	1.2891E+06	8.01E+04
1639.6	1.8488E+05	1.59E+04	6.7145E+04	1.45E+04
1643.6	7.1259E+04	1.27E+03	1.8177E+06	7.67E+04
1651.2	9.8047E+04	1.88E+03	8.3296E+05	3.02E+04

Table 4 Amplitudes from bi-exponential fits of H1a wavenumber-dependent T-jumps. Amplitudes of the rates in Table 3 found by using bi-exponential fits of wavenumber-dependent difference spectra normalized at 300 ns.

Wavenumber (cm-1)	Amplitude 1	s.d. Amplitude 1	Amplitude 2	s.d. Amplitude 2
1613.1	-0.0018948	1.11E-05	-0.0020442	5.48E-05
1625.3	-0.0067048	2.24E-05	-0.0053251	5.42E-05
1627.7	-0.0067193	2.08E-05	-0.0051316	4.74E-05
1631.8	-0.0053615	2.39E-05	-0.0034026	2.88E-05
1635.1	-0.0038028	4.99E-05	-0.0016984	4.01E-05
1639.6	-0.0014989	0.000263	0.00089619	0.000246
1643.6	0.001405	7.75E-06	0.0009287	2.43E-05
1651.2	0.002824	3.42E-05	0.0017337	3.32E-05

Table 5 Principle component data for H1a peptide.

Principal Component	Eigenvalue	% Variance	% Cumulative Variance
1	**0.1347**	**98.6963**	**98.6963**
2	**0.0018**	**1.2865**	**99.9827**
3	**0.0000**	**0.0121**	**99.9949**
4	0.0000	0.0018	99.9967
5	0.0000	0.0014	99.9981
6	0.0000	0.0010	99.9990
7	0.0000	0.0006	99.9996
8	0.0000	0.0004	100.0000

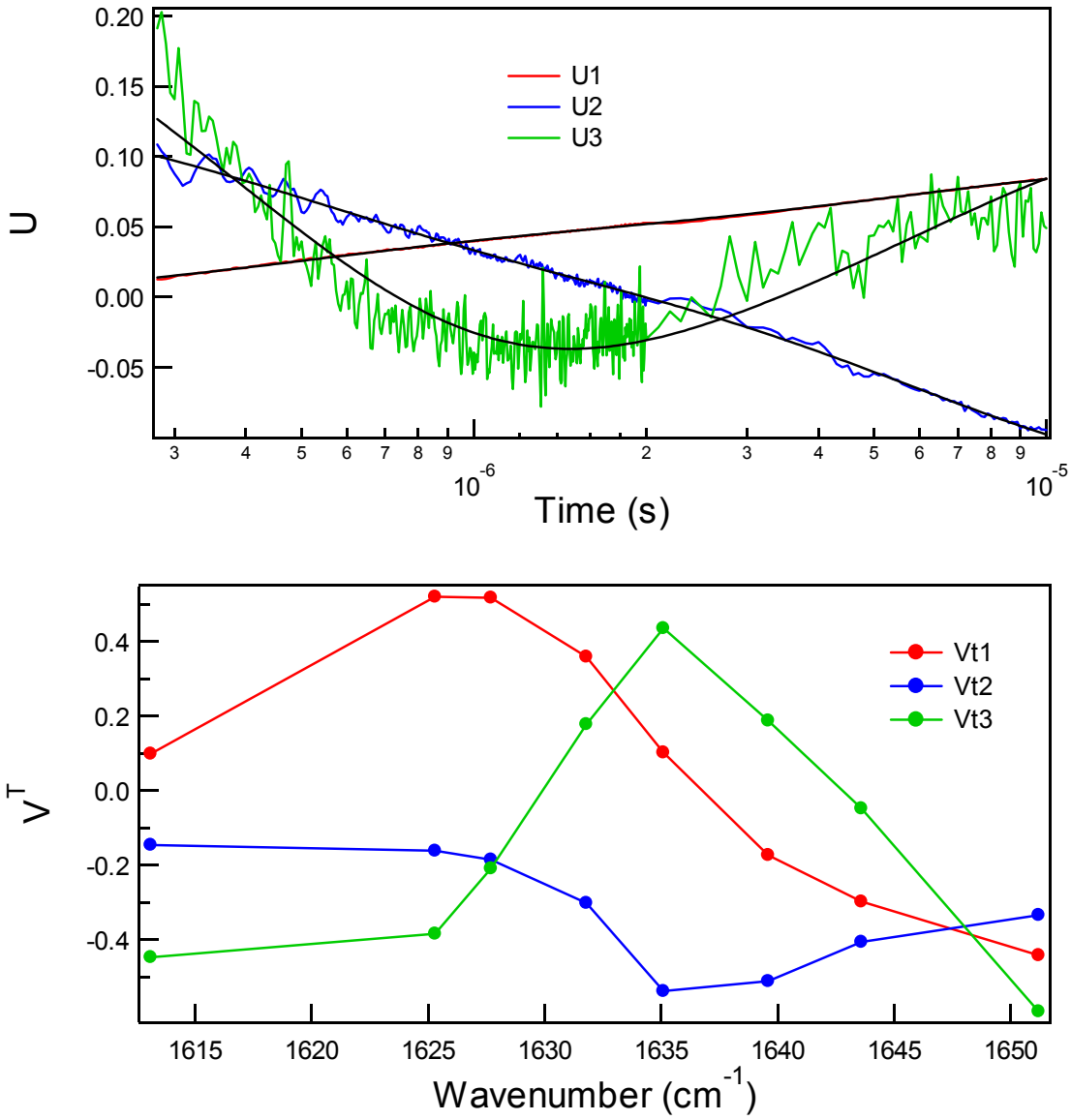

Figure 8 Eigenvectors U (top) and V^T (bottom) used to generate the basis spectra for the H1a peptide. Relative intensities have not been normalized.

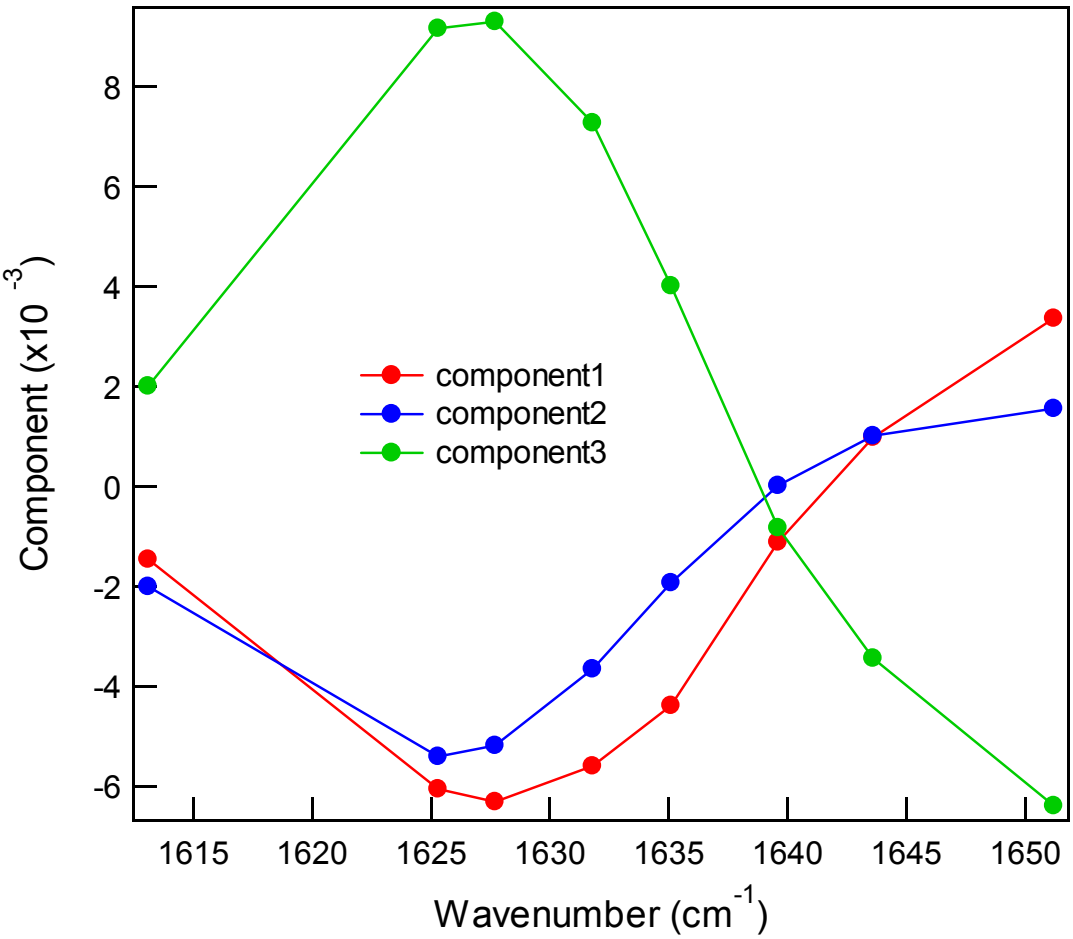

Figure 9 Basis spectra obtained from the decomposition of the SVD matrix. We stress that the model in equation 4 is not imposed on the data, but rather it emerges from the global fitting using the SVD components based on Equation 2. Of course, the components in Figure 9 can be used to reconstruct the original data matrix of ΔA values of wavenumber vs. time.

H3 Peptide

Equilibrium FTIR Studies. Equilibrium FTIR studies suggest that H3 peptide has its most folded conformation at low temperatures. Since a folded structure is not readily achieved for H3 in pure D_2O, 21% (vol) HFIP was added to the D_2O solvent to induce structure. However, the H3 peptide does not cold-denature despite the presence of an alcohol co-solvent such as HFIP. Absorbance and difference spectra for H3 are shown in Figures 10 and 11, respectively. The signature for β-structure is centered around 1636 cm^{-1} in the difference spectra. A temperature-dependent trifluoroacetic acid (TFA) impurity is observed from 1671 – 1687 cm^{-1}. Two small, low frequency peaks appear in the amide II′ region of the difference spectra for H3 which have not been noted in other peptide samples studied in this dissertation. Peaks in the amide II' region have previously been assigned to aromatic or other side chain groups including side chain carbonyl stretches.[15] One hypothesis for the presence of the two low frequency peaks is that they are attributable to the fact that the H3 peptide is neither amidated nor acetylated at the ends of the peptide. This lack of an end group cap could produce low frequency peaks that are the signature of fraying at the end of the peptide's β-strands. The decrease in intensity of the maximum in the β-sheet band at 1635.8 cm^{-1} is shown in Figure 12. The decrease is nearly linear with temperature suggesting that unfolding is not complete even at 80 °C.

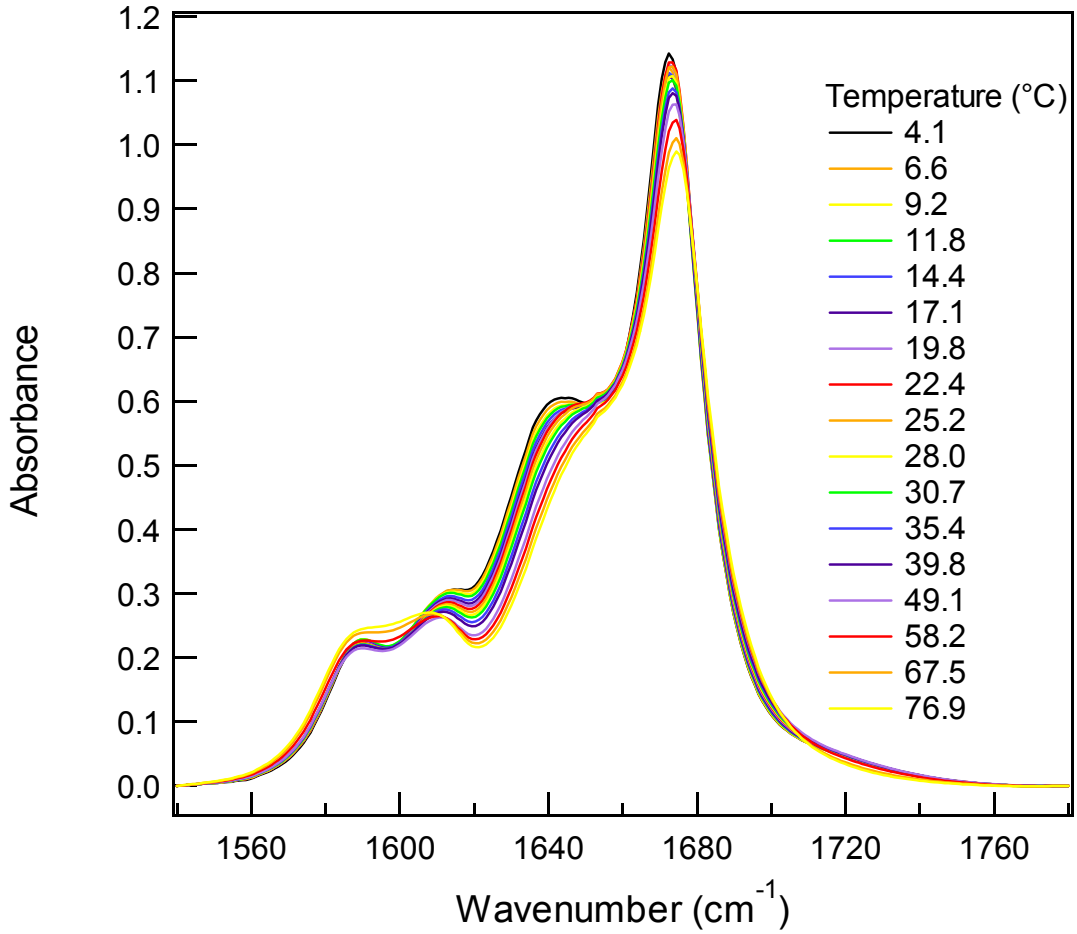

Figure 10 Absorbance spectra of H3 peptide in 21% (vol) HFIP.

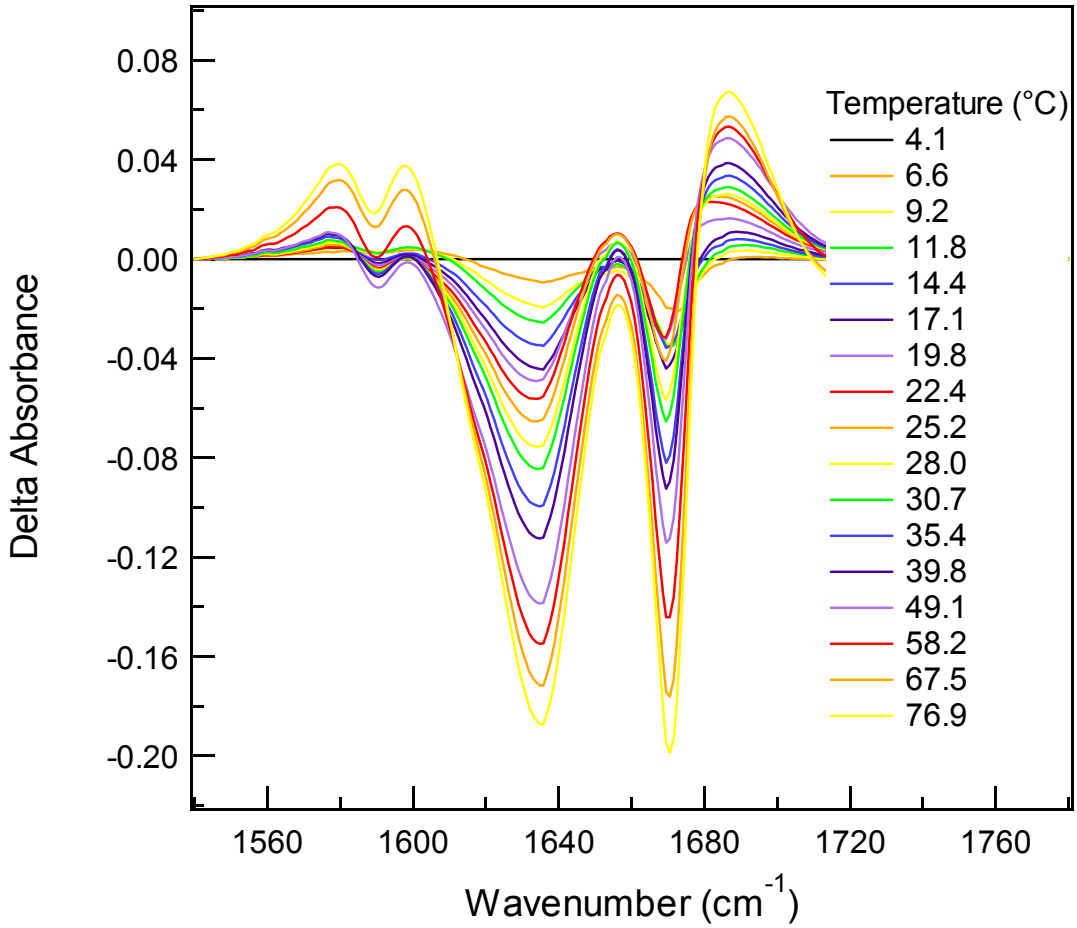

Figure 11 Difference spectra of H3 peptide. β-Structure is decreasing as temperature increases around 1636 cm-1. TFA impurity is observed between 1670 – 1685 cm^{-1}. The peaks around 1580 and 1597 cm^{-1} have not been assigned.

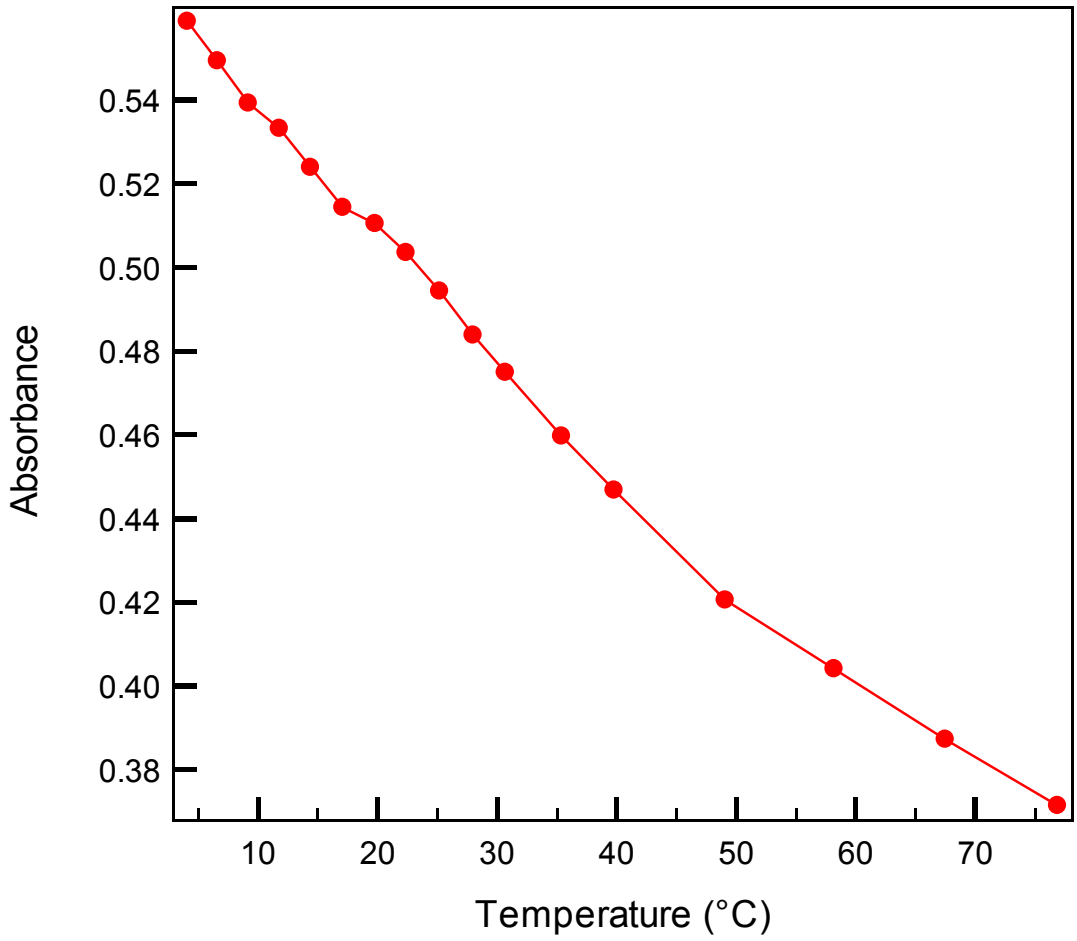

Figure 12 Melt Curve for H3. The melt curve for H3 peptide obtained at 1635.8 cm^{-1} from absorbance spectra.

Temperature Jump Relaxation Kinetics. The relaxation kinetics of the F → U transition were measured for H3 peptide using infrared temperature jump spectroscopy. The observed lifetime for H3 was anticipated to be faster than that of H1a peptide since the position of the hydrophobic core of H3 is one tetrad closer to the β-hairpin turn than in H1a peptide.[4] Kinetic data for H3 peptide were obtained at three temperatures (see Table 6) and eight wavenumbers (see Table 8) and fit to a bi-exponential function. The average T-jump at each of the temperatures was ~3 °C based on calibration curves obtained from T-jump data. The relaxation times obtained from bi-exponential fits of the temperature-dependent data were in the range of 87 ± 2 ns to 808 ± 17 ns where the relative error of one standard deviation is reported (Table 6). The amplitudes of the phases determined by the double exponential fits are listed in Table 7. Sample traces were normalized to reference traces at 110 ns before generating the difference spectra of the kinetic data for different starting temperatures (Figure 13). The purpose of this normalization was to reduce the effects of laser spikes and / or artifacts caused by TFA at early times. Measurements of various wavenumbers in the amide I′ region revealed time constants ranging from several hundreds of nanoseconds to early microsecond regime (Table 8). Amplitudes corresponding to the rates for the various wavenumbers are given in Table 9. A normalization of sample traces to reference traces was applied at 300 ns for the same reasons as given above for the H1a peptide. The effects of this normalization are seen in the difference spectra shown in Figure 14. The average starting temperature for the wavenumber-dependent T-jump measurements was 12.0 ± 0.1 °C, and the average final temperature was 15.8 ± 0.5 °C. Despite the modest T-jump of ~4 °C, these observed rates are slightly faster than those measured for the H1a peptide at similar wavenumbers.

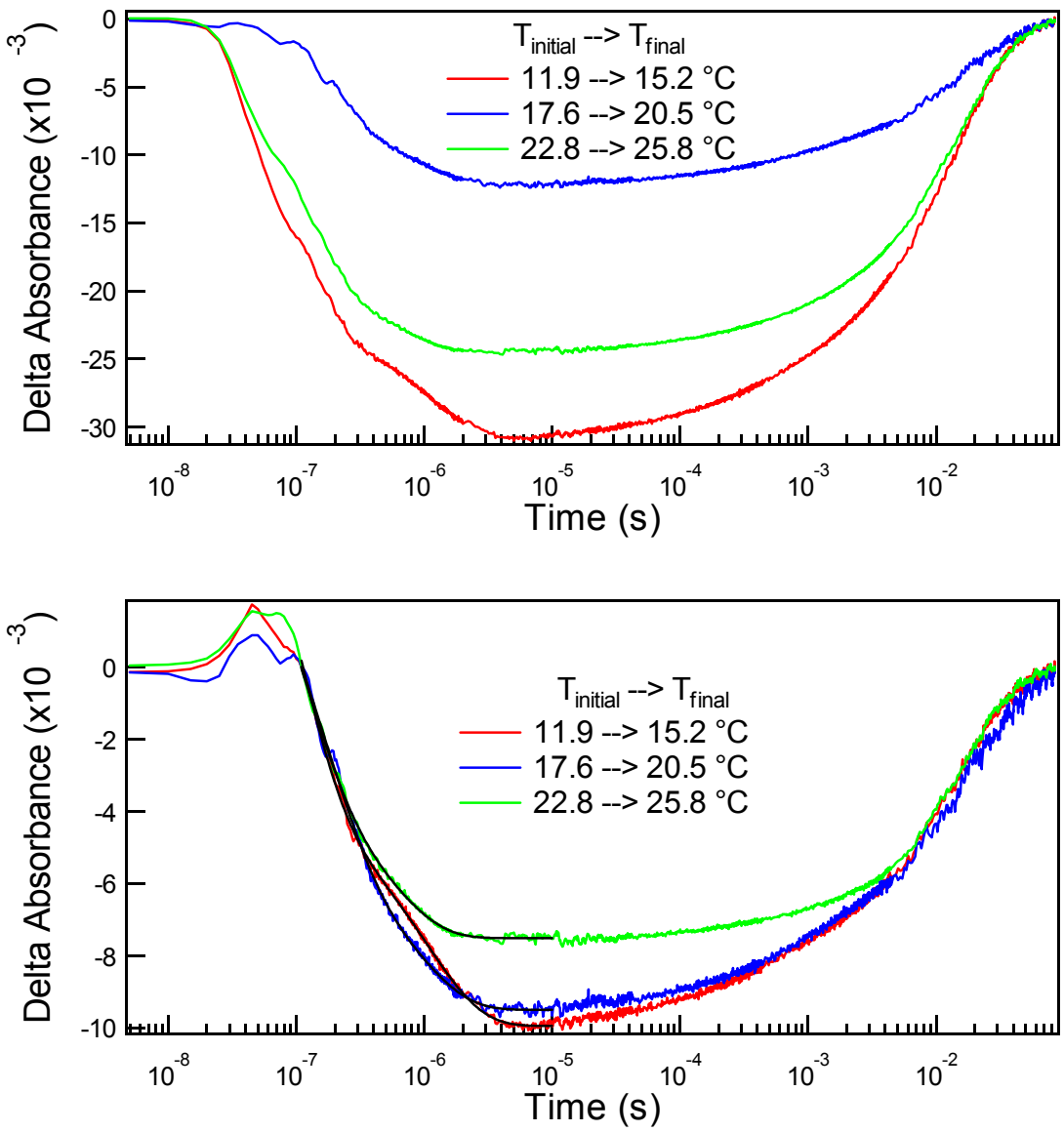

Figure 13 Kinetic relaxation difference spectra for H3 in 21% (vol) HFIP measured as a function of temperature at 1636.2 cm^{-1}. Uncorrected spectra (top) and spectra that were normalized to 110 ns (bottom) are shown here. Double exponential fits were used to fit normalized difference spectra from 300 ns to 10 μs. Each trace represents an average of two or more difference spectra.

Table 6 Observed relaxation rates for H3 temperature-dependent T-jumps. Rates and their standard deviations (s.d.) obtained from bi-exponential fits of temperature-dependent difference spectra normalized at 300 ns. Fits were measured between 110 ns and 10 μs.

Tinitial (°C)	Tfinal (°C)	Rate 1	s.d.Rate 1	Rate 2	s.d.Rate 2
11.9	15.2	9.6086E+05	7.25E+03	1.1500E+07	2.01E+05
17.6	20.5	1.2375E+06	2.66E+04	6.6803E+06	1.69E+05
22.8	25.8	1.9682E+06	2.91E+04	1.0208E+07	2.49E+05

Table 7 Amplitudes from bi-exponential fits of H3 temperature-dependent T-jumps. Amplitudes of the rates in Table 6 found by using bi-exponential fits of temperature-dependent difference spectra normalized at 110 ns.

Tinitial (°C)	Tfinal (°C)	Amplitude 1	s.d. Amplitude 1	Amplitude 2	s.d. Amplitude 2
11.9	15.2	0.0062388	0.0000317	0.016027	0.000394
17.6	20.5	0.0047961	0.000114	0.011101	0.000162
22.8	25.8	0.004682	0.0000875	0.011402	0.000241

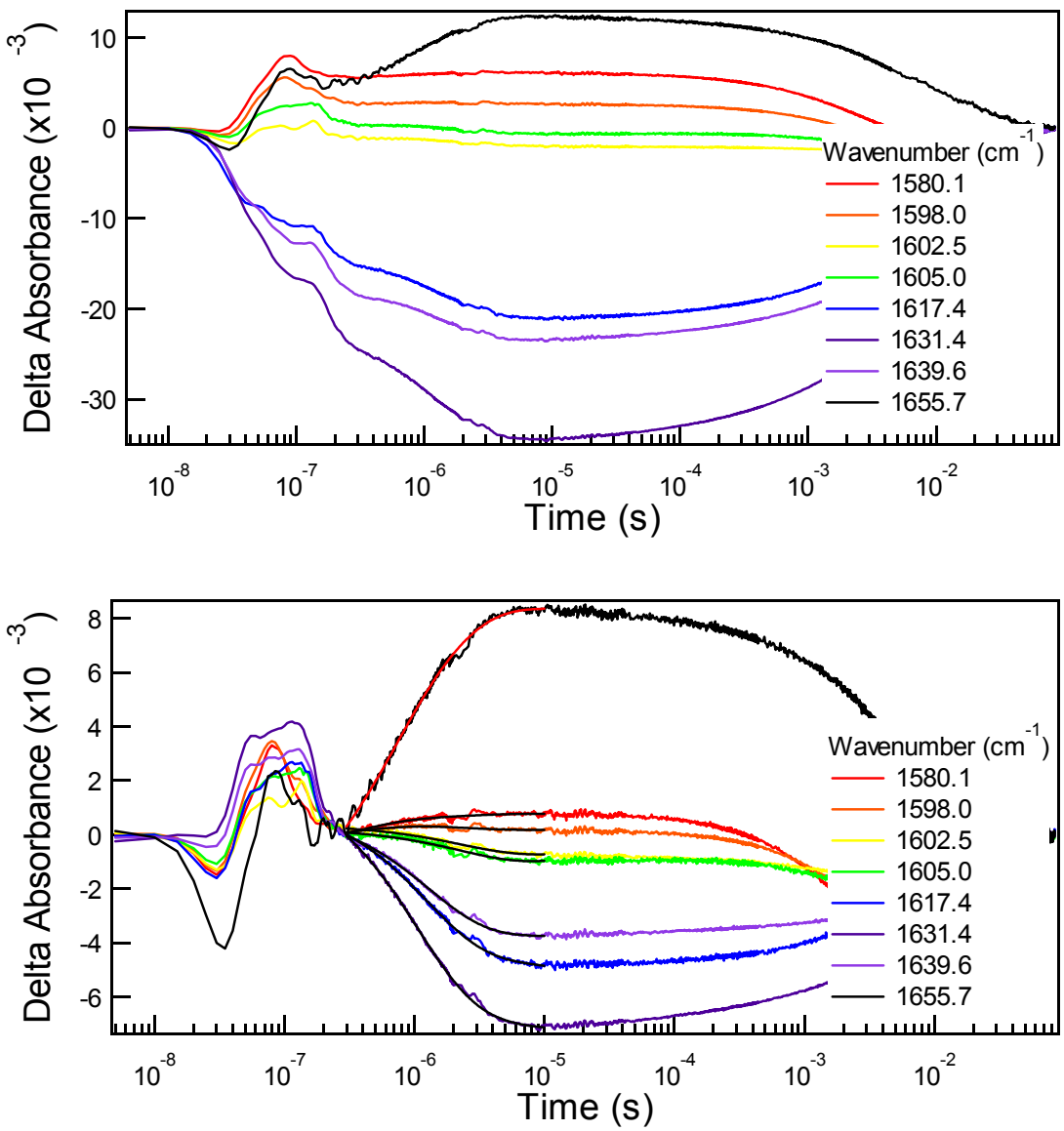

Figure 14 Kinetic relaxation difference spectra for H3 in 21% (vol) HFIP measured as a function of wavenumber. Traces on this graph represent individual spectra and not an average. Difference spectra without normalization (top), and the same spectra with normalization at 300 ns (bottom). These traces were fit between the range of 300 ns and 10 μs. The average starting temperature of all traces is 12.0 ± 0.1 °C, while the average final temperature was 15.8 ± 0.5 °C.

Table 8 Observed relaxation rates for H3 wavenumber-dependent T-jumps. Rates and their standard deviations (s.d.) obtained from bi-exponential fits of wavenumber-dependent difference spectra normalized at 300 ns. Fits were measured between 300 ns and 10 μs.

Wavenumber (cm-1)	Rate 1	s.d.Rate 1	Rate 2	s.d.Rate 2
1580.1	5.0810E+05	2.01E+05	3.1693E+06	5.21E+05
1598.0	5.6946E+05	2.29E+05	2.6616E+06	6.59E+05
1602.5	5.5444E+04	1.41E+06	4.0808E+05	2.33E+05
1605.0	1.6110E+05	1.26E+06	3.4758E+05	5.97E+05
1617.4	1.5431E+05	1.76E+05	8.3366E+05	4.09E+04
1631.4	3.3009E+05	9.47E+04	1.0087E+06	3.89E+04
1639.6	1.8606E+05	1.07E+06	7.7703E+05	4.97E+04
1655.7	6.7358E+05	5.19E+04	2.0016E+06	2.04E+05

Table 9 Amplitudes from bi-exponential fits of H3 wavenumber-dependent T-jumps. Amplitudes of the rates in Table 8 found by using bi-exponential fits of wavenumber-dependent difference spectra normalized at 300 ns.

Wavenumber (cm-1)	Amplitude 1	s.d. Amplitude 1	Amplitude 2	s.d. Amplitude 2
1580.1	-0.00028946	0.0000845	-0.0012488	0.000115
1598.0	0.00031978	0.000127	-0.0007965	0.0000937
1602.5	-0.00037847	0.00415	0.0012812	0.00138
1605.0	-0.001013	0.0112	0.002075	0.0123
1617.4	0.00071454	0.000137	0.0055546	0.000338
1631.4	0.0014034	0.000468	0.0079422	0.000482
1639.6	0.00012059	0.000296	0.0045737	0.000436
1655.7	-0.0060111	0.000751	-0.005749	0.000655

Although the kinetic data obtained for the H3 peptide were fit to bi-exponential equations, uncertainty was present regarding the appropriate model (i.e. two-state or otherwise) to assign to the data. In order to more clearly distinguish the kinetic processes occurring in the wavenumber-dependent difference spectra, singular value decomposition (SVD) was applied to the data using the same procedure as that applied to the H1a peptide. Two basis spectra were selected based on percent variance present in the hundredths decimal place as shown in Table 10. The basis spectra for the time (U) and wavenumber components are shown in Figure 15. The time-dependent basis spectra, U, fit reasonably well to a single exponential with an observed kinetic rate of 1.2 ± 0.0 μs (Figure 15, top). The relative error of one standard deviation is reported. This suggests that the H3 peptide conforms to a two-state model. The linear combinations used to create the component spectra in Figure 16 provide further evidence that a two-state model is the correct assignment for this peptide. The linear combinations produce two traces which appear to mirror each other. A subtraction of these two components from each other would produce a relatively flat baseline indicating that the kinetic rate is going from a folded state to an unfoled state which clearly reflects two-state behavior. A simple formula that can be used to reconstruct the data matrix of the difference absorbance as a function of wavenumber vs. time for H3 peptide is shown in Equation 5.

$$-\Delta A(1-e^{-kt}) \qquad \text{(Equation 5)}$$

Equation 5 differs from Equation 4 only in that there is a single rate constant required for a fit to the H3 kinetic data as opposed to the two rate constants needed for the H1a kinetic components.

Table 10 Principle component data for H3 peptide.

Principal Component	Eigenvalue	% Variance	% Cumulative Variance
1	**0.0820**	**98.7878**	**98.7878**
2	**0.0010**	**1.1984**	**99.9862**
3	0.0000	0.0085	99.9947
4	0.0000	0.0019	99.9966
5	0.0000	0.0013	99.9980
6	0.0000	0.0008	99.9987
7	0.0000	0.0007	99.9994
8	0.0000	0.0006	100.0000

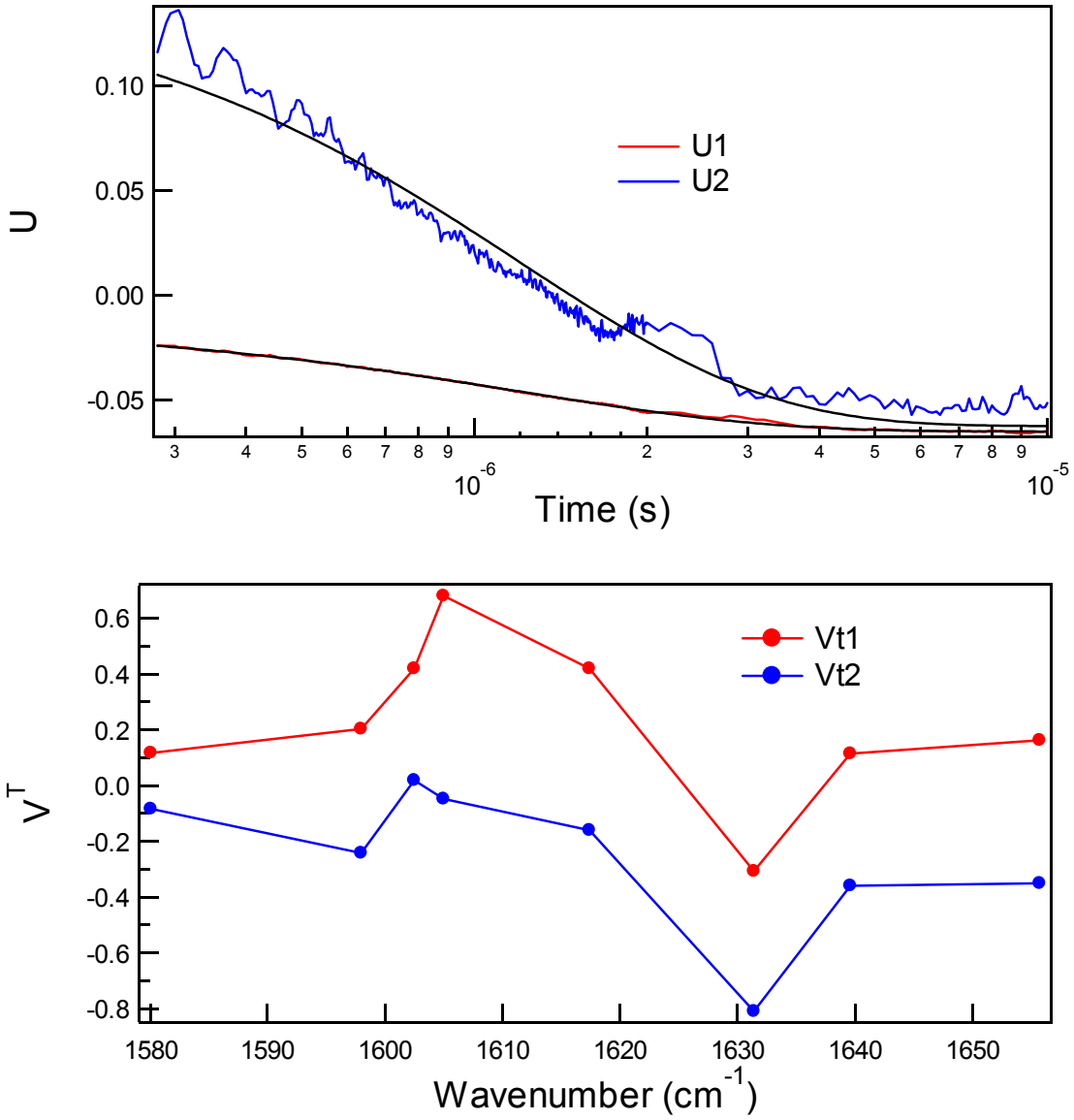

Figure 15 Eigenvectors U (top) and V^T (bottom) used to generate the basis spectra for the H3 peptide. Relative intensities have not been normalized.

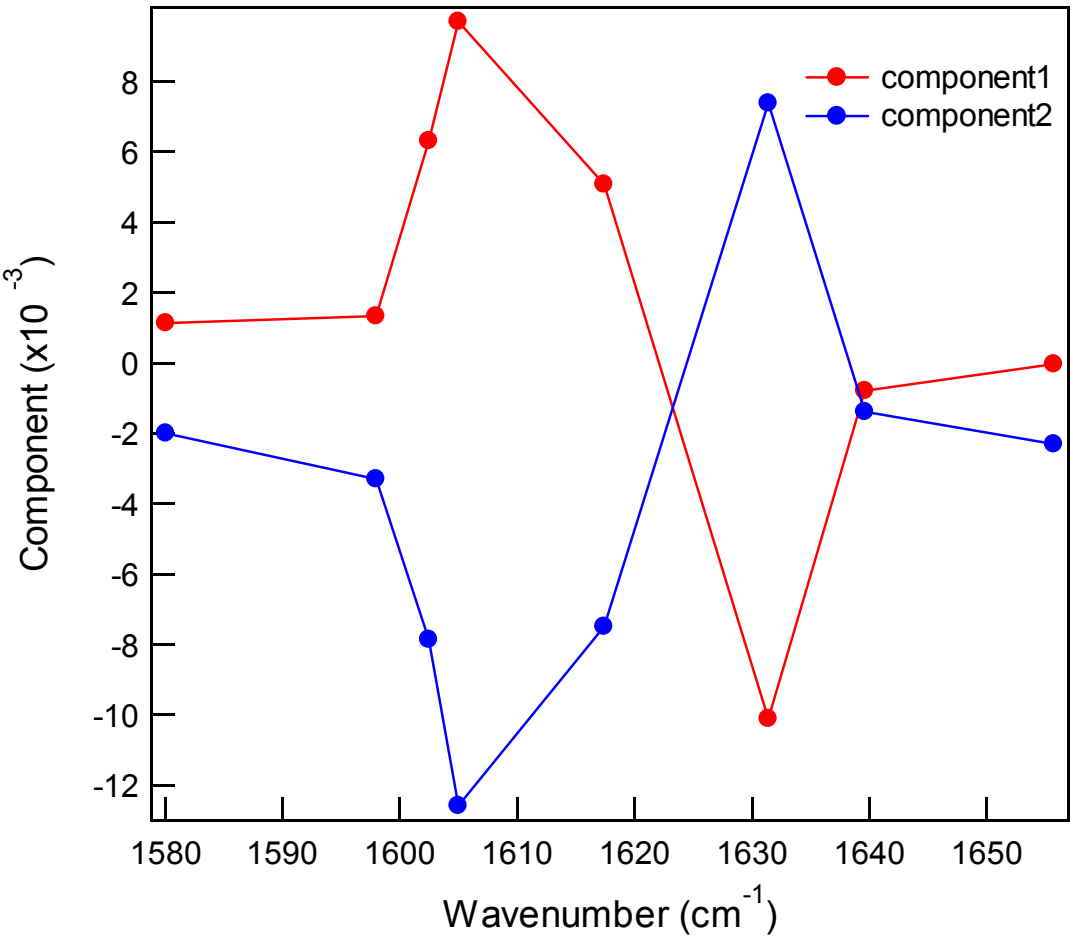

Figure 16 Basis spectra obtained from the decomposition of the SVD matrix.

DISCUSSION

Studies of β-sheet peptide models provide insight into the mechanism of secondary structure formation. In an effort to understand and differentiate the role of β-turn formation and hydrophobic collapse, two β-sheet peptides were studied with time-resolved infrared spectroscopy. H1a peptide both cold- and heat-denatures, while H3 simply heat-denatures. Although previous studies of the H1 peptide suggested two-state behavior,[3] SVD analysis indicates that the H1a peptide does not conform to a two-state model. On the other hand, the shorter peptide, H3 does exhibit two-state behavior based on bi-exponential fits of kinetic data and clearly two-state behavior obtained from SVD analysis.

The SVD analysis indicates that H1a folds in a three-state process. The spectral evidence for an intermediate state can be interpreted in terms of rapid β-turn formation and a slower hydrophobic core collapse of the β-sheet peptide. SVD analysis of H3 indicates a two-state mechanism in which β-turn formation and hydrophobic core formation coincide. Such a mechanism is consistent with the fact that the hydrophobic core is immediately next to the β-turn region in the H3 peptide. The slightly faster relaxation times recorded for the H3 peptide support the prediction that hydrophobic core positions closer to the β-turn region increase folding times.[4]

The folding mechanism can involve nucleation at either the β-turn region or the hydrophobic core. The temperature jump fluorescence experiments performed on the GB1 β-sheet peptide measured only the hydrophobic collapse of fluorescent amino acid residues.[4] This collapse process was observed to occur on a microsecond timescale.[4] Microsecond timescales were also obtained from fits of both H1a and H3 kinetic data.

The microsecond, or slower, phase measured for these peptides is hypothesized to be the result of hydrophobic collapse based on comparisons with the GB1 peptide data.[4] However, a faster transient was observed on the timescale of several hundreds of nanoseconds. Based on the GB1 data,[4] the faster process is assigned to β-turn formation. From the study of cyclic peptides, hydrogen bond propagation was found to occur on a much faster timescale and is not expected to be observed in experiments with non-cyclic peptides.[7] The data on two peptides, H1a and H3 combined with the data on cyclic peptides presented in the previous chapter present a complete hypothesis for the sequence of events in β-sheet formation. First, chain deformations lead to β-turn formation on the timescale of several hundred nanoseconds. Hydrophobic core formation ensues on the timescale of 1 - 10 microseconds. The zipping of hydrogen bonds is rapid and coincides with the hydrophobic core formation.

REFERENCES

(1) Blanco, F.; Ramirez-Alvarado, M.; Serrano, L. *Curr. Opin. Struct. Biol.* **1998**, *8*, 107-111.

(2) Espinosa, J. F.; Munoz, V.; Gellman, S. H. *J. Mol. Biol.* **2001**, *306*, 397-402.

(3) Maynard, A. J.; Sharman, G. J.; Searle, M. S. *J. Am. Chem. Soc.* **1998**, *120*, 1996-2007.

(4) Munoz, V.; Thompson, P.; Hofrichter, J.; Eaton, W. A. *Nature* **1997**, *390*, 196-199.

(5) Dinner, A.; Lazaridis, T.; Karplus, M. *Proc. Natl. Acad. Sci. USA* **1999**, *96*, 9068-9073.

(6) Williams, S.; Causgrove, T. P.; Gilmanshin, R.; Fang, K. S.; Callender, R. H.; Woodruff, W. H.; Dyer, R. B. *Biochemistry* **1996**, *35*, 691-697.

(7) Maness, S. J.; Franzen, S.; Gibbs, A. C.; Causgrove, T. P.; Dyer, R. B. *Biophys. J.* **2003**, *(in press)*.

(8) Kelly, J. W. *Structure* **1997**, *5*, 595-600.

(9) Fink, A. L. *Folding Des.* **1998**, *3*, R9-R23.

(10) Andersen, N. H.; Dyer, R. B.; Fesinmeyer, R. M.; Gai, F.; Liu, Z.; Neidigh, J. W.; Tong, H. *J. Am. Chem. Soc.* **1999**, *121*, 9879-9880.

(11) Massart, D. L.; Vandeginste, B. G. M.; Buydens, L. M. C.; de Jong, S.; Lewi, P. J.; Smeyers-Verbeke, J. *Handbook of Chemometrics and Qualimetrics: Part A*; Elsevier: Amsterdam, 1997; Vol. Part A.

(12) Surewicz, W. K.; Mantsch, H. H. *Biochim. Biophys. Acta* **1988**, *952*, 115-130.

(13) Dyer, R. B.; Gai, F.; Woodruff, W. H.; Gilmanshin, R.; Callender, R. H. *Acc. Chem. Res.* **1998**, *31*, 709-716.

(14) Werner, J. H.; Dyer, R. B.; Fesinmeyer, R. M.; Andersen, N. H. *J. Phys. Chem. B* **2002**, *106*, 487-494.

(15) Susi, H.; Byler, D. M. *Methods Enzymol.* **1986**, *130*, 290-311.

Chapter 5

Computational Modeling

ABSTRACT

Computational methods were applied to models of the cyclic peptides to provide insight into structural properties. Modeling is useful for the interpretation of experimental results because it provides a connection between spectroscopy and structure. Quench dynamics and density functional theory (DFT) were applied to two cyclic peptides to aid in the interpretation of infrared spectroscopic data. For investigations of hydrogen bonding, quench dynamics studies support the idea that families of structures with similar numbers of hydrogen bonds can represent folded, intermediate, and unfolded structures in the folding pathway. DFT calculations performed on the structures obtained by quench dynamics were used to calculate infrared spectra for folded and unfolded structures as well as intermediate or partially folded structures. These results support the hypothesis that temperature-dependent frequency shifts in the amide I′ region are the result of hydrogen bond breaking.

INTRODUCTION

Discerning a correlation between spectroscopic results and protein structure is crucial for the advancement of science in addressing the Protein Folding Problem. Computational methods provide a means for the quantitative analysis of physical changes that occur during a protein folding experiment. The previous two chapters of this dissertation have presented intriguing dynamical information for the folding and unfolding processes of cyclic and non-cyclic β-sheet peptides. However, plausible structural conformations of the peptides are vital for an accurate interpretation of the experimental data. Comprehending the relationship between structure and spectroscopic results is the primary goal of the modeling simulations described in this chapter. In addition to a structure / spectroscopy correlation, two other structural issues are addressed by computational methods. First, modeling simulations have the capacity to identify potential intermediates that exist in experimental data. Although intermediates were not observed experimentally, this does not preclude their existence on the folding pathway. Secondly, computational techniques provide a means of testing the hypothetical effects of changes to an actual peptide structure. In this research, the effect of side-chain contributions in the amide I region was investigated. These calculations provide clues to the overall importance of the polypeptide backbone in governing the collective motions of peptide folding relative to side-chain contributions.

Quench dynamics was the first step used to make the connection between observed time-resolved infrared spectra and structures. Structural properties such as hydrogen bonding can be identified by quench dynamics using a combination of simulated annealing and energy minimization. The result of quench dynamics is a range

of possible peptide conformations that must be analyzed to determine if structures can be grouped into families of similar properties. Quench dynamics can be performed using varied conditions, such as gas or liquid phase, solvent mixtures, and variable temperature. The results reported in this chapter were generated using gas phase dynamics at three different temperatures. Three small, cyclic β-sheet peptides were tested with quench dynamics. The results of these studies showed that indeed there are different families of structures that consist of various hydrogen bonding states.

The second step in the analysis of the observed spectra is the calculation of vibrational spectra using some of the structures generated by quench dynamics as a starting point. Density functional theory (DFT) was used to calculate vibrational frequencies of energy minimized peptide structures. The frequencies found by the DFT calculations are used to generate infrared intensities which can then be compared with experimental results. DFT results are useful for identifying the structural features of the peptide based on shifts in the amide I region.

In an effort to correlate spectroscopy to structure, DFT calculations were performed for the folded, intermediate, and unfolded states of a hexamer peptide. The results of the hexamer study compare the frequency shifts between primarily poly-glycine side-chains and poly-alanine side-chains; two proline residues are included as part of the β-turn region.

In addition to the hexamer peptide, a cyclic decamer peptide was studied using DFT methods to compare the results of a peptide having its original, bulky side-chains attached versus glycine side-chains. Proline is again part of the β-turn region for both

types of side-chain structures. The hypothesis of this study was that the side-chains do not contribute significantly to the amide I infrared frequency.

METHODS

Quench Dynamics. Three cyclic β-sheet peptides were studied using implicit solvent quench dynamics at three temperatures: 400 K, 500 K and 600 K. A btcl script based on a Biosym command language written in collaboration with Melinda Box was used to determine the number of hydrogen bonds present for each peptide at the three temperatures. The amino acid sequences for these peptides are as follows where all tyrosine residues are of D stereochemisty.

6-mer: KdYPKdYP

10-mer: VKLdYPVKLdYP

14-mer: VKLKVdYPLKVKLdYP

These peptides were originally synthesized by Alan Gibbs in the laboratory of Prof. David Wishart at the University of Alberta, Canada.[1]

Discover 3.0 (Accelerys Inc.) was used to create the structural coordinate file (.car) and molecular data file (.mdf) from NMR coordinates which were converted to a Protein Data Bank (.pdb) file for each peptide. The input file (.inp) used for quench dynamics simulations was previously generated from the pdb coordinates. The input file contains the initial coordinates to cycle through the stages of the annealing and energy minimization. Calculations were carried out on the SGI/Cray Origin 2000 at the North Carolina Supercomputer Center (NCSC).

Quench dynamics were performed on the peptide structures in discrete stages. The NMR structure was minimized to the lowest possible energy corresponding to the native, or folded, state of the peptide. After equilibrating at a low temperature, the structure's temperature was jumped to a high temperature (e.g. 400 K, 500 K, or 600 K) for equilibration and molecular dynamics. The goal of the molecular dynamics simulation is to sample the conformational space of the peptide in order to obtain information on the distribution of structures in the ensemble. Prior to molecular dynamics (or production dynamics) an equilibration stage was carried out, in which the structure was allowed to propagate in the force field for 4000 time steps (4 ps). As production dynamics were performed at the higher temperature, 100 'snapshots' of the peptide were taken. These 'snapshots' were captured in history files as the peptide was annealed to the starting temperature. Finally, the 'snapshots' were geometry optimized to their lowest energy conformation and saved as coordinate (.cor) files.

Density Functional Theory Analysis. Calculations of amide I frequencies and infrared spectra were made for the hexamer and decamer peptides. Both peptides were analyzed with all side-chains (except for proline) replaced by glycine. Similarly, the hexamer peptide was studied with poly-alanine side-chains. A DFT calculation for the decamer with its original side-chains was also performed.

DFT calculations were performed using DMol3 software (Accelerys Inc.). Optimized ground state geometries were obtained from the DMol3[2,3] implementation of the generalized gradient approximation (GGA) which was characterized by Perdew and Wang.[4] A convergence criterion of $< 10^{-6}$ a.u. change in the energy and a change of less than 0.003 Bohrs for the atomic length per iteration was used for the geometry

optimization of all molecules. Fixed α-carbon positions were imposed for the geometry optimizations. Subsequent to geometry optimization, atom by atom finite differences were used to generate a hessian matrix. An energy calculation was obtained for the x, y, and z direction of each molecule at each position during the creation of the hessian matrix. From the hessian matrix, vibrational frequencies were obtained after the matrix was diagonalized and mass-weighted to Cartesian coordinates. There were 3N-6 eigenvalues that corresponded to vibrational normal modes. Vibrational frequencies in units of wavenumbers (cm^{-1}) were obtained from these eigenvalues. Infrared intensities were calculated using the finite difference procedure to estimate the difference dipole moment derivative along a given normal mode. InsightII (Accelerys Inc.) software was used for visualization of the results. DFT calculations were performed on the SGI/Cray Origin 2000 and IBM SP supercomputers at NCSC.

RESULTS AND DISCUSSION

Quench Dynamics. Comparisons of the percent probability for hydrogen bond occurrence in three cyclic β-sheet peptides were made for molecular dynamics simulations carried out at 400 K, 500 K, and 600 K. Three temperatures were studied in order to observe the results of increased configurational entropy as higher temperatures permit structures to access more states. Lower temperatures risk the possibility of collecting trapped intermediates in local minima. By comparing three temperatures, one can estimate the temperature required to cross critical energy barriers for complete sampling of the conformational space of the peptide.

The number of possible conformational states of a peptide can be simplified by assuming a two-state model in which the peptide is either completely folded or

completely unfolded. This assumption leads to 2^N possible configurations for each peptide where N is the number of potential hydrogen bonds. There are two, four, and six possible hydrogen bonds for the 6-, 10-, and 14-mer, respectively. A Biosym btcl script sorted structures based on the number of hydrogen-bonded residues using a cut-off distance of 0 – 2.5 Å to define a hydrogen bond. Distances greater than 2.5 Å were considered to be non-hydrogen bonded. Table I and Figure 1 demonstrate the results of the number and percent probability of hydrogen bonds present in the peptides at the three temperatures studied.

Figure 1 illustrates the sampling of hydrogen bonded structures achieved from the quench dynamics studies at three temperatures. The figure suggests that the hexamer peptide preferred a completely unfolded (zero hydrogen bonds) or completely folded (two hydrogen bonds) structure at each temperature studied. Figures 2 and 3 show the quench dynamics structures obtained for the hexamer for a folded and unfolded conformation. These calculated structures provide clear evidence that distinct differences are detectable between folded and unfolded conformations even for small peptides such as the hexamer. Hydrogen bond formation for the 10-mer illustrated how quench dynamics conclusions can vary as a function of temperature. The hydrogen bond sampling results for the 14-mer peptide indicated mixed results, although at 600 K, zero hydrogen bonds had the highest probability. The calculated structures obtained from quench dynamics simulations are significant factors for the interpretation of experimental results of peptide unfolding. The impact of these structures was increased by combining the results of quench dynamics simulations with density functional theory (DFT) calculations.

Table 1 Percent probability of hydrogen bond formation from quench dynamics studies.

6-mer			10-mer			14-mer		
Temp (K)	H-bonds	% Probability	Temp (K)	H-bonds	% Probability	Temp (K)	H-bonds	% Probability
400 K	0	44	400 K	0	0	400 K	0	0
	1	10		1	0		1	0
	2	46		2	19		2	1
				3	29		3	7
500 K	0	40		4	52		4	68
	1	7					5	23
	2	53	500 K	0	18		6	1
				1	4			
600 K	0	56		2	39	500 K	0	0
	1	6		3	35		1	1
	2	38		4	4		2	1
							3	6
			600 K	0	51		4	13
				1	7		5	71
				2	33		6	8
				3	7			
				4	2	600 K	0	28
							1	8
							2	14
							3	18
							4	13
							5	11
							6	8

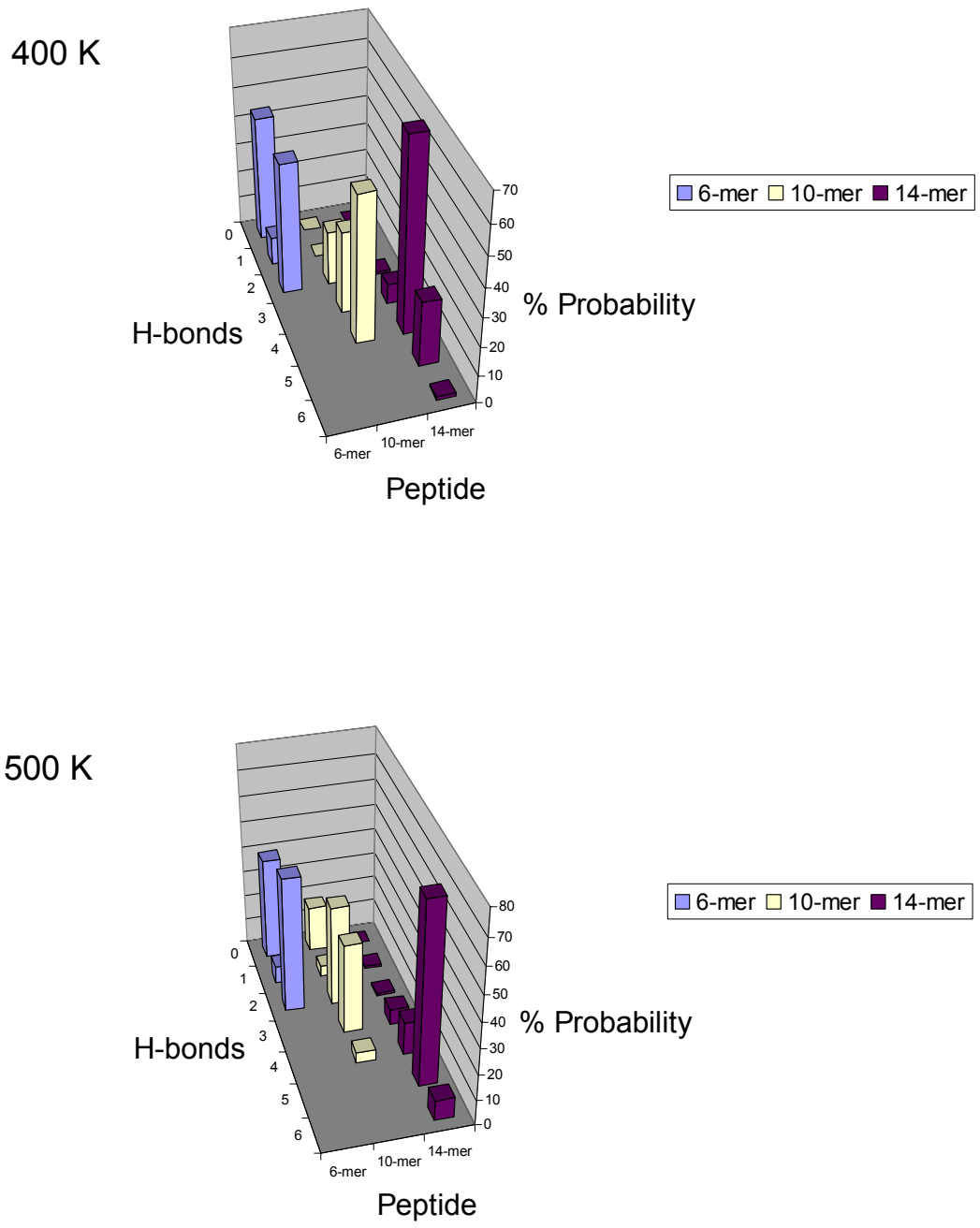

Figure 1 Percent probability for hydrogen bond formation for 6-mer, 10-mer, and 14-mer peptides at 400 K (top), 500 K (bottom), and 600 K (top of following page). Figure 1 continued on the following page.

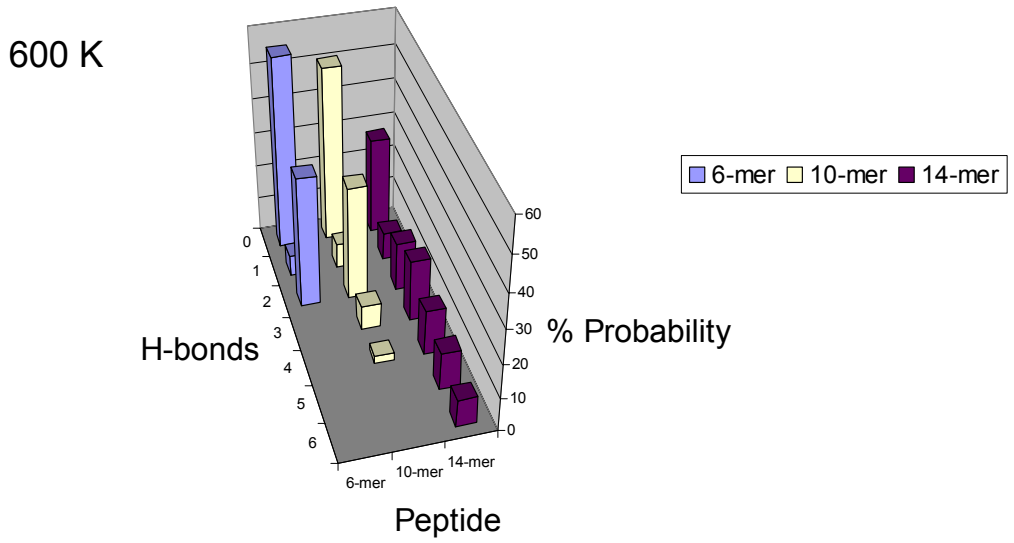

Figure 1 (Continued from previous page)

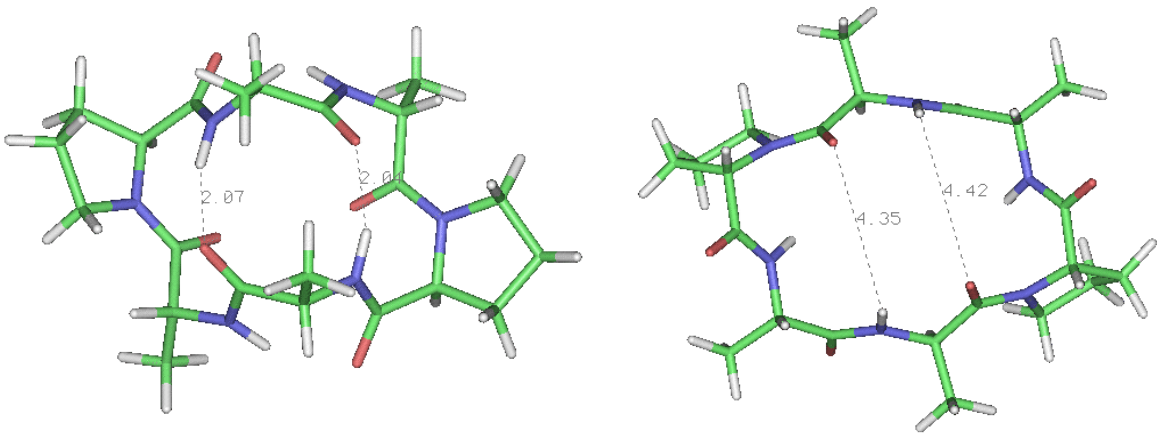

Figure 2 Sample structures of a folded (left) and unfolded (right) hexamer peptide.

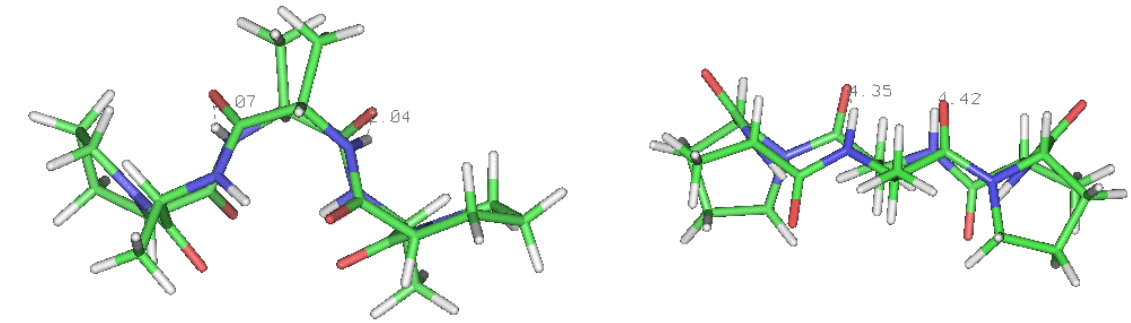

Figure 3 Side view of the folded (left) and unfolded (right) hexamer peptide. The anit-parallel pleated β-sheet is very distinctive for the folded structure.

DFT Calculations. DFT studies of the hexamer peptide compared the amide I frequencies and the calculated infrared spectra of poly-glycine and poly-alanine side-chains in the amide I region. It is important to note that despite the fact that the side-chains are primarily comprised of either alanine or glycine there are two proline residues which are necessary for the β-hairpin turn. DFT results of vibrational frequencies and calculated infrared spectra for the 6-mer were obtained for folded, intermediate, and unfolded structures. Figure 4 shows the comparison of the calculated wavenumbers and their intensities for hexamer structures. Tables 2, 3, and 4 list the frequencies shown in Figure 4. Six frequencies were observed in each case corresponding to the six carbonyl stretches of the polypeptide backbone. Illustrations of the shifts and spectral changes that occurred in the calculated infrared spectra using Gaussian widths of 10 cm^{-1} and 20 cm^{-1} are shown for the folded (Figure 5), intermediately folded (Figure 6), and unfolded (Figure 7) structures. A Gaussian width is determined by the vibrational relaxation time of a molecule. Biological molecules typically have a Gaussian width between 10 cm^{-1} and 20 cm^{-1}. Infrared spectra were calculated using Gaussian widths of both 10 cm^{-1} and 20 cm^{-1} to represent both extremes. The infrared spectra for folded structures occurred at lower frequencies than those of unfolded structures. This is an important observation to note for the structural assignments made in spectroscopic data. The intermediate structure of the hexamer indicated the presence of two peaks which suggests that components of both the folded and unfolded species were represented. The calculated infrared spectrum for the unfolded peptide was shifted to the highest wavenumber which compares favorably with observed experimental data.

Correlation between structure and spectroscopy is best illustrated for the hexamer peptide. Comparisons of the calculated infrared spectra for folded, intermediate, and unfolded structures were combined using the data from Gaussian width fits of 20 cm^{-1} (Figure 8). A shift of ~20 cm^{-1} is observed between the folded and unfolded spectra in both structures comprised primarily of poly-glycine and poly-alanine. Figure 9 shows the temperature-dependent FTIR difference spectra collected for the 6-mer peptide. In this figure, the β-structure region appears around 1621 cm^{-1} while the disordered polypeptide structure is observed near 1653 cm^{-1}. Consequently, a 32 cm^{-1} shift is experimentally observed as compared to ~20 cm^{-1} for the calculated spectra. These results agree quite well considering that the experimental data was based on solution phase measurements while the calculations were all done in the gas phase. These favorable comparisons between experimental and computational results appear very promising for further use in protein folding studies that attempt to correlate structure and spectroscopy.

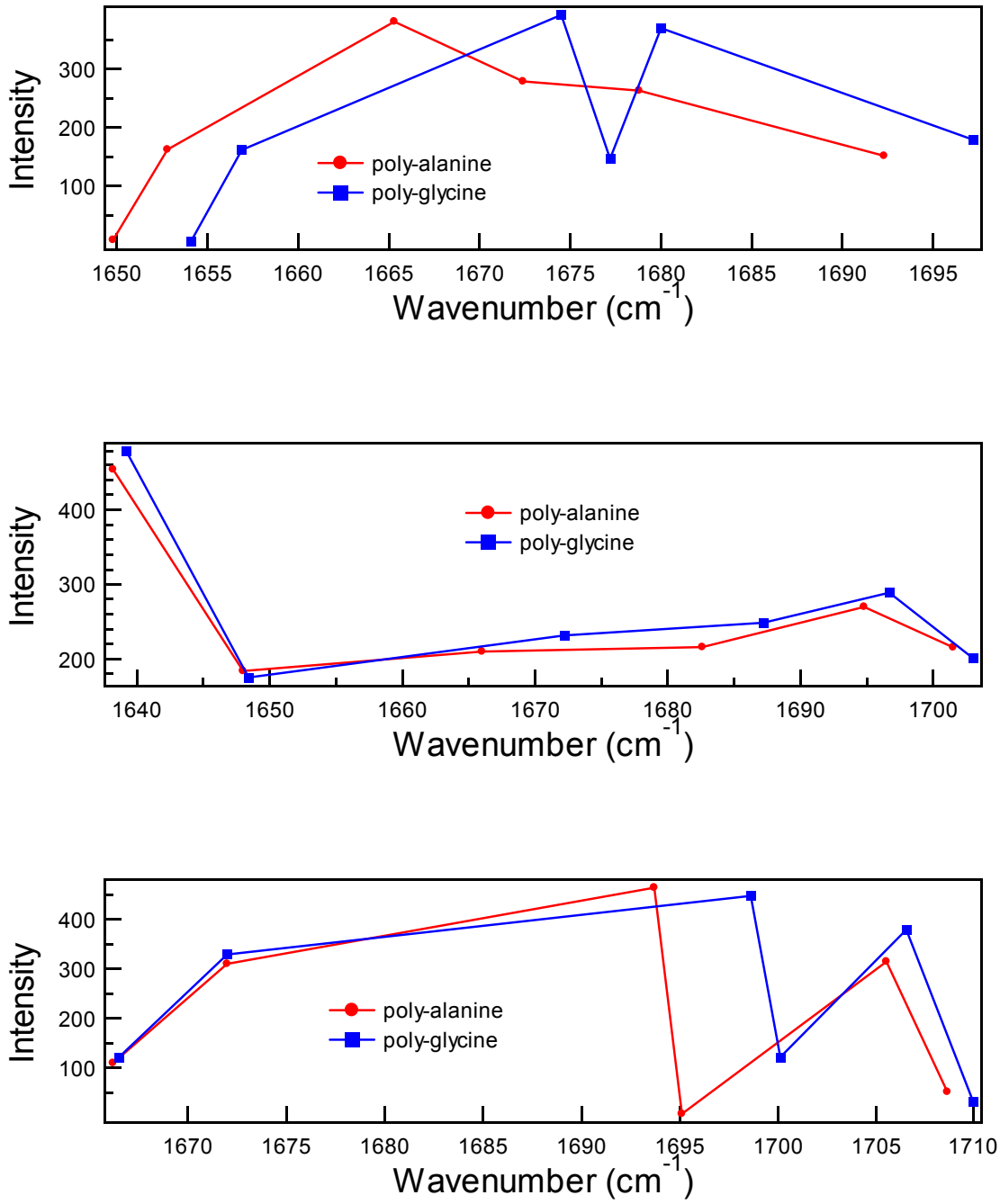

Figure 4 DFT calculated vibrational frequency spectra for the 6-mer peptide in the folded (top), intermediate (middle), and unfolded (bottom) states.

Table 2 Frequecies corresponding to the folded 6-mer structure shown in Figure 4 (top).

Poly-alanine	Poly-glycine
Frequency (cm-1)	Frequency (cm-1)
1649.8	1654.1
1652.8	1656.9
1665.3	1674.5
1672.4	1677.2
1678.8	1680.0
1692.3	1697.2

Table 3 Frequencies corresponding to the intermediately folded 6-mer structure shown in Figure 4 (middle).

Poly-alanine	Poly-glycine
Frequency (cm-1)	Frequency (cm-1)
1638.2	1639.2
1648.0	1648.4
1666.0	1672.2
1682.6	1687.2
1694.8	1696.7
1701.5	1703.0

Table 4 Frequencies corresponding to the unfolded 6-mer structure shown in Figure 4 (bottom).

Poly-alanine	Poly-glycine
Frequency (cm-1)	Frequency (cm-1)
1666.2	1666.5
1672.0	1672.0
1693.7	1698.6
1695.1	1700.1
1705.5	1706.5
1708.6	1709.9

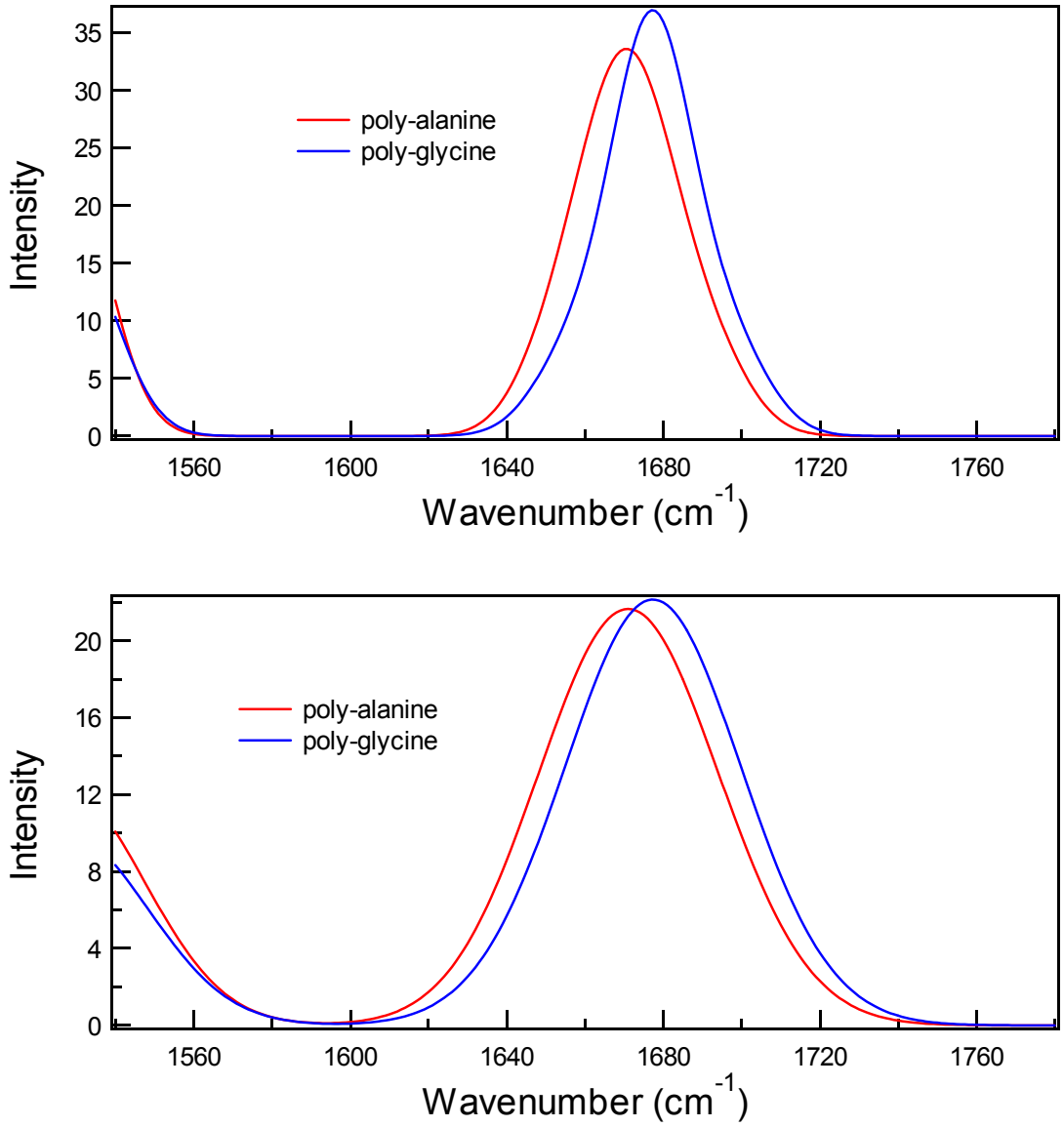

Figure 5 DFT calculated absorbance spectra for the folded hexamer peptide using a Gaussian width of 10 cm^{-1} (top) and 20 cm^{-1} (bottom).

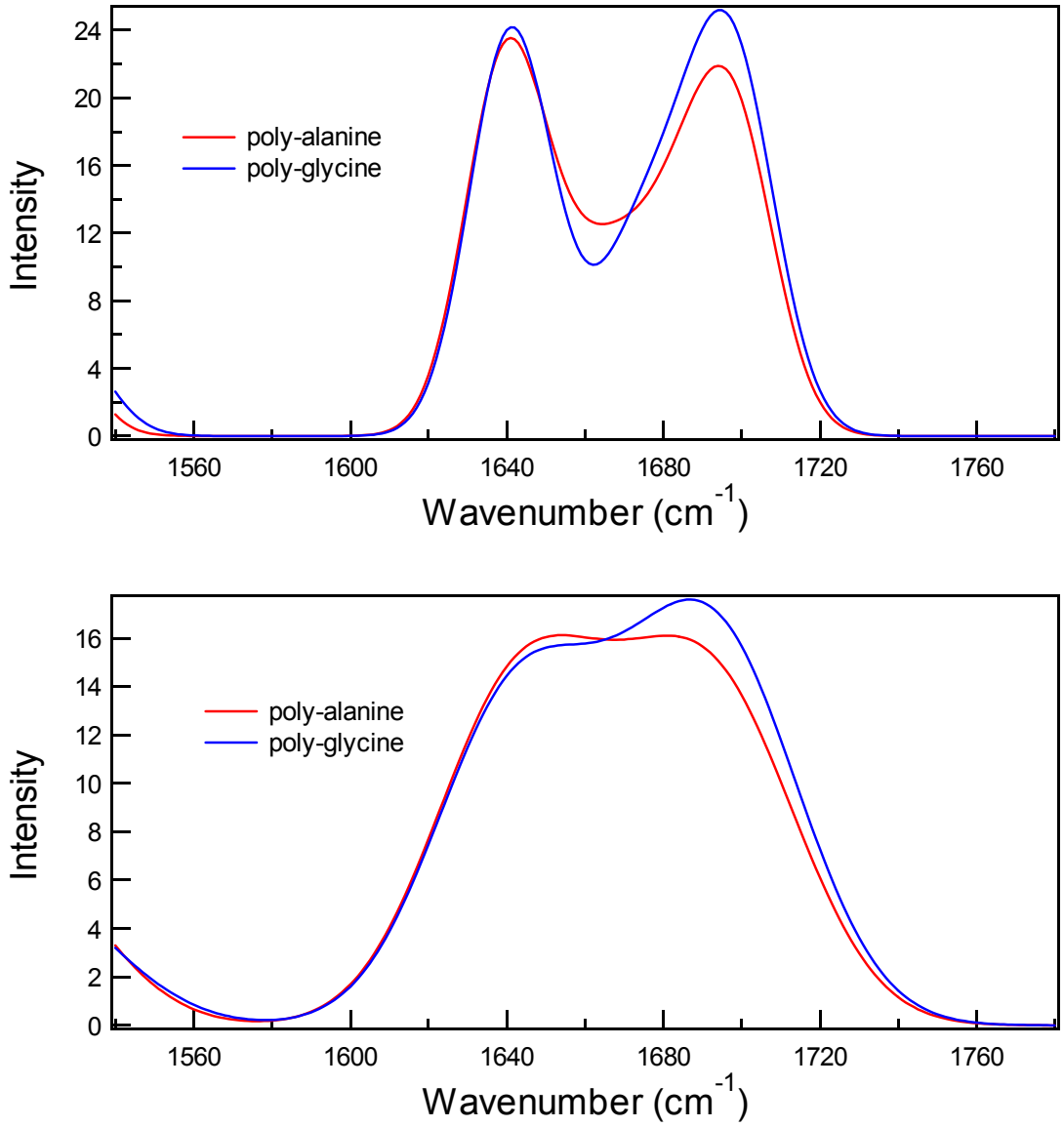

Figure 6 DFT calculated absorbance spectra for the intermediately folded state of the hexamer peptide using a Gaussian width of 10 cm^{-1} (top) and 20 cm^{-1} (bottom).

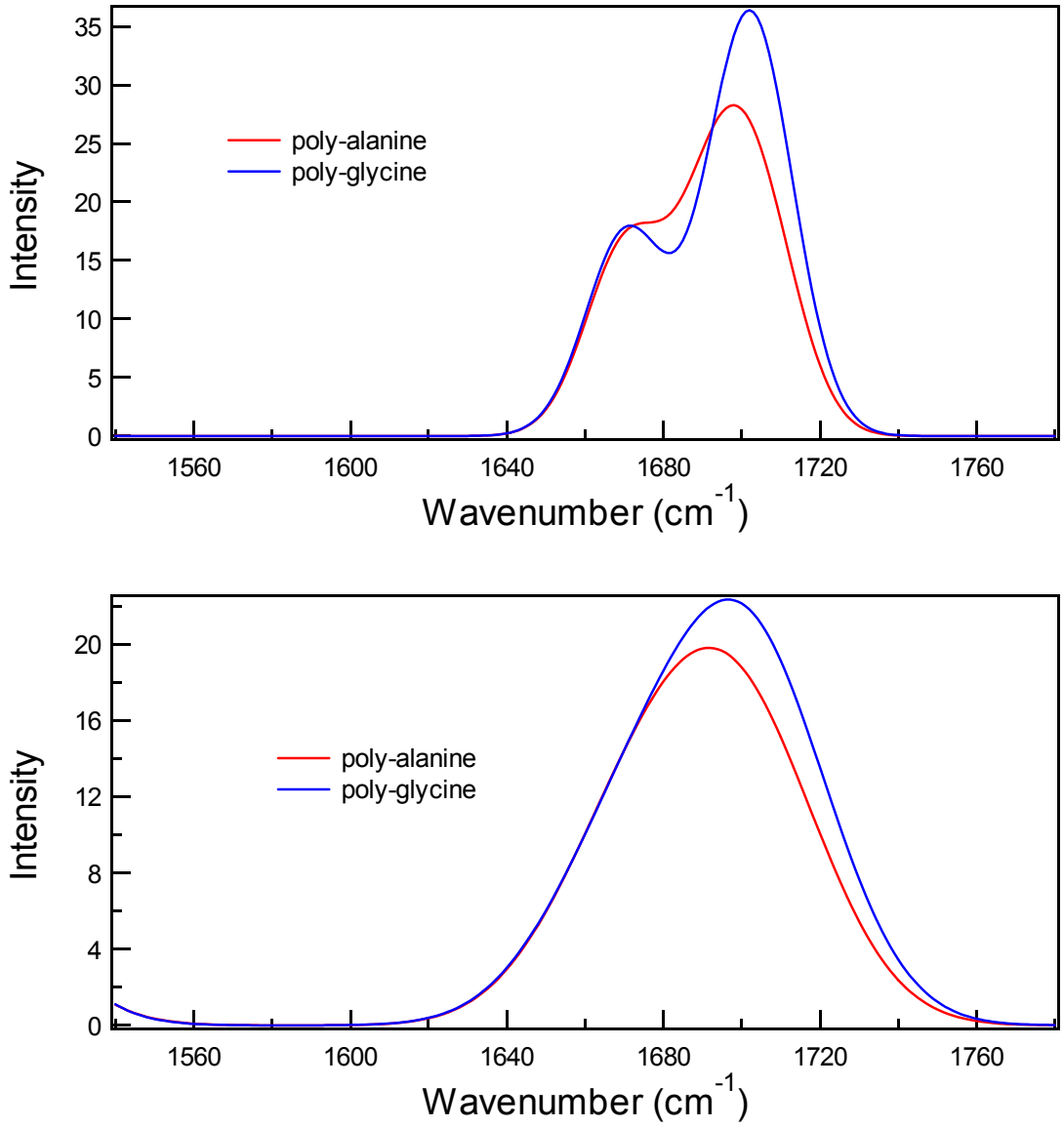

Figure 7 DFT calculated absorbance spectra for the unfolded hexamer peptide using a Gaussian width of 10 cm^{-1} (top) and 20 cm^{-1} (bottom).

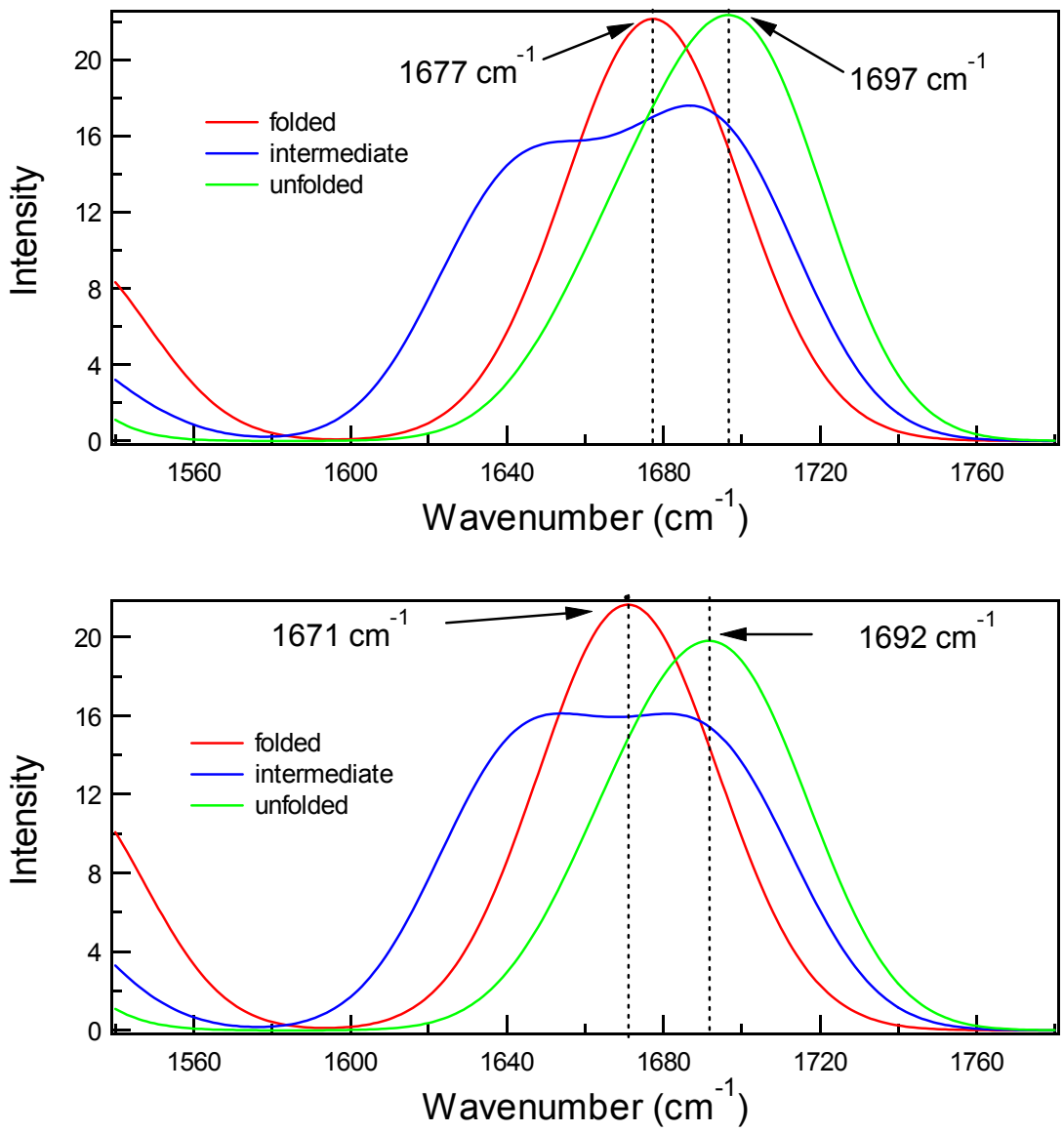

Figure 8 Calculated infrared spectra for poly-glycine (top) and poly-alanine (bottom) with a gaussian width of 20 cm^{-1}.

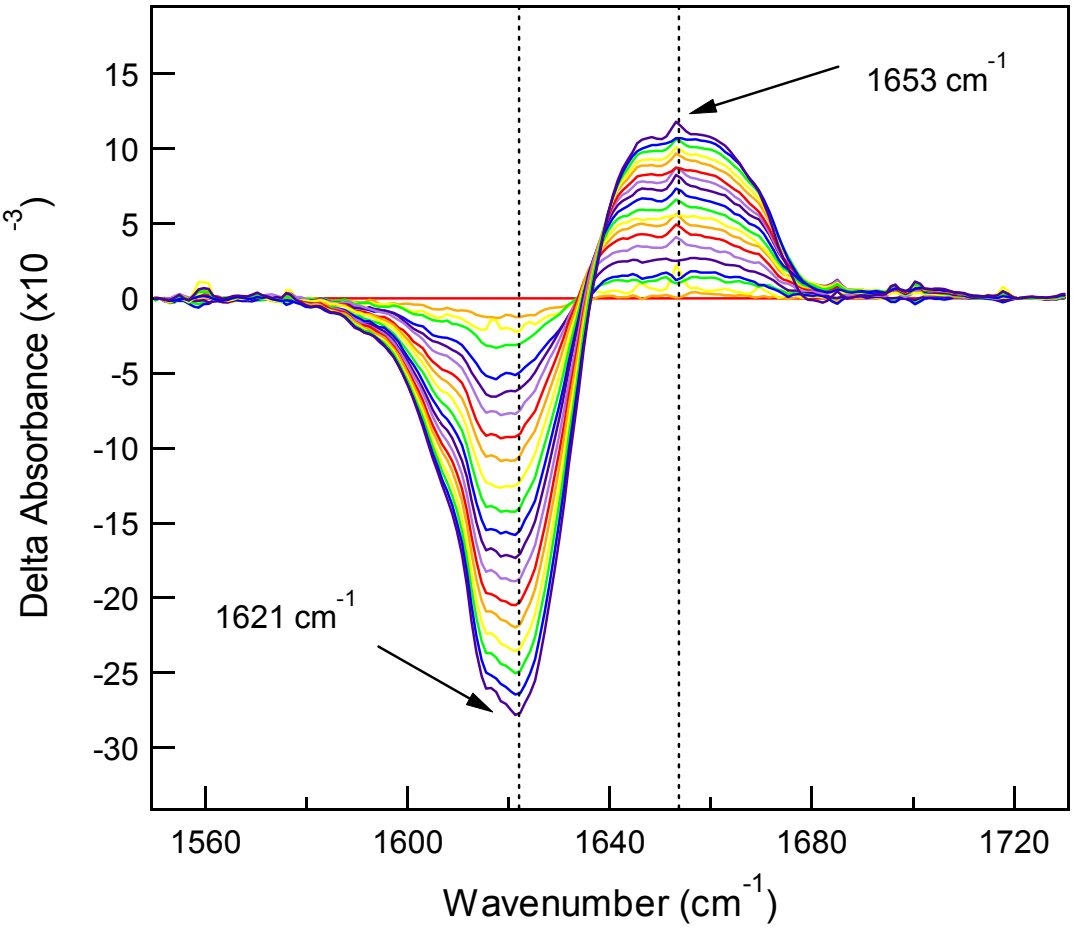

Figure 9 Temperature-dependent difference spectra from FTIR experiments.

The DFT calculations for the hexamer with poly-alanine versus poly-glycine side-chains illustrated the effects of relatively subtle changes between the two peptide structures. Alanine and glycine side-chains produced similar results for vibrational frequency calculations as well as amide I infrared intensity calculations. The decamer computations compared bulkier side-chains to poly-glycine side-chains. Analysis of vibrational frequency calculations for the decamer peptide with its original side-chains versus poly-glycine side-chains found comparable results (Figure 10). Proline residues were the only exception for glycine side-chain substitutions since proline is needed to maintain the β-hairpin turn as mentioned earlier for the hexamer peptide. Despite the similarities between the two types of side-chain frequencies, there are two primary differences observed for the decamer with bulky side-chains versus poly-glycine side-chains. One obvious difference is the frequencies that result primarily from individual side-chain residues. These frequencies are shown in Figure 10 in the range of 1598 – 1644 cm^{-1}. In aqueous experiments, motions such as carbonyl stretching of individual side-chains are typically observed in the amide II region.[5] However, these DFT calculations are based on gas phase properties causing the observed frequencies to be slightly higher than solution phase experiments. These studies focused on the amide I region of the infrared spectrum since all experimental comparisons were made in this well-characterized area.[5-8] The 10-mer structure with glycine side-chains had 10 frequencies in the amide I region (~1600 – 1700 cm^{-1}) which correspond to the number of carbonyl groups present in the structure. Another apparent discrepancy between the two types of side-chain measurements is that the poly-glycine decamer is shifted to a slightly higher frequency. By shifting the maximum intensity peak of the poly-glycine peptide to

match the maximum intensity peak of the decamer with its original side-chains, the frequencies otherwise appear to correspond well (Figure 10, bottom). Wavenumber values for the frequencies shown in Figure 10 are also listed in Table 5. Figure 11 shows the structures for the 10-mer that correspond to the points of highest intensity in Figure 10. The frequency of maximum intensity for the peptide with its original side-chains was at 1678.1 cm^{-1} as compared to the decamer with glycine side-chains which had a maximum frequency at 1686.3 cm^{-1} in the amide I region. The eigenvectors in Figure 11 show the magnitude and intensity of the vibrations resulting primarily from the polypeptide backbone. These data suggest that the polypeptide backbone is the primary source of amide I signal with minimal side-chain contributions in spectroscopic experiments.

Calculation of the infrared spectrum for the decamer peptide indicated no dramatic shifts in the amide I region between the structure with side-chains and the peptide with poly-glycine side-chains (Figure 12). However, the DFT calculation with side-chains showed almost twice the intensity of the poly-glycine model for Gaussian widths of both 10 cm^{-1} and 20 cm^{-1}. In both cases the peak maxima were separated by only two wavenumbers in the region around 1678 cm^{-1} indicating that side-chains do not appear to govern the vibrational features of peptides in the amide I spectrum.

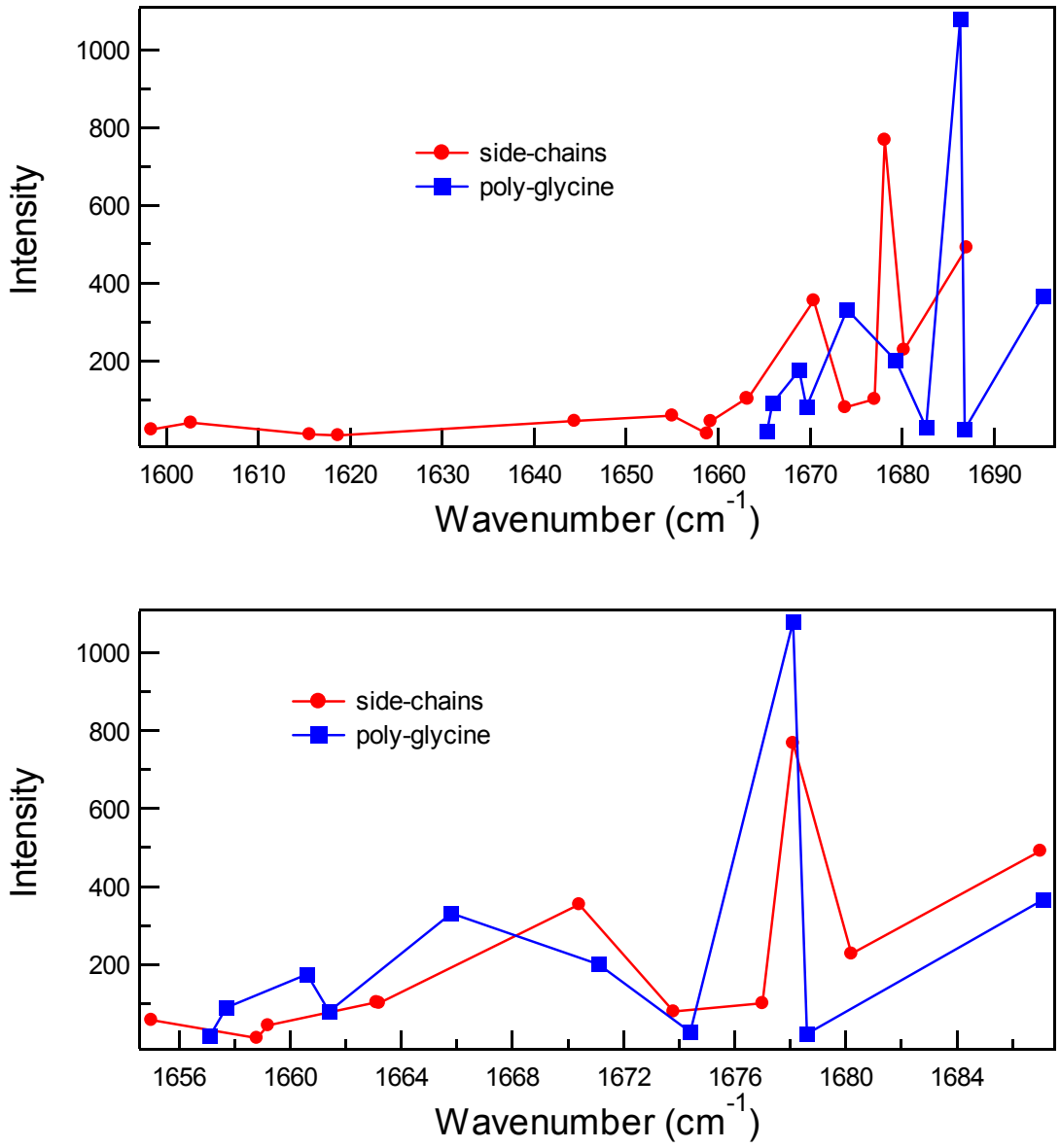

Figure 10 DFT vibrational frequency calculation for the decamer peptide. Calculated frequencies for the amide I region of the 10-mer peptide with original side-chains and glycine side-chains are shown (top). Relatively good agreement is observed by shifting the maximum intensity peak of the glycine model by -8.2 cm^{-1} to correspond to the bulky side-chain peak maximum (bottom). Low frequencies attributed to individual side-chain contributions were omitted from the bottom graph.

Table 5 Comparison of side-chain frequencies for decamer peptide. The shifted glycine side-chain values correspond to the values in Figure 10 (bottom) while the frequencies that are not shifted match those shown in Figure 10 (top).

Side-chains Frequency (cm-1)	Glycine side-chains (shifted) Frequency (cm-1)	Glycine side-chains (not shifted) Frequency (cm-1)
1602.7		
1615.6		
1618.7		
1644.4		
1655.0		
1658.8	1657.1	1665.3
1659.2	1657.7	1665.9
1663.1	1660.6	1668.8
1663.2	1661.4	1669.6
1670.4	1665.8	1674.0
1673.8	1671.1	1679.3
1677.0	1674.4	1682.6
1678.1	1678.1	1686.3
1680.2	1678.6	1686.8
1687.0	1687.1	1695.3

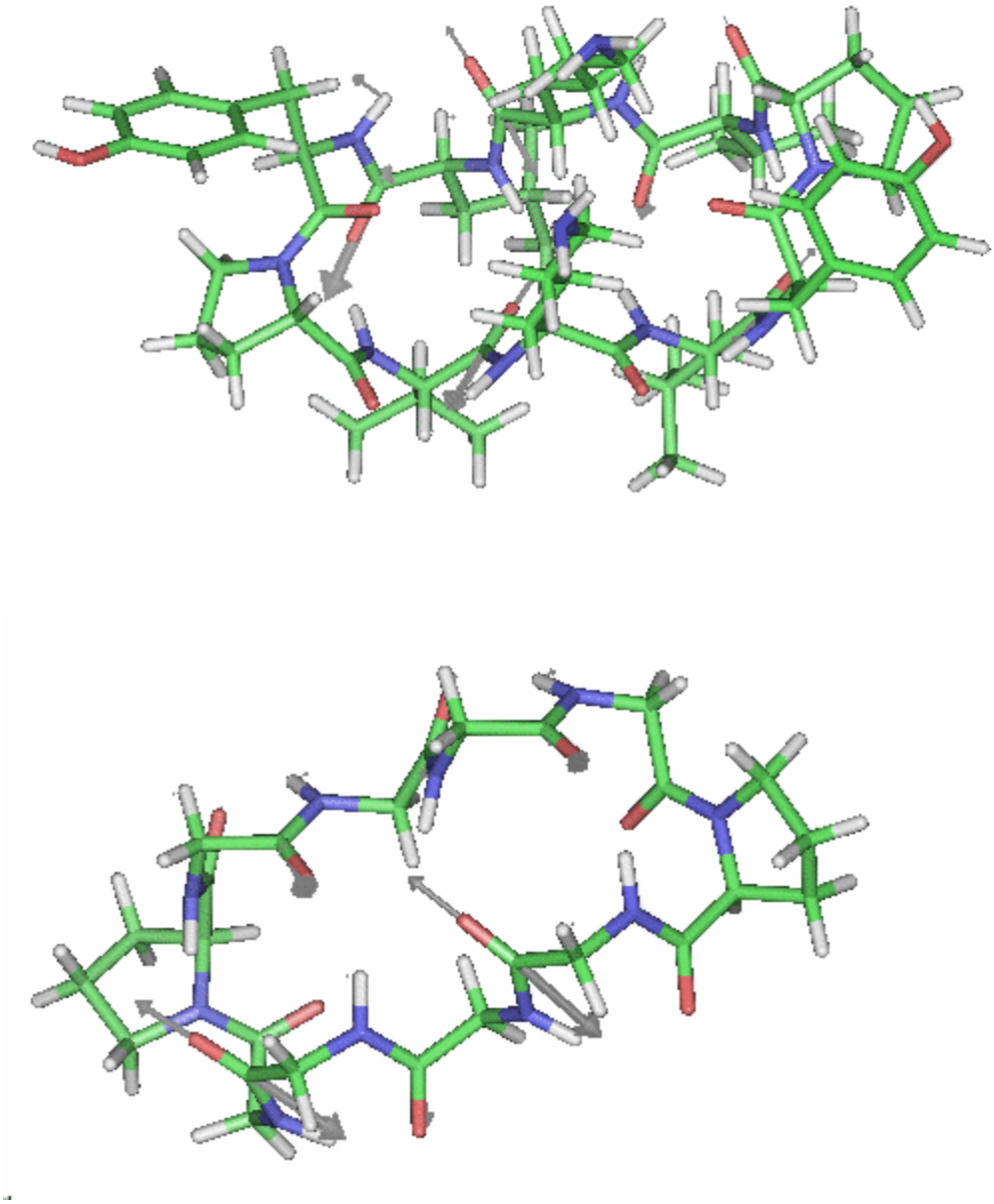

Figure 11 Decamer structures with the highest calculated frequency for the peptide with side-chains at 1678.1 cm^{-1} (top) and with poly-glycine side-chains at 1686.3 cm^{-1} (bottom). Eigenvectors are superimposed on the structures to indicate the magnitude and direction of vibrations.

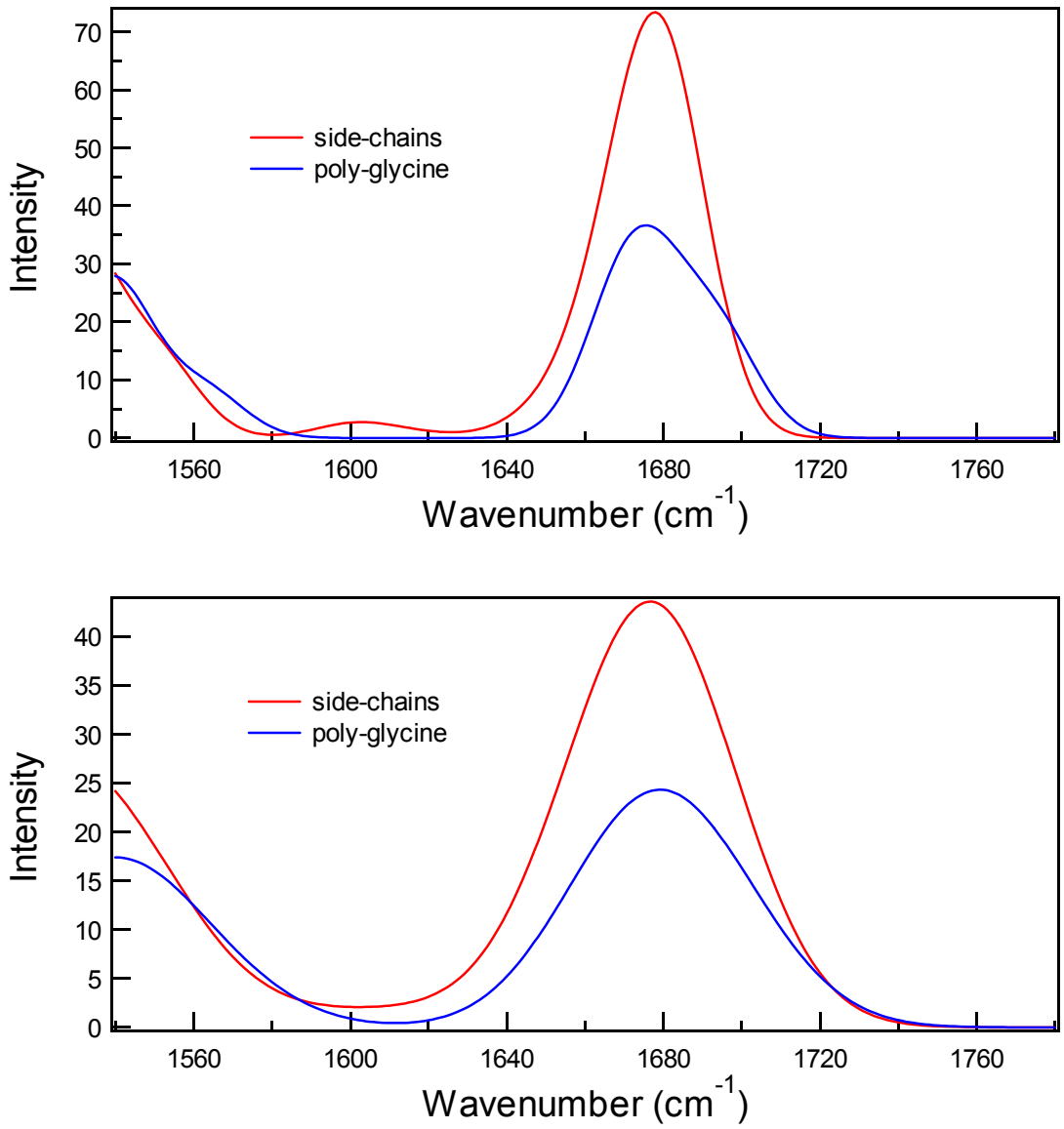

Figure 12 Calculated infrared spectra for the decamer using a Gaussian width of 10 cm^{-1} (top) and a Gaussian width of 20 cm^{-1} (bottom).

CONCLUSIONS

The calculations presented in this study for the cyclic hexamer and decamer peptides corroborate the relationship between frequency (wavenumber) and the folding state of a peptide established by the experimental work presented in Chapter 3 of this dissertation. The good agreement between experimental and calculated wavenumber differences of the folded and unfolded states of a peptide lends credibility to the use of quench dynamics and density functional theory calculations for further studies on the linear peptides discussed in Chapter 4. Comparisons between large and small side-chain groups of the decamer peptide produced similar infrared spectra. This result is important when one considers the reduction in computational time that can be achieved by trimming bulky side-chains without significant loss of accuracy in the result. The information obtained from the computational methods presented show the convergence of theory and experiment in predicting the correlation between structure and spectroscopy which could eventually pave the way for further progress toward understanding the Protein Folding Problem.

REFERENCES

(1) Gibbs, A. C.; Kondejewski, L. H.; Gronwald, W.; Nip, A. M.; Hodges, R. S.; Sykes, B. D.; Wishart, D. S. *Nat. Struct. Biol.* **1998**, *5*, 284-288.

(2) Delley, B. *J. Chem. Phys.* **1990**, *92*, 508-517.

(3) Delley, B. *J. Chem. Phys.* **2000**, *113*, 7756-7764.

(4) Perdew, J. P.; Chevary, J. A.; Vosko, S. H.; Jackson, K. A.; Pederson, M. R.; Singh, D. J.; Fiolhais, C. *Physical Reviews B* **1992**, *46*, 6671-6687.

(5) Susi, H.; Byler, D. M. *Methods Enzymol.* **1986**, *130*, 290-311.

(6) Krimm, S.; Bandekar, J. *Adv. Protein Chem.* **1986**, *38*, 181-364.

(7) Surewicz, W. K.; Mantsch, H. H. *Biochim. Biophys. Acta* **1988**, *952*, 115-130.

(8) Rahmelow, K.; Hubner, W.; Ackermann, T. *Analytical Biochemistry* **1998**, *257*, 1-11.